Design and Testing of a Gated Electron Mirror

by

John Simonaitis

B.S. Electrical Engineering
University of Illinois at Urbana-Champaign (2018)

Submitted to the Department of Electrical Engineering and Computer Science
in Partial Fulfillment of the Requirements for the Degree of

Master of Science in Electrical Engineering and Computer Science

at the

MASSACHUSETTS INSTITUTE OF TECHNOLOGY

February 2021

©Massachusetts Institute of Technology. All rights reserved.

Signature of Author: . . . .

Department of Electrical Engineering and Computer Science
January 15, 2020

Certified by . . . .

Karl K. Berggren
Professor of Electrical Engineering and Computer Science
Thesis Supervisor

Certified by . . . .

Phillip D. Keathley
Group Leader, Research Laboratory of Electronics
Thesis Supervisor

Accepted by . . . .

Leslie A. Kolodziejski
Professor of Electrical Engineering and Computer Science
Chair, Department Committee on Graduate Students

High Voltage, Vacuum Integrated Electronics for Nanosecond Switched Charged Particle Optics

by

John Simonaitis

Submitted to the Department of Electrical Engineering and Computer Science
on January 31, 2021 in Partial Fulfillment of the Requirements for the Degree of
Master of Science in Electrical Engineering and Computer Science

ABSTRACT

One of the primary limiting factors of modern electron microscopes is the damage imparted to samples during imaging, which limits the achievable image resolution for many biological specimens [1]. Recently, there have been several microscope designs proposed to improve resolution in these samples by reducing beam damage employing novel quantum measurement schemes such as interaction free measurement [2] and multi-pass electron microscopy [3]. These designs fall under the heading of a quantum electron microscope (QEM). A recurring element of all actively explored QEM designs is a linear cavity for recirculating electrons. This cavity, which could be inserted into existing microscopes, would allow for either the wavefunction transfer required for interaction free measurement or the phase build-up needed for multi-passing protocols to reduce specimen damage. In order to achieve these modes, there must be some way to open and close this cavity in a controlled fashion to allow electrons to enter, stably recirculate, then exit the setup. One approach to realizing such a cavity is the construction of a gated electron mirror, an electron optical element capable of switching between two operating states. In one state it transmits electrons travelling along its optical axis, while in the other it reflects them back onto their incident path. This gated mirror is required to operate at kilovolt potentials and reflect electrons with high accuracy within a several-nanosecond switching time frame.

In this thesis, we aim to develop, build, and test such a gated electron mirror. We first outline in Chapter 1 the electron-damage problem, approaches to solving it, and how QEM might do this. Next, in Chapter 2, we review state-of the art fast pulsing approaches, as well as requirements for the mirror. In Chapter 3 we then design and test a fast pulse generating circuit based on emerging Gallium Nitride on silicon technology. In Chapter 4 we simulate the performance of the gated mirror. We optimize the structure of the gated mirror to minimize transition times and errors, and avoid induced voltage changes in other parts of the apparatus. We also discuss various design approaches to improve device performance, such as integrating high voltage pulsing electronics into the gated mirror itself. We also discuss the ultimate limits of switching. In Chapter 5 we then develop and show progress on an apparatus for testing the switching characteristics of the gated mirror in both time and frequency domains, directly probing the changing fields using an electron beam. Finally, in Chapter 6 we discuss improvements to our measurements and next steps.

Thesis Supervisor: Karl K. Berggren

Title: Professor of Electrical Engineering and Computer Science

Thesis Supervisor: Phillip D. Keathley

Title: Group Leader, Research Laboratory of Electronics

Acknowledgments

This work would not have been possible without the constant help and advice from many of my friends, family, colleagues, and mentors. In particular, I would like to thank the following people who have helped me the above and beyond:

My co-advisors Prof. Karl K. Berggren and Dr. Phillip D. Keathley, for their constant mentorship and for creating a exciting and deeply collaborative research environment to work in. In addition, I would like to thank Karl for his excitement for the little victories in research, his emphasis on the broader responsibilities of his students as citizens and scientists, and his open acceptance of both crazy ideas and failure. I would also like to thank Donnie for the many great conversations we have had about engineering and science in general, for his tireless hands-on help with the practical aspects of research, and most of all for helping me understand difficult problems when I asked for help, and especially when I did not. I have learned so much from both of you, in research and outside of it.

I would also like to thank Dr. Yugu Yang-Keathley and Ben Slayton for the tremendous help you both gave with simulating and understanding gated mirrors, the core work of this thesis.

In addition, I would like to thank Dr. Akshay Agarwal, Navid Abedzadeh, Marco Turchetti, and Peter Satterthwaite for many great conversations in research and beyond. I would also like to thank everyone in the QNN group for creating such an open and fun research environment.

I would like to thank our collaborators in the QEMII Collaboration for many extremely useful conversations and for laying the groundwork for this thesis. I would like to specifically thank the Kasevich group at Stanford, especially Adam Bowman, Brannon Klopfer, and Stewart Koppell, for many discussions of the gated mirror and electronics to drive it, and Prof. Pieter Kruit and Maurice Krielaart at TU Delft for incredibly useful discussions on constructing a gated mirror and streak camera.

I thank the Gordon and Betty Moore Foundation for supporting the Quantum Electron Microscope project and this work. This material is based upon work supported by the National Science Foundation Graduate Research Fellowship under Grant No. 1745302.

I would last like to thank my parents, Bill and Kathleen Simonaitis, for fostering my curiosity in everything, even if it meant me taking apart televisions and microwaves and scattering the remains about the basement. I'd like to thank my brothers, Pat and Will, for putting up with the know-it-all-ism that likely led me on the path to graduate school. Lastly, I'd like to thank my grandparents, George Cady, Kathleen Cady, Grace Simonaitis, and Dr. John Simonaitis for teaching me so many lessons in life, from how to treat others to living life with endless curiosity.

List of Figures

Contents

Chapter 1

Mitigation of Radiation Damage by Quantum Electron Microscopy

One of the key challenges of modern electron microscopy is the imaging of beam sensitive specimens. While inorganic materials such as carbon and gold can be imaged directly to sub-Angstrom atomic resolution, organic samples such as proteins and viruses can not due to the immense amount of damage caused by incident electrons [4]. Modern transmission electron microscopes (TEMs) are limited in their resolution by the the maximum number of electrons that can be used to image a sample before it is destroyed, and the smallest length scale of a specimen they can resolve is referred to as their dose-limited resolution [4, 5].

In this chapter, we first briefly review the state of the art in the electron microscopy of biological specimens, as well as routes for improving these and the ultimate limits of cryo-EM. Then, we explore the possibility of quantum techniques, which are aimed at using quantum resources (electrons) as efficiently as possible to obtain the best possible signal-to-noise ratios in our specimen with the least damage. This lower damage leads to the best possible resolution. Finally, we discuss our general efforts to develop one of these schemes for quantum electron microscopy (QEM), outlining each required component [2]. This thesis focuses on the development of one of the central components of such an instrument, a gated electron mirror.

1.1 Existing approaches to improving dose-limited resolution

An understanding of damage in cryo-EM is crucial to understanding approaches to mitigating it, as well as the inherent resolution limitations caused by it. Damage in cryo-EM stems from two types of electron scattering: elastic scattering of high-energy electrons from the nucleus, which can cause ejection of

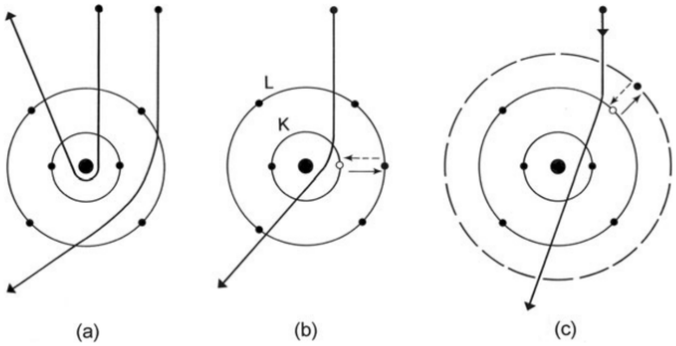

Figure 1.1: (a) Elastically scattered electrons, with the outer incident electron showing scattering that leads to image contrast, and the inner strongly scattered electron showing knock-on damage, where the backscattering of the electron leads to ejection of the atom. (b) Inelastically scattered core-shell electron scattering, where an inner electron is ejected from the atom to a higher valence state. Upon the return of this electron to the ground state, x-rays are generated. (c) Inelastically scattered valence-shell electron scattering. This kind of electron-electron scattering leads to irreversible damage through bond breaking and heating of the material of interest. Figure taken from Fig. 1.1 of R.F. Egerton [5]

atoms from a material, and inelastic electron-electron scattering, which causes charging, heating, structural deformation, and mass loss in samples due to disruption of electron bonds in materials [5]. This is demonstrated in Fig. 1.1 taken from Chapter 1 of [5]. These unavoidable damage processes significantly limit resolution in beam sensitive specimens to a few nanometers, far larger than the sub-Angstrom capabilities of aberration-corrected TEMs [6]. An example of this can be seen in Fig. 1.2, where at low doses the resolution is limited by noise in the system, and at high doses the resolution is limited by damage to the specimen.

A major breakthrough in the imaging of biological specimens was the development of electron cryomicroscopy (cryo-EM) [7, 8, 9], which netted its inventors the 2017 Nobel Prize in Chemistry. This technique, which works by freezing molecules in vitreous ice, destructively imaging millions of copies them to get partial information from each, and then reconstructing this information into a three-dimensional representation of the molecule, only achieved atomic resolution in 2020 [10]. Even still, there are many shortcomings of this approach such as its ability to only image large proteins and the requirement of imaging millions of copies of the specimen, which takes significant time and computational resources, and destroys the possibility of real-time imaging of structural changes [11, 12].

Many approaches have been taken and proposed to improve Cryo-EM performance further through purely classical means. Examples offering substantial improvement include: cooling and encapsulating of specimens to reduce heating and protect from mass loss [4]; optimization of incident beam energy and specimen thickness [14, 13]; improvements to the energy spread and coherence of electron sources [15];

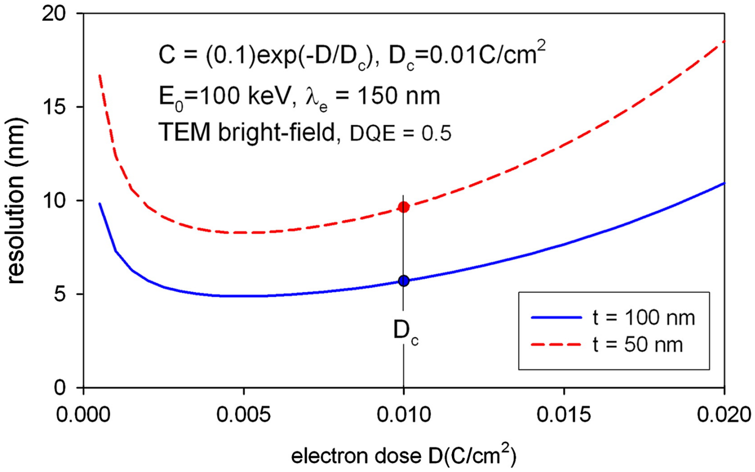

Figure 1.2: Example of dose-limited resolution in cryo-EM. At low doses, resolution is limited by shot noise, while at higher doses the damage limits resolution. This figure shows the effect of changing specimen thickness on damage. Figure taken from [13].

improvements in detector quantum efficiencies to waste as few electrons as possible[16]; and improvements to computational reconstruction algorithms [17].

One important aspect to minimizing damage and producing high quality images in cryo-EM is understanding contrast mechanisms in it. All organic molecules are made primarily of light elements such as carbon and hydrogen, and thus under electron illumination they appear as weak electron phase objects. In fact, the negligible amplitude blocking they cause is due to damaging events, and thus is optimally avoided. Therefore, in perfect focus it is impossible to form an image of proteins with significant contrast. The historical way of getting around this in Cryo-EM was to instead defocus the probe slightly, using the so-called Scherzer defocus [18]. Only since 2001 have components such as the Zernike [19, 20], Volta [11], and Boersch [21] phase plates enabled direct phase contrast of specimens. Since 2016, various proposals and demonstrations have emerged that aim to improve these phases further by adapting them in-situ. [22, 23]. However this adaptive approach is still in its infancy.

1.2 Quantum approaches

In recent years, much work has been proposed to take advantage of the quantum nature of electrons in biological imaging. This work seeks to use electron properties such as their phase, wavelength, and wavefront structure as an advantage in quantum sensing, rather than a detrimental trait that limits resolution and makes contrast generation more difficult. A few of these approaches are reviewed below, before discussing the approach that is the subject of this thesis.

1.2.1 Structured Illumination and Entangled States

One proposal to improve resolution in Cryo-EM is through the use of structured illumination. Structured illumination has already been demonstrated to some degree through the generation of electron vortex beams [24, 25], useful states for imaging the magnetic properties of materials. General structured illumination takes this several steps further. The basic idea of this is to use patterned or adaptive phase plates to impart complex structure onto the electron probe. This structure is tailored to a specific protein, and if the protein is illuminated properly, the resulting wave function scattering leads to the refocusing of the beam to a distinct point in space [26]. If any other protein is illuminated, the electron will scatter off to completely different locations. The core appeal of this approach is that it might be possible to identify and sort proteins using only a single electron. However challenges in realizing such adaptable phase plates and accounting for the many possible orientations of proteins in vitreous ice can be in have yet to be settled. This work was recently funded by the European Union's Horizon 2020 Research and Innovation Programme under Grant Agreement No 766970 Q-SORT (H2020-FETOPEN-1-2016-2017), and is an exciting quantum approach to protein imaging.

Another proposal that seeks to reduce electron damage in Cryo-EM uses entanglement to improve image signal-to-noise ratios to the quantum limit [27, 28, 29]. This concept is similar to the use of N00N states in light optics to reduce the quantum resources required for a given measurement accuracy [30]. The idea is that by entangling incident electrons with quantum resources such as flux or charge qubits, we can reduce shot noise scaling as a function of particles used N past the classical limit of $1/\sqrt{N}$ and to the quantum limit of $1/N$. However, this approach has numerous technical challenges and has yet to be realized.

1.2.2 Interaction free measurement

Another approach to reducing electron beam damage stems from the famous thought experiment of Elitzur and Vaidman [31] known as interaction free measurement (IFM). The core idea of this is summarized in Fig. 1.3 below, where the object is taken to be a ”quantum bomb” for dramatic effect. If an object exists in the path, there is a 25% chance of measuring its existence without interacting with it, as described in 1.3. While interesting, this is not particularly useful.

This thought experiment was later extended in the work of Kwiat et al. [32] to result in the detection of an object with zero chance of interacting with it. This is achieved through the principle or repeated interrogations, or the quantum Zeno effect, shown in Fig. 1.4. By probing the sample with only a tiny

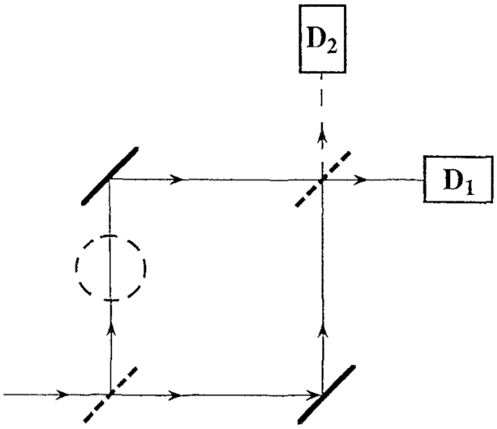

Figure 1.3: IFM Demonstration. The dotted circle represents where an object would be placed in this experiment. Starting from the bottom left we have an incoming quantum resource. This is the split into a 50-50 chance of either path at the beam splitter (the diagonal dotted line). This is then recombined at the second beam splitter in the top right. In the case of no object then we can vary the relative phase to interfere the electron with itself to constructively interfere at D_1 and destructively interfere at D_2, always leading to a D_1 count. If we then put an absorptive object in this path as shown, suddenly this interference can not occur. In this case there is a 50% chance of hitting the object and a 50% chance of hitting the second beam splitter, leading to a 25% chance of hitting D_1 and a 25% chance of hitting D_2. In this case, hitting D_2 implies an object was in the path, but there if it hit D_2 it could not have interacted with the object, and so we can infer its existence without an interaction. This is the crux of IFM. Figure taken from [31]

probability many times, the overall probability of interaction approaches zero, while the probability of detecting the object if it exists approaches one. The difference between no object and an object is illustrated in 1.4a and 1.4b respectively. In case (a), the electron simply resonates to the top half through a partial mirror of reflectivity $1/N$ over N iterations, eventually entering the top. In case (b), the electron repeatably interrogates the sample, with a probability of interacting of $1/N^2$ on each pass. The total probability of interacting is then just $1/N$. As N approaches infinity, the interaction probability approaches zero, and the measurement truly becomes interaction free.

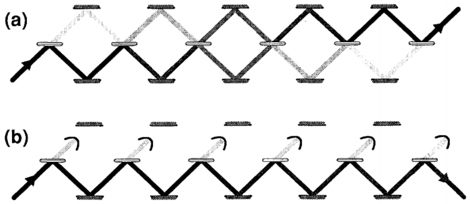

Figure 1.4: Quantum Zeno Effect Demonstration. (a) Repeated splitting of the electron wavefunction leads to the coherent transfer of the electron from the lower half of the figure to the upper half. (b) Repeated splitting of the electron wavefunction with an object blocking coherent transfer to the upper half. Figure taken from [32]

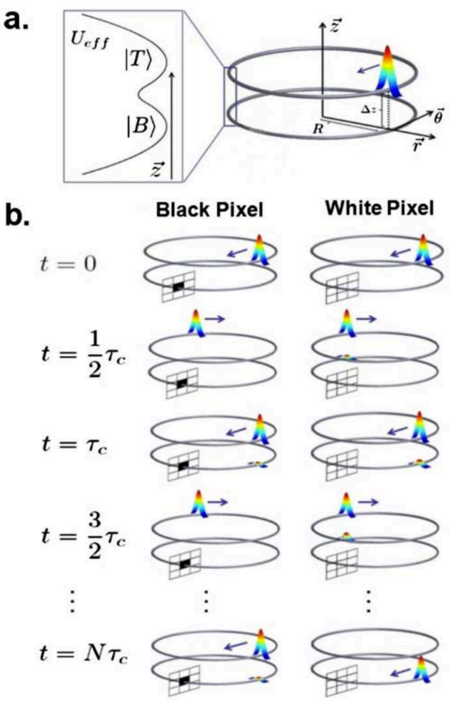

Figure 1.5: A proposed IFM experiment using charged particle traps. (a) The experimental setup, where two closely spaced charge particle traps form an effective potential U_{eff} with states $|T\rangle$ and $|B\rangle$ corresponding to a particle in the top and bottom well respectively. (b) The proposed interaction free measurement, where in each circulation of the top loop there is some electron wavefunction coupled into the bottom. Figure taken from [33]

In 2009, Putnam and Yanik proposed an experimental realization of this concept using electrons held in charged particle traps [33]. This worked by forming a double well potential as shown in Fig. 1.5a. In this experiment, the electron circulates inside the trap, and after each round trip some of the electron is coupled into the bottom loop. which is shown in Fig. 1.5a. In the case of the black pixel, this transfer is disrupted each circuit of the loop, interacting slightly with the black pixel and keeping the electron in the upper loop. In the white pixel, no blockage occurs and the wavefunction is fully transferred from the top to the bottom state. By tuning the number of round trips N needed to fully switch from one trap to the other (and therefore the coupling strength), this could theoretically achieve IFM measurements with the damage probability approaching zero, limited only by the coherence time of the electrons in the circulator.

In 2016, designs for the realization of an IFM scheme in an electron microscope were proposed by Kruit et al. [2]. This approach introduced several new elements to a standard TEM, the most notable being a pulsed electron source, a recirculating cavity, gated electron mirrors to in-couple and out-couple electrons, and a coherent beam splitting element. These elements are summarized in Fig. 1.6 from the work of Turchetti et al. [34], where a more specific IFM-based design was proposed.

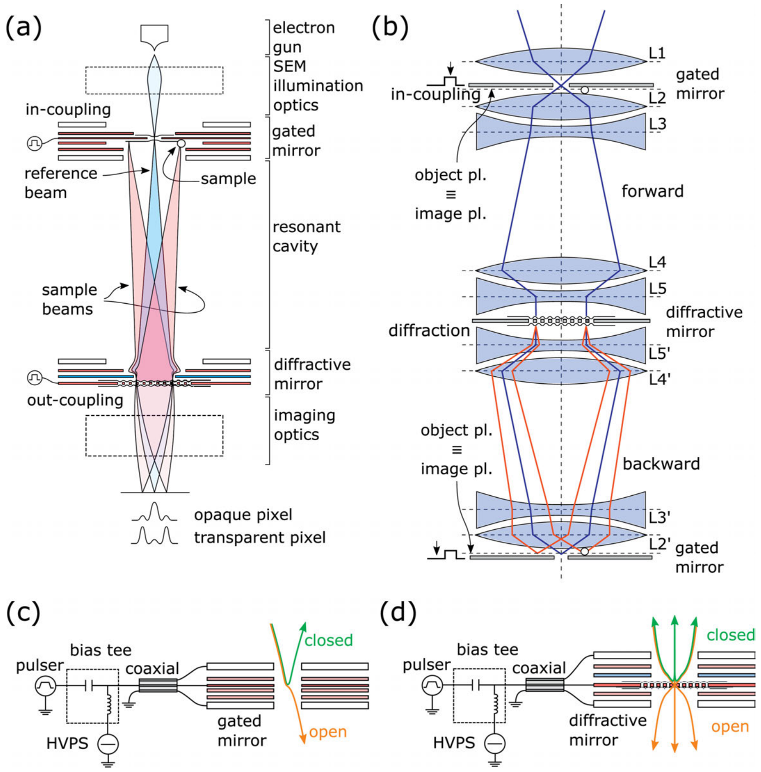

Figure 1.6: A proposed IFM experiment using a linear cavity in a TEM. (a) A schematic design showing each component of the microscope as described in the text. (b) A ray-optical view of the cavity, showing the various images formed and diffracted orders. (c) A rendering of the gated electron mirror, showing its behavior in the open and closed states. (d) the operation of a related diffractive electron mirror required for successful operation of the cavity. Figure taken from [34].

In this design, shown schematically in Fig. 1.6a, electrons are generated by a laser triggered electron gun before being focused by illumination optics onto the center of the so-called gated electron mirror. When this mirror is in its transmitting state, the electrons pass through, where they impinge on the beam-splitting element, a so-called diffractive electron mirror. Upon reflecting, one of the diffractive orders is incident on the sample, which blocks coherent coupling to that order. After a predetermined number of round trips N set by the coupling strength of the diffractive mirror, the electron is out-coupled to imaging optics and a detector via a second gated electron mirror. If an object exists, the diffraction is blocked and we have most of the intensity in the central order as shown with the opaque pixel. If there is no object, the intensity shifts primarily to the diffractive order as shown in the transparent pixel case. It is critical to have a low-loss or loss-free diffractive element to achieve this, or else the quantum advantage disappears [2].

One of the key elements we highlight is the gated electron mirror, which is crucial for properly in-coupling and out-coupling electrons from the cavity. This will be discussed later in this thesis. Another is the diffractive electronic mirror [35] which is based on reflecting electrons from just above a nanostructured surface. While appealing in theory, this has yet to be demonstrated in a modern microscope system, though mentions of this by Lichte et al. from 1983 appear in conference proceedings [36]. Due to the complexity of such a component and its integration into apparatus, our efforts have shifted to focusing on an alternative microscope configuration known as a multi-pass transmission electron microscopy [37].

1.2.3 Multi-pass electron microscopy

The theory of multi-pass transmission electron microscopy (MPTEM) is quite similar to that of an IFM based microscope. The core principle underlying its operation is the concept that repeated weak phase measurements using the same quantum resource results in an enhancement of signal-to-noise (SNR) ratios in a phase measurement [38]. If we have m passes, this leads to an m-fold SNR enhancement when applied to weak phase objects, include all proteins at high electron energies [37]. An example of this enhancement is shown in Fig. 1.7, where we see over multiple passes an enhancement of SNR at various fixed doses.

The design of the MPTEM is extremely similar to an IFM based microscope. The key difference between them is the lack of an explicit electron beam-splitting component such as a diffractive electron mirror [37], although technically one can interpret the sample itself as the beam-splitting element. A proposed design is outlined in Fig. 1.8, which is taken from [39]. The principle of multi-passing has been demonstrated using photons by Juffmann et al. [3], though has yet to be shown with electron illumination.

The operation of such a microscope occurs in three parts. During illumination, the first gated electron

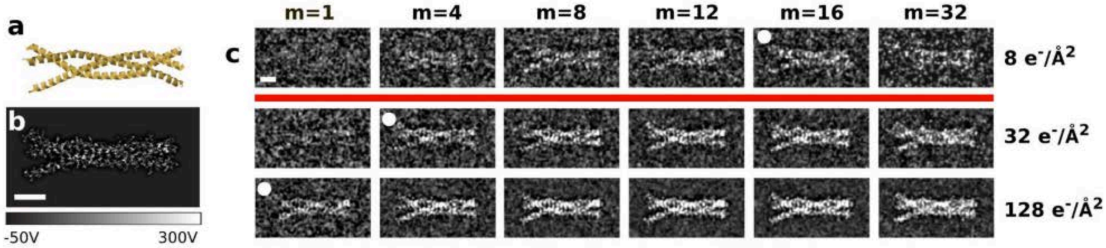

Figure 1.7: Simulation of the phase enhancement of multi-pass electron microscopy in a real protein. Figure taken from [37].

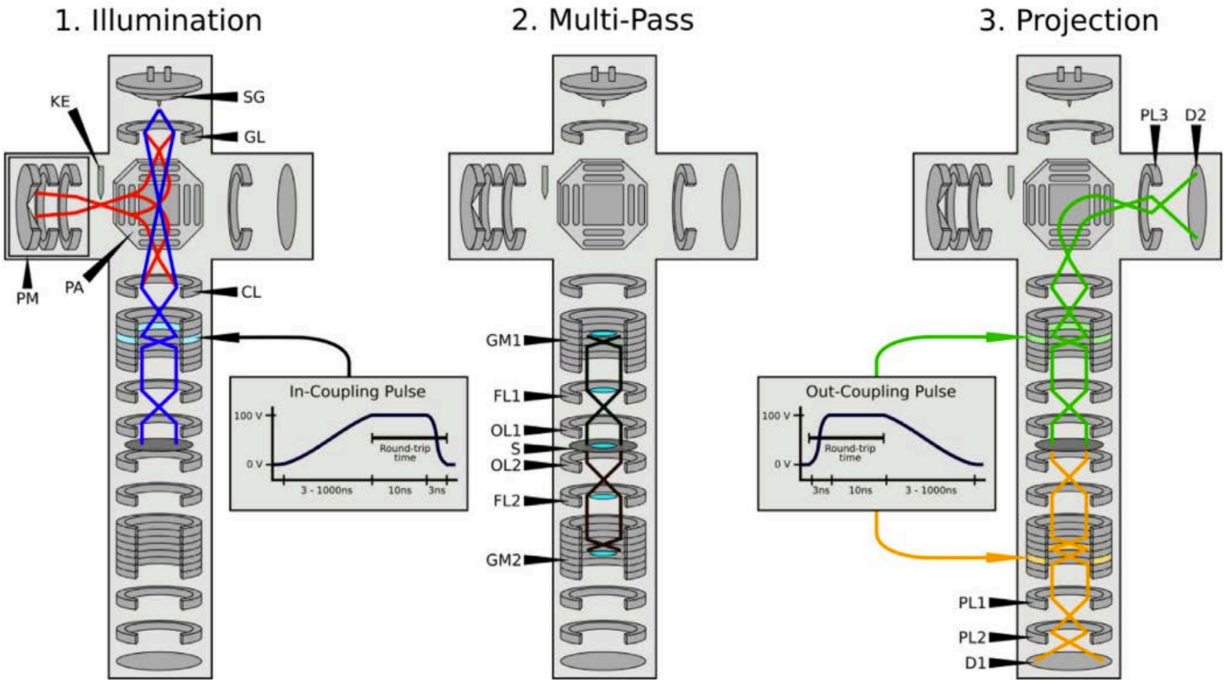

Figure 1.8: A proposed MPTEM integrated into a linear cavity in a TEM. It is broken into three operating steps: illumination, multi-passing, and projection. Figure taken from [39]

mirror (GM1) is opened with a few-nanosecond-switched voltage pulse. This allows electrons to enter the chamber. Next, we close GM1. The mirror must fully close by the time the electrons return from reflecting off the second gated mirror (GM2) for multi-passing to occur. Finally, we open GM2, allowing the electron that has built up a phase shift from N passes to exit the chamber and be imaged. In contrast to the IFM-based approach, the only novel electron-optical element required for this to function is the gated electron mirror: the topic of this thesis.

Chapter 2

Requirements for Pulsing of a Gated Electron Mirror

In order to realize a functioning Quantum Electron Microscope, we require some way of stably in-coupling and out-coupling electrons from an electron cavity. Due to the quantum-coherent nature of this approach to imaging, we require stringent performance specifications on this gated electron mirror transition. In this section, we elaborate on these requirements. We also discuss various state-of-the art pulsers and their potential use in a gated mirror, before settling on a technology that is explored in the rest of this thesis.

2.1 Requirements for a gated electron mirror

The basic experiment undertaken in both the case of IFM and multi-pass electron microscopy is shown in Fig. 2.1 below. Depending on the microscope design, the gated mirror requirements vary. In this thesis we will discuss the design of a gated mirror for a 10 keV multi-pass based electron microscope [39], but the designs are easily applied to other IFM-based designs as well [34]. There are six operating regimes for the microscope, three static and three transitory. In the first, default, state of the microscope, the top gated mirror is open (held at -9.95 kV), and the bottom is closed (held at -10.05 kV). In this state, electron pulses can be injected into the cavity as shown in Fig. 2.1a. Next, a -100 V pulse is applied to the top Gated Mirror 1 (GM1), putting it in the transitory regime shown in Fig. 2.1b. This transition must be completed in a time t_{close} which is less than the round-trip time of the cavity, t_{rt}. Previous work has used classical estimates to show that the mirror must be within 1% its final value in order to minimize spatial and energetic aberrations to the the electron probe [39, 34]. Of course, given that our approach is quantum and requires continued coherence of the electron packet after reflection in all cases, the requirements may be more stringent. This is discussed in Chapter 4.

Assuming proper shutting of the cavity and stable in-coupling of the electron beam, we allow the electron to recirculate for N round trips, the number N being set by optimizing for the phase accumulation and absorption per pass. This is shown in Fig. 2.1c. Next, we must open the second gated mirror (GM2), again in a time t_{open} less than the round trip time of the cavity, t_{rt}. This time, we apply a positive +100 V pulse to GM2. Now that the electron beam no longer has to be re-imaged onto the sample and recirculated stably in the cavity, the requirements for the opening ringing are less stringent. In the final state (Fig. 2.1e) the pulse is simply released onto an imager from the cavity. After this, the pulses can stop being applied, and the system slowly reset to state (a).

Figure 2.1 shows a timing diagram of this process, allowing us to think clearly about the system requirements for such a cavity. Each grey dotted line corresponds to a single round trip, or time t_{rt}. Each cycle starts when an electron packet is generated by the pulsed source shown by the green START line in Fig. 2.1, which for our purposes we set to a repetition rate of 1 MHz. GM1 Trigger and GM2 Trigger the control signals for the system which start opening and closing GM1 and GM2 respectively. GM1 State and GM2 State are the actual voltages of the mirror, and show the finite transition times of the system t_{close} and t_{open}. Note that we flip the sign of the plot to show a rising edge as closing, since that corresponds to the energy barrier the negatively charged electron sees. t_{prop} refers to the time between setting the mirror state and it physically changing. This is determined by the delay time from the computer control to the switching circuitry, the propagation time of the switching circuitry, and the propagation time of the high voltage signal to where the electron sees. The term t_{jitter} refers to the total jitter time from the electron generation to the closing of the cavity, and is comprised of uncertainty from the electron generation to clock, signal propagation, and pulse generation. Electron State refers to whether or not the electron is in the recirculating cavity, and is simply there to clarify the cavity operation.

In order to properly in-couple the electron, we must set t_{sync} to equal $t_{arrive} - t_{prop} - t_{jitter}$, with t_{jitter} set as the threshold for the number of successful in-couplings given unavoidable system jitter. For our purposes we set this so that more than 99% of in-couplings are successful. Depending on the rise time of the switching pulse, we have an in-coupling window given by $t_{window} = t_{rt} - t_{close} - t_{jitter}$, where t_{close} is the closing time to achieve a specified voltage error (in our case less than 1%). The larger this window, the more time we can have to in-couple current to the cavity, and the less reduction we have in overall system current, shown in Eqn. 2.1, where t_{rep} is the repetition period of the pulsed source and I_{gun} the standard TEM gun current. This assumes the pulse length is perfectly length t_{window}. This current estimate neglects concerns for decoherence from space charge effects in the cavity, especially in regions

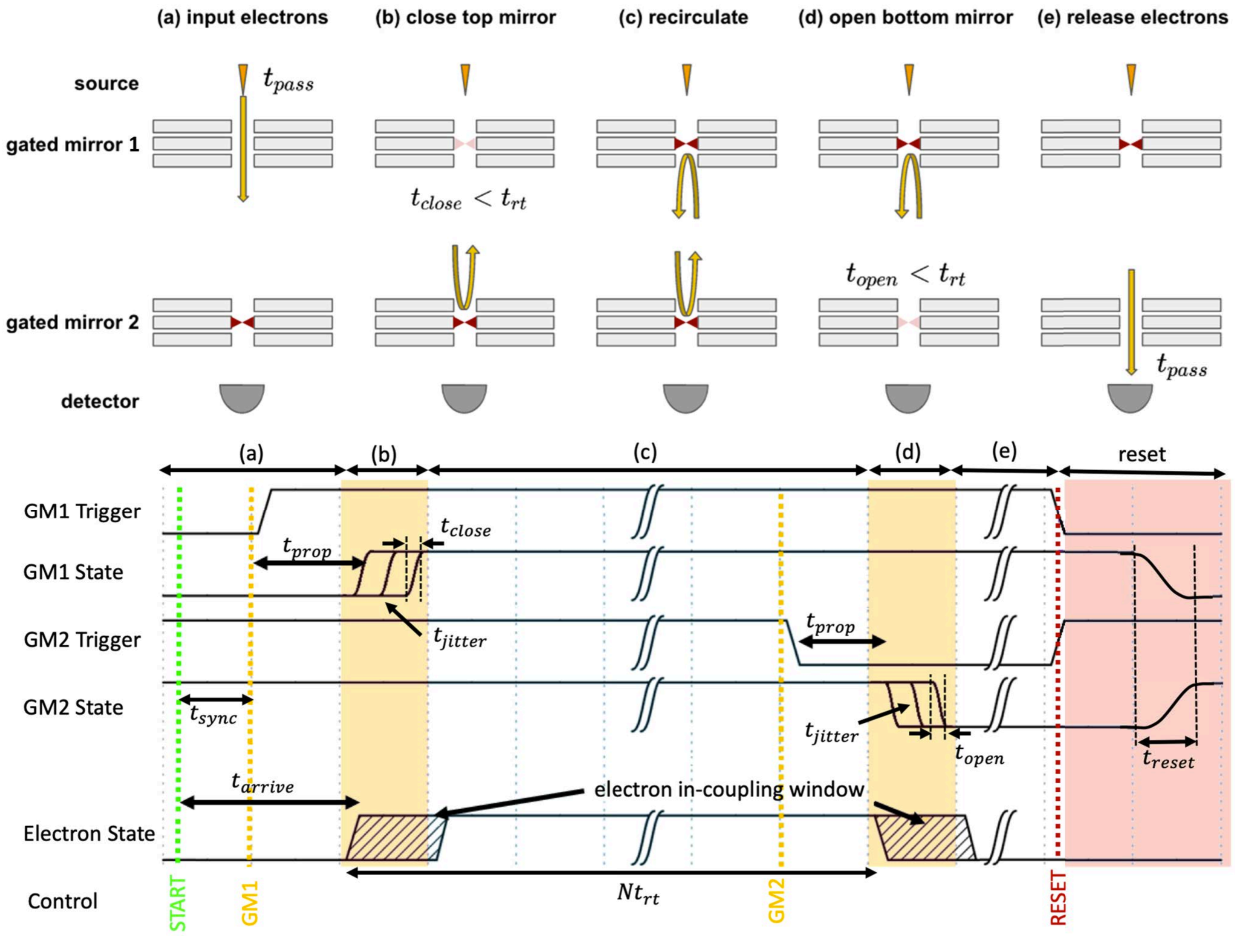

Figure 2.1: Timing diagram of a gated electron mirror, with the various states and transitions labeled. Each heading (a-e) responds to the 5 stages discussed, along with the resetting state. Each dotted line segment corresponds to a the round trip time of the cavity, t_{rt}. (a) The input state, where the top gated mirror GM! is held open, and GM2 is held closed. (b) The capturing of the electron in the cavity, where the electron reflects off GM2 and we must close GM1 before the electron reaches it in time t_{rt}. (c) The recirculating phase, where the electron loops in the cavity for a predetermined time set by the round trip time and desired number of passes. (d) The releasing phase, where we open GM2 before the electron hits to out-couple the electrons without distorting them. (e) The measuring phase, where we detect the electrons to observe a quantum enhancement. The transitory states are highlighted in yellow for the critical opening and closing of the cavity, while the resetting is highlighted in red.

where the electrons slow and reflect. We set our recirculating time as Nt_{rt}, with N being the number of round trips, leading to $2N+1$ passes in the microscope. We set the GM2 trigger to be Nt_{rt} after the GM1 trigger. Finally, we set our reset trigger as close to the cavity being opened as possible, trying to minimize the total reset and state (e) time to increase the total microscope repetition rate. Note that depending on the delays of the system, signals START, GM1, GM2, and RESET may not bee in the order specified.

$$I_{\mathrm{rt}} = \frac{t_{\mathrm{rep}} - (2N+1)t_{\mathrm{window}}}{t_{\mathrm{rep}}} I_{\mathrm{gun}} \tag{2.1}$$

In practice, the cavity will have a round-trip time of approximately 10 ns, and will operate at a 5 MHz repetition rate (though for fewer passes, faster repetition rates would be better to preserve current). We would like to have the ability to go from 3 to 15 passes, meaning the pulse widths will have to be from 30 - 150 ns, since for the single-pass state we do not have to switch the cavity at all as in traditional TEMs. Thus, for our purposes, we require two pulsers: one negative edge pulser achieving -100 V pulses 1% error in under 10 ns, and a positive +100 V pulser with less stringent error requirements still switching in less than 10 ns. These pulsers must be coupled to lenses operating at 10 kV. The faster, higher voltage, and lower error these pulsers are the better, which motivates the rest of our work.

2.2 Approaches to Fast Pulsing

Nanosecond, high-voltage pulses have broad application in in the physical sciences, ranging from their use in optics for driving Pockels cells and piezoelectric actuators [40], to their use in deflecting and gating electrons or ions in nuclear science, spectroscopy [41], and charged particle optics [42, 43]. In the past, these fast pulses have been generated by a wide variety of technologies such as silicon power FETs [44, 45, 46], avalanche transistor circuits [47, 48, 49], step recovery diodes [50], non-linear transmission lines [51], spark gaps [52], and laser-triggered semiconductor gaps [53, 54]. Various reviews and studies exist comparing some of these techniques [55, 56, 57], and most recently the use of nanoplasmas [58] has given record switching performance.

While technically achieving pulses fast and high-voltage enough for the operation of a gated mirror, these technologies have various trade offs that must be balanced. Some downsides are simply inconvenient, such as cost, complexity, short lifetime, or difficult control. Others issues reduce the throughput of experiments and may limit application beyond proof-of-concept demonstration, such as low repetition rates, large jitter, and short maximum pulse widths. In deciding an appropriate technology for use, these must be considered case-by-case. For example, spark gaps, though capable of generating 100 ps pulses on the order of 100 kV, are limited to repetition rates on the order of a few KHz, which, as shown by Eqn. 2.1, would reduce the effective current in our system, and thus imaging times, by over four orders of magnitude.

However, all of these pulse techniques have a common issue that makes them unsuitable to use directly for driving a gated electron mirror: ringing. This persistent ringing prevents the 1% accuracy threshold required for our QEM cavity to function properly. This ringing stems from two sources: parasitic inductances and capacitances intrinsic to the pulse generators themselves, and impedance mismatches between the $50\,\Omega$ driving input lines and the gated mirror load.

Ringing in the driving pulse using traditional high voltage techniques mentioned above can be addressed with low-pass filtering, such as a Butterworth filter, which truncates higher-frequency components to the accuracy required while slowing the transition speed [59]. This is shown schematically in Fig. 2.2a. An alternative approach that does not reduce transition speeds as much is to use resonant filters on the output, which selectively block out the parasitic resonances, shown in Fig. 2.2b. However, this is difficult to implement, especially at the high voltages required, and further difficulties are introduced by the requirement of being able to adjust the pulse width from 30 ns to 150 ns, which changes the frequency content of the pulse.

Impedance mismatch between input lines and the mirror, which causes ringing in the load due to the mirror acting as a resonator, can be addressed in four ways. The first, easiest approach is to bring the pulser close to the load. However, due to the size of the pulsers, as well as their thermal dissipation, this is not possible for a gated mirror held under vacuum. A second simple approach is to simply shrink the mirror electrodes. This shifts the resonances developed over the length scale of the load up, meaning they will be less excited by a pulse of a given bandwidth. Another, more sophisticated approach would be to make the mirror roughly $50\,\Omega$ by engineering its geometry into a parallel plate structure. However this approach, which is commonly used in deflector designs, has many practical difficulties when applied to a gated mirror. Examples include the need to drive the mirror at more than 10 keV, which requires tapered electrodes near the the insulator connections, and complexities from having a hole in the structure.

The fourth, most complicated approach, is to use resonant matching, either with lumped elements or strip-lines, to selectively match each frequency component of the pulse to $50\,\Omega$. If the repetition rate of the pulsing is fixed at say 5 MHz, this means that we need to manipulate frequency components at 5 MHz intervals to achieve a given pulse shape. However, given our need for sub-10 ns transitions to 1%we need more than 500 MHz of bandwidth, meaning we theoretically need to account for over 100 frequency

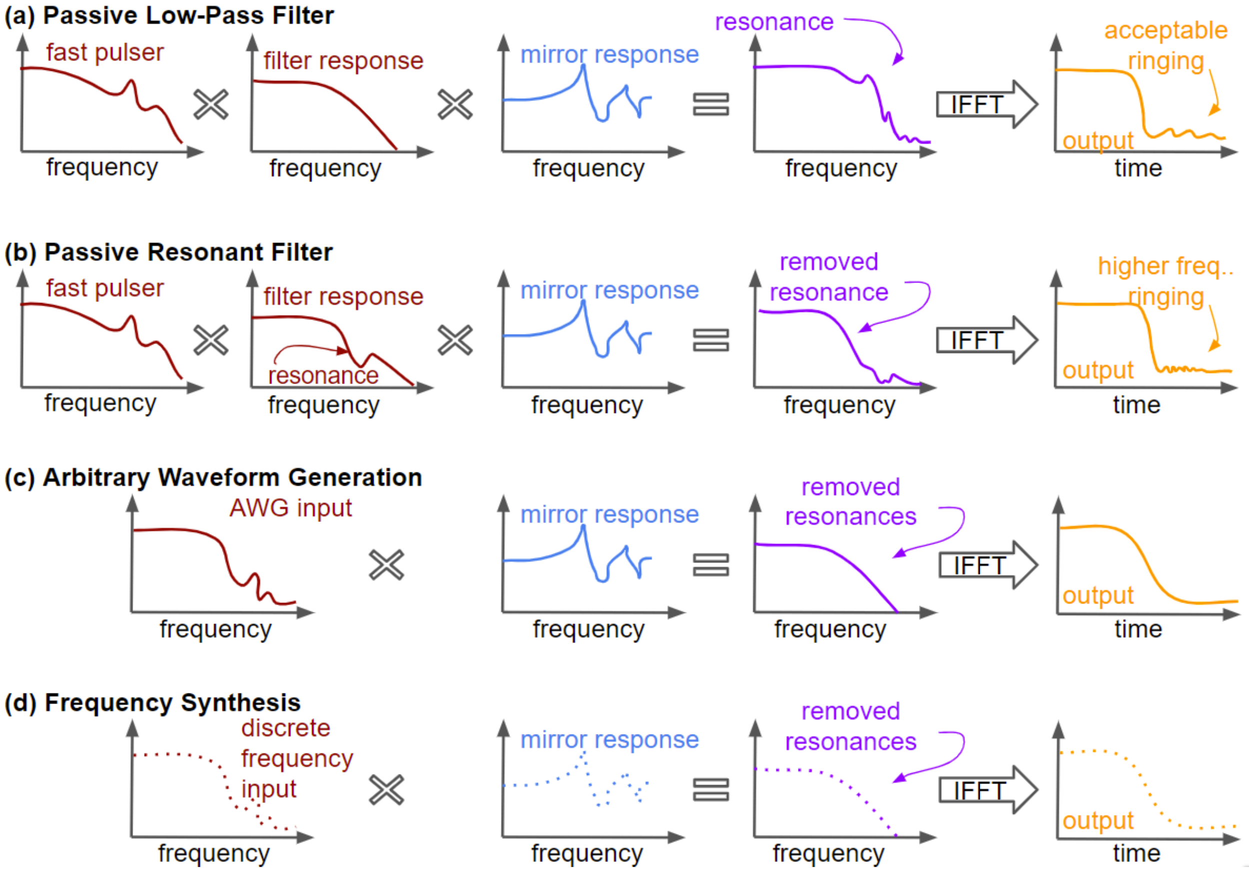

Figure 2.2: Approaches to precision high frequency driving. (a) Traditional low-pass filtering, where the entire edge is slowed to remove ringing in the driving and avoid load resonances. (b) Resonant filtering, where resonances and ringing components are selectively removed, allowing faster edges. (c) An AWG approach, where predistortion of the pulse allows for active removal of ringing and resonances. (d) Frequency synthesis approach, where we mix many discrete frequencies (shown as dots) to reconstruct a waveform at a given repetition rate.

points still. Granted, this is greatly simplified by fact that there are only a handful or resonances in a real load that we need to fit the magnitude, phase, and frequency of, but this problem is still very difficult due to the interaction of difference resonances. Again, the fact that we hope to adjust the pulse width and repetition rates for optimal performance complicates this as well and means separate filters for each pulse length would likely be required. One positive note on this technique is that it could probably be used in combination with the resonant ringing filtering approach, but this complicates the design still further.

Another approach would be to totally abandon the use of traditional fast, high voltage pulsers and instead use modern digitally controlled waveform generators and power amplifiers. These offer a possible solution to this filtering problem, since in this case we can simply program in the required frequency components without worrying about complicated interactions. This also allows us to dynamically adjust both repetition rates and pulse widths as required. This could be achieved either by the use of frequency mixing at the given repetition rate to achieve a desired arbitrary pulse (shown for discrete frequencies in Fig. 2.2d, or through the use of fast time-domain sampling from an arbitrary waveform generator shown in Fig. 2.2d. Due to the huge amount of frequency components required of a mixing approach (more than 100, calculated above) the AWG approach seems much more feasible. Commercial AWGs exist with bandwidths of 50 gigasamples per second, such as the Tektronix AWG70000B, although they generally output at most 5 volts. Power amplifiers rated to over 100 V with bandwidths up to 500 MHz also exist, such as the ZHL-100W-GAN+ from MiniCircuits, which address this problem. Many concerns still exist with this approach, such as the stability of AWG, drift in the system, and amplifier noise, and it is an active area of research in the QEM collaboration [39, 60]. An alternative approach to power amplifiers would be to have impedance transforming lines going from $50\,\Omega$ to $1\,\mathrm{k}\Omega$, which would increase the line voltage from 5 V to 100 V, at the expense of complicating the structure and introducing more system resonances. All of these approaches are compared in Fig. 2.2.

In this work, we take a completely different approach to switching of the gated mirror, taking advantage of emerging high-speed and high-power Gallium Nitride field effect transistors (GaNFETs) and using them directly as switches. While GaNFETs have been used extensively for high-efficiency power converters [61], amplifiers [62], and pulsed lasers [63], we demonstrate that these devices have the potential to also switch a gated electron mirror due to their sub-nanosecond rise times and $>$ 200 V voltage ratings. These circuits are also simple to control due to their FET topology, with single-shot pulsing triggered by a 5 V logic inputs up to a repetition rate of 60 MHz which allows us to easily set both the pulse width and repetition rate of our mirror without any tuning. The high power efficiency and low thermal dissipation of these circuits also offer advantages in operation, leading to small form factors that are compatible with vacuum environments. This vacuum compatibility means that these circuits can be integrated directly into gated electron mirrors, removing the need for impedance matching by removing the need for transmission lines and allowing us to simply damp the gated mirror as an resistor-inductor-capacitor (RLC) load with minimized parasitics due to its small size.

Chapter 3

Design of Gallium Nitride High Voltage Pulsers

Wide bandgap semiconductors such as Gallium Nitride (GaN) have long been considered excellent candidates for power electronics due to their ability to withstand voltage and currents far beyond that of silicon, low channel resistances, and high temperature compatibility [64]. In recent years, GaN on silicon technology has emerged as a low cost and robust option with commercial products that have small gate and output capacitances, optimized packages to minimize parasitic inductances, and a wide variety of current and voltage ratings [65]. Along with these advances, various fast single-sided and half-bridge drivers with sub-ns rise times, 7 A of peak drive current, 60 MHz repetition rates, and 2.5 ns propagation delays have been demonstrated [66]. Together, these offer the possibility of few-nanosecond switching of hundreds of volts and tens of amperes, ideal for application to a gated electron mirror.

In this section, we first validate the capabilities of these GaNFET circuits, demonstrating switching in under 1 ns of up to 200 V. We optimize the circuit design, layout, and filtering to minimize circuit parasitics and ensure vacuum compatibility. Using high voltage passive probing, we demonstrate 100 V transitions and ringing-free switching of this circuit, and test the maximum power of such circuits. Next, we connect the circuit to an oscilloscope through a decoupling capacitor to avoid introducing probing artifacts to our measurements and see the transition with as little perturbation as possible. We use this same approach to approximate real distributed loads as well. Finally, we share designs for a double sided GaNFET pulser, and details for the assembly of such circuits.

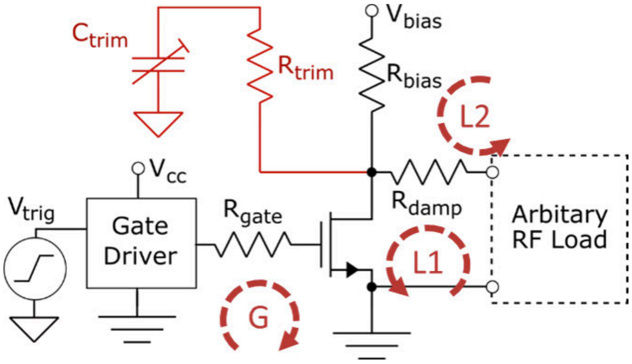

Figure 3.1: Circuit diagram for the GaNFET, where the gate driver is the LMG1020, and GaNFET the EPC2012C. R_{gate} damps the gate turn on loop (G), R_{damp} damps the fast load loop (L1), and R_{bias} sets the power usage and load recovery time loop (L2). The optional trimming circuit in red allows for fine tuning of the load damping.

3.1 Single-Sided Circuit Design

In order to validate the possibility of GaN for switching a gated electron mirror, we first designed a testing circuit from the LMG1020 driver from Texas Instruments along with the EPC2012C enhancement mode GaNFET from the Efficient Power Corporation. The basic circuit design is shown in Fig. 3.1. The load is held to potential V_{bias} until the gate driver is triggered by V_{trig}. When the driver is triggered, the gate driver outputs a high current signal through R_{gate} to turn on the GaNFET by charging its gate as shown in loop G. Charge is then shunted out from both the GaNFET's parasitic output capacitance and the arbitrary load through R_{damp} into ground (loop L1), bringing the load bias to zero. When the GaNFET is shut back off, V_{bias} pulls the voltage back up through R_{bias} in loop L2, though this transition is significantly slower due to the larger value of R_{bias}, which limit power dissipation circuit when the GaNFET is on. If we wanted to speed this up, a high voltage P-channel silicon MOSFET could be used in place of the resistor, though this would require active control. The resistors R_{gate} and R_{damp} are also used to set the turn on time and damp the ringing for the FET and the load, respectively. A tunable snubbing circuit, based on a trimming capacitor as shown in red, was incorporated to ensure that the transition was critically damped, since the RF damping resistors used had values too coarse to precisely damp the circuit.

The full circuit used is shown in Fig. 3.2a, with part numbers labeled. The power supply is based on the TPS7A4700RGWT (Texas Instruments), though any low-noise direct current (DC) supply will suffice. In order to minimize switching times and ringing, significant care was taken to choose capacitors with high self resonant frequencies (SRFs) and low equivalent series resistances (ESRs) for the driving circuitry. We placed the capacitors as close to the LMG1020 driver as possible, as shown in Fig. 3.2b. We used the

Label(s)	Value	Manufacturer	Part Number
C6	$0.1\,\mu\text{F}$	Murata Electronics	NFM15PC104D0J3D
C7	$1\,\mu\text{F}$	TDK Corporation	C0510X5R0J105M030BC
C8	$20\,\text{pF}$	Vishay Vitramon	VJ0603D200JXPAJ
C9	8 - $40\,\text{pF}$	Knowles Voltronics	JZ400HV
R1, R2	$2\,\Omega$	Vishay Dale	CRCW02012R00FXED
R3	$1\,\text{k}\Omega$	Bourns Inc.	CR0603-JW-102ELF
R4, R5	$10\,\Omega$	Vishay Thin Film	FC0402E10R0BTT0
R6, R7	$25\,\Omega$	Vishay Thin Film	FC0402E25R0BTT0
J2, J5	$12\,\text{GHz}$	Murata Electronics	MM5829-2700RJ4

Table 3.1: List of components from schematic shown in Figure 3.1

combination of a $0.1\,\mu\text{F}$ 0402 feed-throug capacitor (TDK YFF15PC0J474MT) closest to the driver and a $1\,\mu\text{F}$ 0204 (wide package) capacitor (TDK C0510X5R0J105M030BC) slightly further out to provide a low-impedance drive loop and maintain biasing to the driver respectively. The temperature stability of the capacitors was sacrificed in order to minimize the package sizes used, with X5R ratings chosen rather than X7R. Low heat dissipation in our system and good thermal grounding ensured this did not cause problems in our setup due to changing capacitance with temperature. The most relevant parts and part numbers used are listed in table 3.1.

We also sought to minimize the size of the drive ground loop in order to minimize parasitic inductance in our circuit. This was done by the use of a thin two-sided $100\,\mu\text{m}$ Kapton substrate (PCBWay) with a direct ground return trace running under from the GaNFET source pad directly to the driver ground as shown in Fig. 3.2b.

Damping was implemented using high-frequency thin film resistors ranging from $10\,\Omega$ to $100\,\Omega$ (Vishay Thin Film FC Series). Though the 0.125 W power rating would indicate they can only operate to 1.25 MHz (assuming 100 V switching of $10\,\text{pF}$), we found the resistor continued working to 5 MHz. Using better heat-sinking and multiple damping resistors in parallel to spread out the dissipation, we found this circuit could operate up to 20 MHz, the maximum repetition rate we tested. This performance was limited by the resetting time of R_{bias}, and we began to see the voltage failing to return to zero if the repetition rate was too high. In the test cases shown, we used two parallel $10\,\Omega$ resistors for damping, which we calculated as roughly the critical damping point. This testing was done using a LeCroy PP007-WR 500 MHz probe, which slowed the response but ensured we could not damage the oscilloscope.

We were also able to make these circuits vacuum compatible. This was done by using silver-based solder (SMD291SNL-ND from Chip Quik Inc.) and low-out-gassing Kapton substrates (PCBWay). After assembly, the circuits were mounted on Oxygen-free high conductivity (OFHC) copper, sonicated in PCB

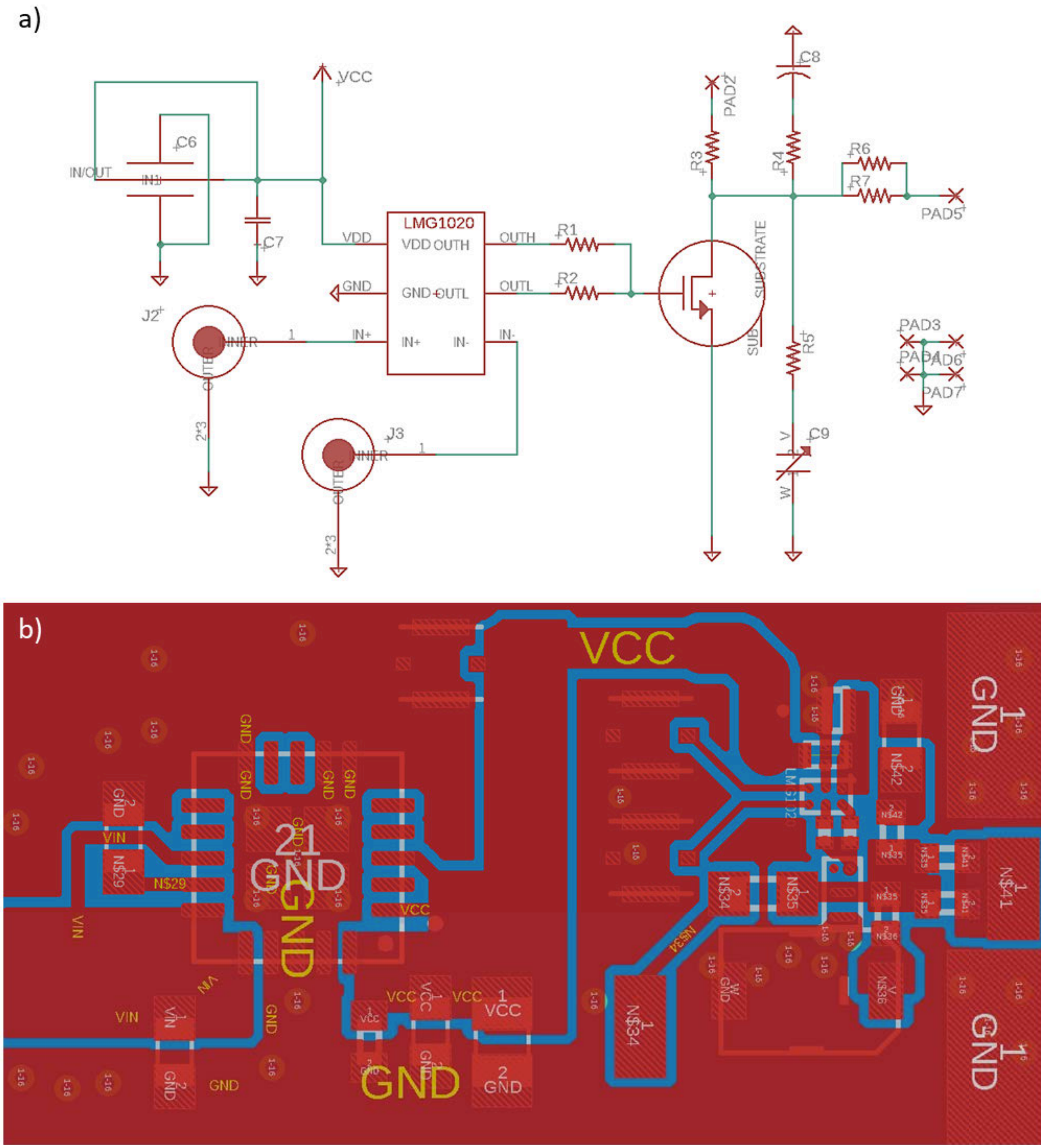

Figure 3.2: Test-bed circuit schematics and layout. (a) The main part of the circuit design, excluding the power supply which is represented by VCC. (b) The layout. The active region is to the right. Note the proximity of the input capacitors to the LMG1020 and the minimized ground return path placed directly under the drive loop to minimize inductance.

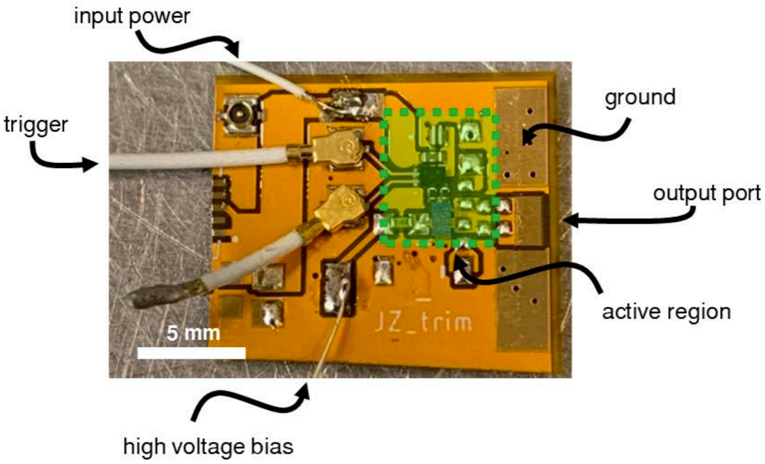

Figure 3.3: The physical layout of the circuit mounted on a flexible Kapton substrate. The highlighted green region shows the active portion of the circuit which is $<0.25\,\mathrm{cm}^2$.

cleaning solution (PELCO Kleensonic™ APC) rinsed by water and IPA, and finally encased in thermally conductive and electrically insulating ceramic epoxy (EPO-TEK H70E Thermally Conductive Epoxy).

Figure 3.3 shows the realization of this circuit on a $100\,\mu\mathrm{m}$ thick Kapton substrate. The green shaded region shows the active area of the GaNFET, driver, bypass capacitors and damping, taking up less than $0.25\,\mathrm{cm}^2$, while the power supply makes up the rest of the circuit and can be placed off-board. No difference was seen between having the power supply directly on the board or coupled in via a coaxial cable. The circuit shown is not yet mounted to OFHC copper or encased in epoxy.

A detailed description of the assembly is described at the end of this chapter.

3.2 Circuit Testing

We then tested the response of the circuit with a 500 MHz, $10\,\mathrm{M}\Omega$ probe (LeCroy PP007-WR) on a 2 GHz LeCroy 6200A oscilloscope. The exact contact, using a blade ground attachment, is shown in Fig.3.4a. The setup used is shown in Fig. 3.13 in the testing section at the end of this chapter.

The undamped response at R_{damp} = 0 Ω shows a full transition in less than 1 ns, but suffers from significant ringing. This is shown in Fig. 3.4. Note that there is a second spurt of ringing around 12 ns. Given the cable is 1.2 m long, and the speed of light in the cable is 66% the speed of light in vacuum, we get that a return reflection would occur in 12 ns, leading us to believe this is the cause despite the engineering of the cable by the manufacturer to prevent return reflections. We believe the high power of the switching makes this small, 2% reflection (which is not of interest for standard applications of lower voltage or speed) visible.

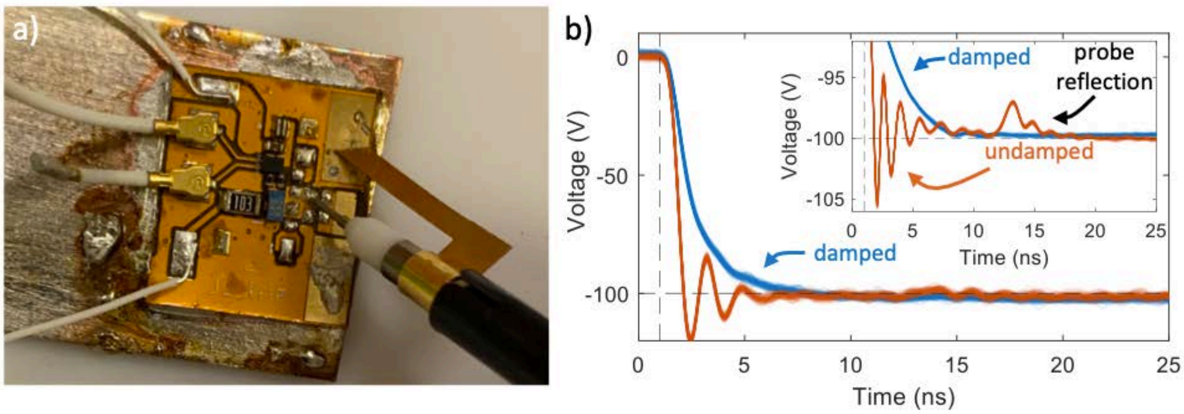

Figure 3.4: Probing of the circuit. (a) Probing using a high impedance high voltage probe. (b) Output of probe. The undamped result shows significant ringing and a resurgent ringing we attribute to probing cable reflections. The damped result shows fully removed ringing in a 3 ns transition.

The near-critically damped response obtained at R_{damp} = 25 Ω and by tuning the trimming circuit (setting R_{trim} = 15 Ω and $C_{trim} \approx 40pF$) shows a transition from -10 V to -90 V (10% to 90% of the amplitude) in less than 3 ns with no residual ringing. More significantly, the critically damped circuit is capable of reaching 5% of the final value in under 4 ns, and 1% accuracy in 6 ns as shown in the top right inset of Figure 3.4b. We note that these circuits were successfully driven up to 200 volts. However, to ensure we did not damage the probe and oscilloscope in the overshoot cases, the maximum voltage we used while measuring was 100 V.

This measurement established the approximate speed and voltage capabilities of our circuit, but does not accurately represent what a lumped load would behave as. To remove probe artifacts, as well as most accurately simulate a real load of short length, we directly hooked the circuit up to the oscilloscope, as shown in Fig. 3.5a.

This direct connection was done instead of the more standard approach of using active probing, since most active probes are not rated for high enough voltages for our testing and the full system is hard to analyze. Also, as will be explained in Chapter 4, the large length scale of a probe and its cable interferes with our attempts to approximate the system as lumped elements, meaning that the damping of the system is not straightforward. A comparison of the two measurement approaches is shown in Fig. 3.6, with the most important difference being the lossy transmission line of Fig. 3.6a. Fig. 3.6b does not have this length scale and so can be reduced to lumped elements. The passive probe also has compensation circuitry consisting of low and high-pass adjustable filtering, which complicates the model, though ideally this is removable through compensation.

However, directly hooking the circuit up to the oscilloscope led to issues with our measurement chang-

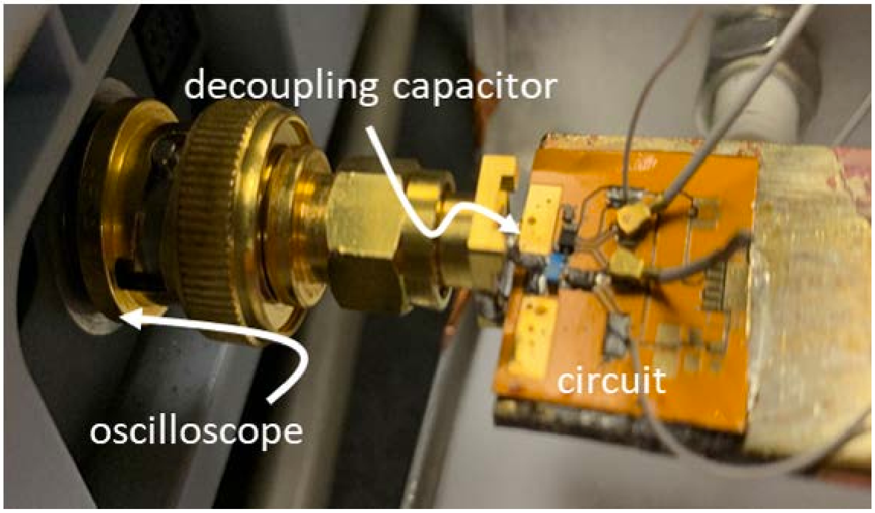

Figure 3.5: Direct hookup of the circuit to the oscilloscope. The PCB is directly connected to the oscilloscope through an SMA connector decoupled by a 2.2 pF capacitor.

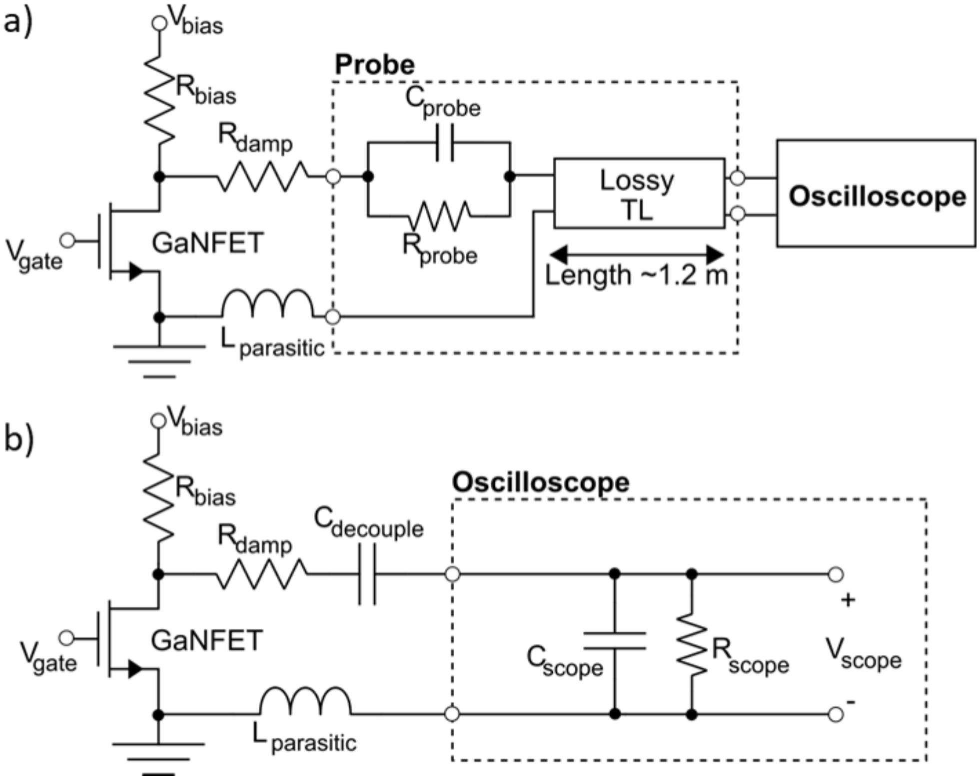

Figure 3.6: Measurement circuit models. (a) is the measurement circuit model using the 500 MHz probe, which has unavoidable transmission line effects due to its length of 1.2 m. For simplicity the compensation circuits are neglected. (b) the simpler model from directly hooking the circuit up to the oscilloscope. Due to the proximity of the circuit to the measuring amplifier, we can neglect transmission line effects. A decoupling capacitor is used to prevent impedance changes the GaNFET sees when switching gains, and to attenuate the input voltage.

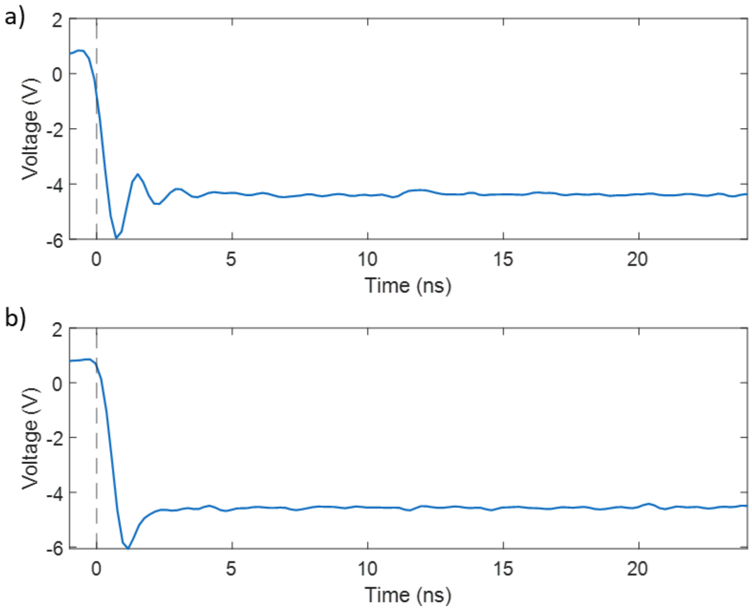

Figure 3.7: Effect of changing gain on the measurement. (a) A trace with a gain of 1.02 V/division. (b) The same trace with a gain of 1.00 V/division. Switching this range causes an audible click in the oscilloscope, likely due to some sort of switched amplifier configuration on the input, which visibly changes the response of the circuit.

ing as a function of the oscilloscope gain. This is demonstrated below in Fig. 3.7a and b for 1 V/division and 1.02 mV/division respectively, and is repeated for other transitions such as from 100 mV/division to 102 mV/division where the waveform changes more subtly. We hypothesize that this is due to changes in the oscilloscope amplifier impedance as we switch gain ranges, which changes what the GaNFET sees. Introducing a small-valued capacitor in series to stabilize the impedance seen by the circuit seems to improve this, though not entirely.

We then measured the decoupled circuit with and without damping. In Fig. 3.8a we used a 2.2 pF capacitor, resulting in a 1:10 attenuation into the 20 pF, $1\,\mathrm{M\Omega}$ oscilloscope load. The resulting load is $2\,\mathrm{pF}$ as seen by the GaNFET. We only drove to 50 V to avoid damage to the oscilloscope, since the ringing overshoot is significant, reaching a peak of -125 V. We measure the ringing to be 1.1 GHz.

Because the GaNFET to oscilloscope distance is much smaller than the wavelength of the largest transition frequency, we can simplify this circuit into a resistor-capacitor-inductor (RLC) circuit model. Knowing the ringing frequency (f) and that our total capacitance (C) is 3 pF (2 pF from the scope and 1 pF from the substrate), we use $L \approx \frac{1}{(2\pi f)^2 C}$ to estimate an inductance of 7 nH. Given RG-58/U cable has an inductance of 3.67 nH/cm, this would mean our circuit is 2 cm from the oscilloscope amplifier, which seems to be on the order of the dimensions of our circuit. If we have an RLC-type circuit, this would then mean we would

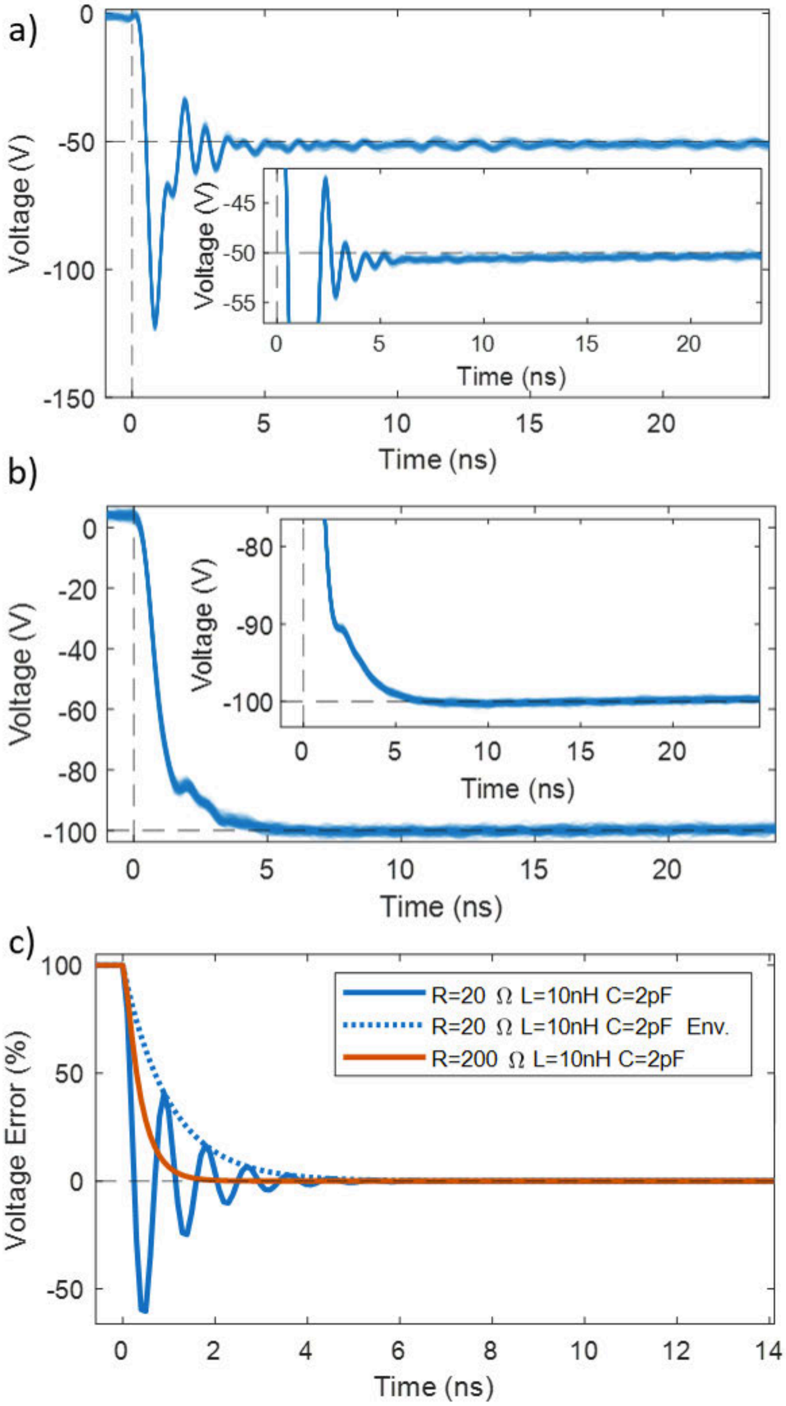

Figure 3.8: (a) A 2.2 pF decoupling capacitor with no damping biased to 50 V (b) The same decoupling, with 200 Ω resistive damping. (c) RLC-model comparison to the curves with and without damping.

expect to need total damping of $R = 2 * \sqrt{\frac{L}{C}}$, which is $96.6\,\Omega$.

We the apply a $100\,\Omega$ resistor in series with the decoupling capacitor, making this circuit slightly over-damped. This results in a transition from 10% to 90% of the amplitude in less than 1.5 ns with no residual ringing. More significantly, the critically damped circuit is capable of reaching 1% of the final value in under 3 ns. This demonstrates that the GaNFETs are potentially fast and high-voltage enough to drive a gated electron mirror with very high accuracy.

3.3 Double-Sided Pulsing

Finally, we extended this design to a double-sided pulser using bootstrapped GaNFETs based on the LMG1210 driver from Texas Instruments. The basic operation of this circuit is described in Fig. 3.9. We begin by describing the low side loop, which is similar in operation to the first circuit based on the LMG1020. We begin with both GaNFETs off, isolating the gated mirror node at HS. First, V_{LI} is set high while V_{HI} is set low. This turns off the top GaNFET U_t and turns on the bottom one by shunting current though loop G1 into the gate of U_b. This allows the load to be pulled to ground through R_{damp}, which damps the circuit. At the same time, loop B1 pulls current from V_{cc} through diode D into capacitor C, charging it to 5 V (V_{cc}) above the level of pin HS.

Next, we shut off the bottom GaNFET U_b by setting V_{LI} low, again isolating the gated mirror until needed. After a set delay, determined by the number of round trips in the cavity, we set V_{HI} high, which begins putting current through loop G2 into the gate of U_t. As the FET opens, HS is pulled high to V_{bias}, and because the diode D shuts off, capacitor C is able to hold the high-side GaNFET U_t's gate signal (HO) to be 5 V above V_{bias}. This keeps the GaNFET U_t open, allowing the load to be pulled high through R_{damp}. Once this is completed, we set V_{HI} to low, and the cycle repeats.

As before, we show the schematic and layout in Fig. 3.10a and b, and the parts used in this circuit in Tab. 3.2. The primary difference between the LMG1020 and LMG1210 based designs stem from the need for a bootstrapping reservoir to hold the upper GaNFET to the gate potential, and the need to have a low-impedance charge reservoir across V_{bias} to sink into the gated mirror when generating the positive edge. This bootstrapping circuitry necessarily adds to the physical size of the layout, and internally in the driver, slowing performance. The required biasing capacitors must also be carefully chosen to minimize self-resonances that slow turn on times. The layout and part selections address both of these factors. Other details include the use of biasing capacitors on the input, selection of low-ESR capacitors for the internal regulator, and use of a Schottky diode and a feed-through capacitor to minimize reverse recovery time,

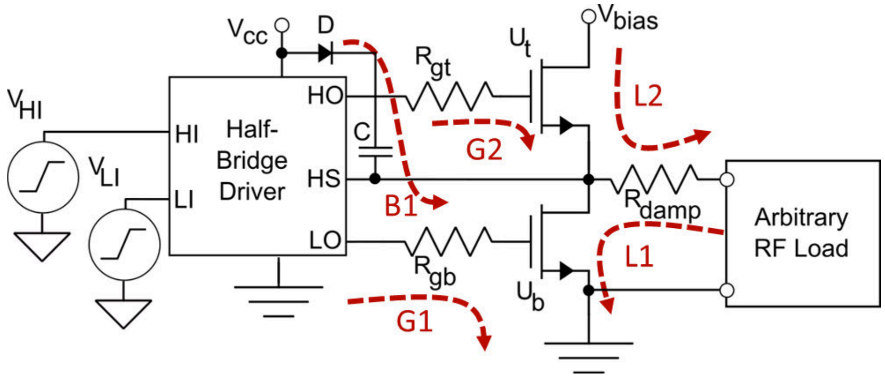

Figure 3.9: Operating description of the bootstrapped GaNFET circuit, allowing for both positive and negative voltage transitions.

Label(s)	Value	Manufacturer	Part Number
C1	10 µF	TDK Corporation	C3216JB1C106K160AA
C2, C3	1 µF	TDK Corporation	C2012X7S2A105K125AE
C4	1 µF	Murata Electronics	NFM15PC104D0J3D
C5	0.1 µF	TDK Corporation	C0510X5R0J105M030BC
C6	250 V 0.1 µF	TDK Corporation	CGA4J3X7T2E104M125AE
C7	250 V 0.022 µF	TDK Corporation	C20123X7R2E223K125AA
C8	250 V 330 pF	Vishay Vitramon	VJ085D331KXPAJ
C9,10,11	250 V 100 pF	Vishay Vitramon	VJ063D101KXPAJ
C12	40 pF	Knowles Voltronics	JZ400HV
R1, R2	2 Ω	Vishay Dale	CRCW02012R00FXED
R3, R4, R5	10 Ω	Vishay Thin Film	FC0402E10R0BTT0
D1	10 Ω	Vishay Thin Film	FC0402E10R0BTT0
J1, J2	12 GHz	Murata Electronics	MM5829-2700RJ4

Table 3.2: List of components from schematic shown in Fig. 3.10

voltage drops, and loop inductance.

The response of this circuit is shown in Fig. 3.11, using a passive 500 MHz, 10 MΩ probe (LeCroy PP007-WR) on a 2 GHz LeCroy 6200A oscilloscope as before. The undamped transitions are 2 ns, slower than the single-sided case due to the larger loop inductance of the circuit and the slower driver.

In the following sections on simulating and testing the gated mirror, we will focus on the single-sided topology, since its faster switching leads to more stringent constraints on the design of the gated mirror and damping. All of this analysis applies equally well to the case of this bootstrapped pulser, which is the easier case given the lower frequency content of its switching.

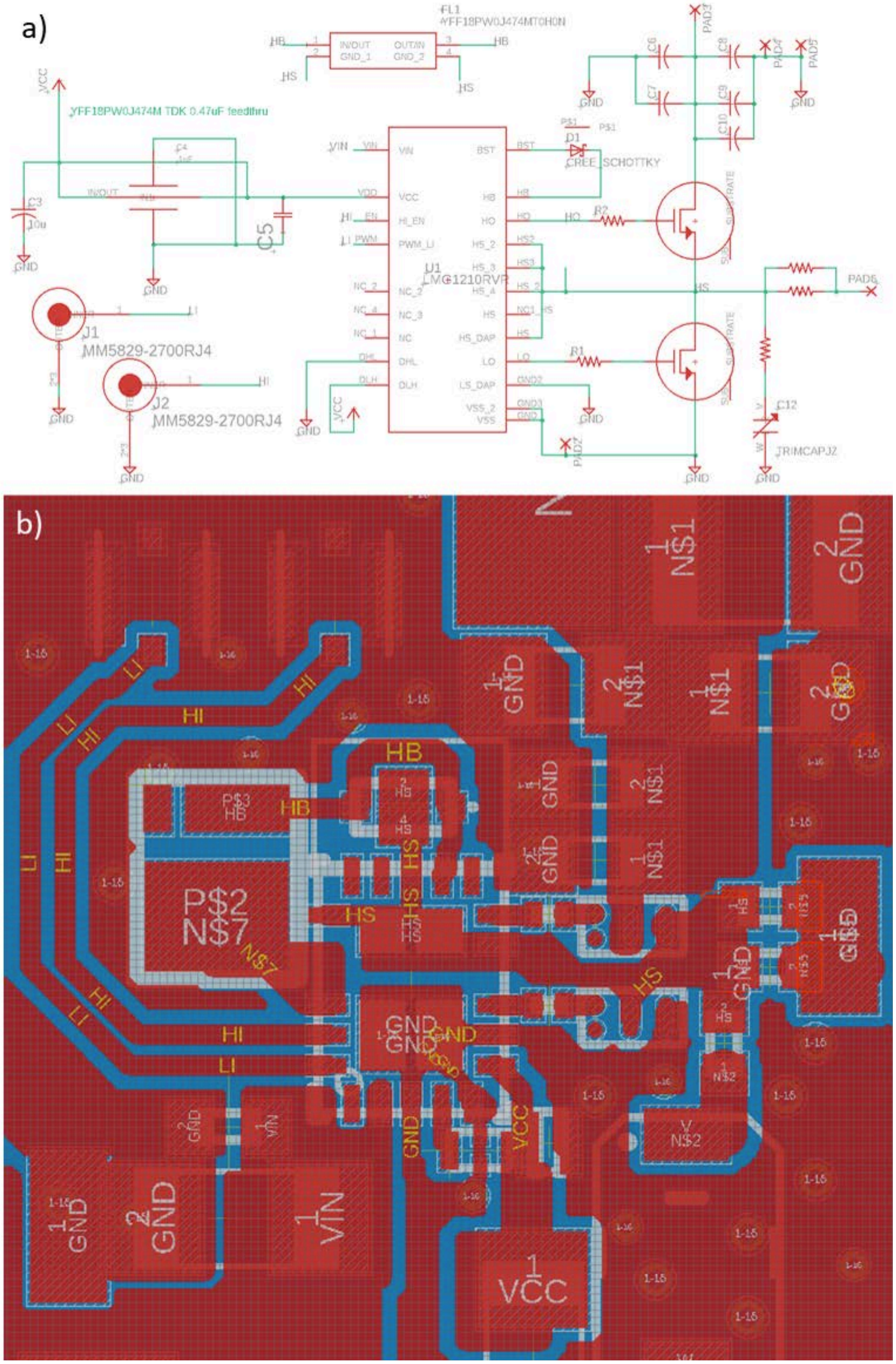

Figure 3.10: Bootstrapped GaNFET circuit design. As before, we sought to minimize ground loop sizes by using small components, thin substrates, and careful placement.

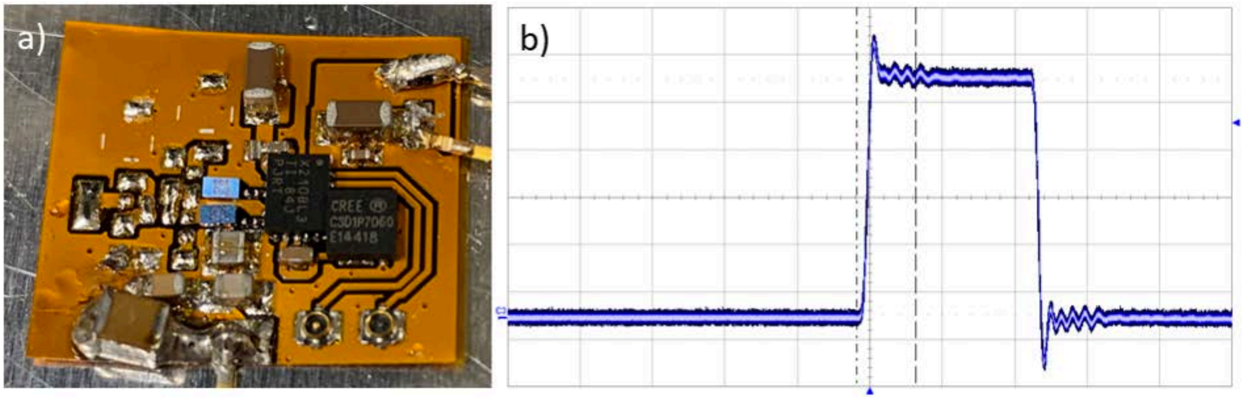

Figure 3.11: Bootstrapped GaNFET Results. (a) The physical circuit, which is significantly larger than the initial topology, taking up less than $2\,\mathrm{cm}^2$. (b) Double-sided pulsing demonstration into a 500 MHz probe. The response is slower due to the larger circuit size. Vertical scale is 20 V/division, horizontal scale is 10 ns/division.

3.4 Assembly Procedure

The following details the construction of this high-speed GaN circuit.

1. First, we prepare our work space. Electrostatic discharge (ESD) safe mats and grounding bracelets are a necessity to get high circuit yields. Preheat the hot plate to 190°C. Preheat a soldering iron to 300°C. Tape the circuit using an easy release masking tape to whatever work surface you hope to assemble it on, as shown in Fig. 3.12a.

2. Next, we use a soldering stencil from the layout given (also from PCBway) and align it using a magnifying glass or microscope to the pattern. Tape one side of the mask as shown with the flipped stencil in Fig. 3.12a. We found aligning to the smallest component pads was the easiest way to do this.

3. Apply a small amount of solder paste to the edge of the mask. Holding the stencil firmly and evenly down, use a straight edge (such as a plastic card) to gently spread the paste over all of the holes, ensuring each hole is covered. Then, pressing more strongly on the card, scrape away any excess material.

4. Remove the stencil, being careful to pop it directly up. Inspect the layout, ensuring there are no solder connections between different pads. If there are, it is possible to correct by breaking the bridges with a fine tip. If the paste is too spread out, wipe the surface clean and repeat. An example of good looking paste application is shown in Fig. 3.12b.

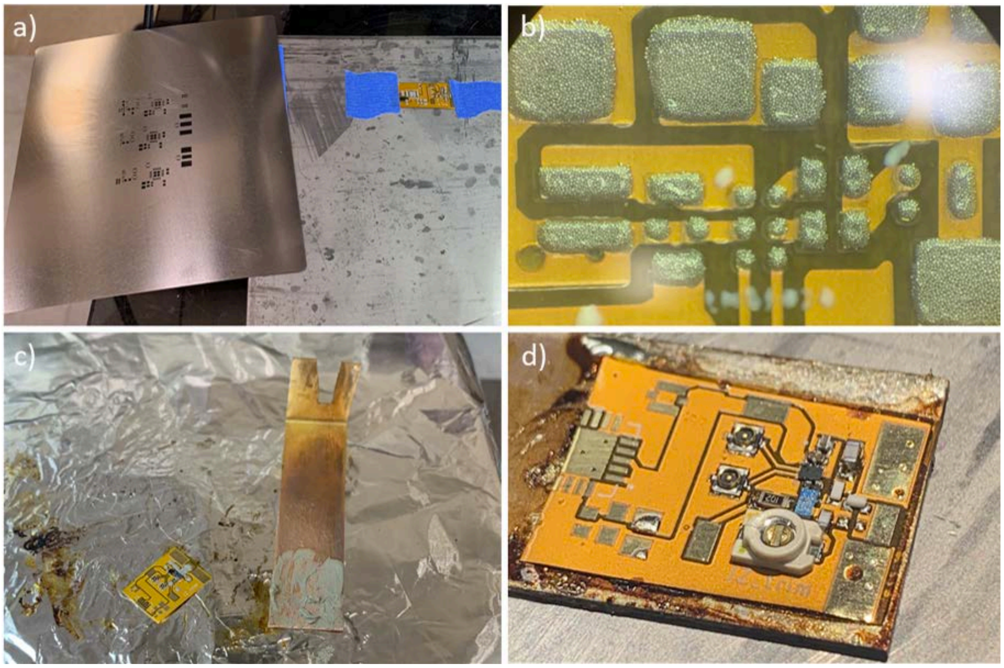

Figure 3.12: Overview of circuit assembly for thermal management and vacuum compatibility. (a) Taping of the circuit to the board, and the stencil attached to the left with tape (flipped upside-down). (b) Solder paste clearly on pads, resulting from a well-aligned stencil. (c) Heating of the circuit on a hot plate to solder each connection. Also shown is the solder spread on the copper mount, which we place the circuit on for heat-sinking. (d) the final circuit without wires, showing successful soldering of the components and bonding to the copper heat sink.

5. Now assemble components. If not already done, make sure to wear an ESD bracelet, or at least ground your tweezers with an alligator clip or something similar. Even the slightest discharge will destroy the GaNFET, causing your FET to be across the source to drain when off. This is especially catastrophic in the double-sided circuit as it can damage your high voltage supply. Other various tips are below.

    - Begin assembling components one at a time. Generally we start with the largest components and work down in size, finishing with the EPC2012c and LMG1020 as their pads are the most delicate and they are the most expensive. The only exception to this size rule is placing R1 and R2, which we generally do fairly early since they are inexpensive and easy to mess up, and it is nice to have space to place them without worrying about knocking the GaNFETs or driver out of place.
    - Various methods exist for stabilizing hands while doing this such as resting your hand on your fingers, exhaling during the final component placement, and avoiding caffeinated beverages the day of trying. Using a clean wipe and alcohol, clean the tweezers after each placement to prevent solder paste from sticking the component to the tweezers.
    - If the component is misplaced, put the tweezers tip onto the PCB to stabilize shaking, and then slide the tweezers tip around to nudge components into place. As long as the component pads make contact with the solder paste on each pad, it should be fine as surface tension will pull components exactly into place.

6. Place the circuit onto the hot plate. If available, place a fume extractor or fan above the hot plate. Increase the plate temperature to 290°C, though this can be adjusted depending on the plate, as long as the PCB does not darken the temperature is not too high. As this happens, you should see the solder begin to melt. Watch the smallest components, especially the LMG1020 and EPC2012c, and make sure the components get pulled into place by surface tension of the solder. If this does not happen, try slightly nudging the components with tweezers to knock them into place. If when you touch the components, there is no action trying to return them to place, they are likely not properly placed, or there is not enough solder.

7. On the piece of OFHC copper you wish to mount your circuit on, spread out the silver solder paste evenly. For our thin heat sink this is shown in Fig. 3.12c. Remove the assembled circuit and place it onto the copper. The solder should harden holding the circuit components in place. Now, place the

entire copper piece onto the hotplate. Wait until the solder melts and the circuit is pulled into place by surface tension.

8. Reduce the hot plate temperature to 190°C. Wait until all of solder re-solidifies. Once this happens, take the soldering iron and apply it to the biasing and power pads and solder on connection wires. Remove the circuit. Clean the circuit with acetone and IPA. If vacuum performance is required, sonicate in PCB cleaning solution given in the materials section. If high repetition rate performance is required, encase in EPO-TEK H70E thermally conductive epoxy (PELCO). The end product should look like Fig. 3.12d.

3.5 Circuit Testing Procedure and Safety

1. Next, we test the circuit. First connect the circuit to ground. Next, attach the high voltage biasing port to a high voltage port. In our case, we used a 150 V piezo supply (Thorlabs model MDT693B) with a $1\,\mathrm{M\Omega}$ resistor tied to ground (for safety and ESD protection) coupled through a BNC cable (rated to 300 V). This high voltage supply is left off until testing. We then turn on the power supply supply. In early tests we used a 6 V power supply (XP Power VEL05US060-US-JA) with the designed regulator circuit. For later tests, to reduce power dissipation in the circuit and it more vacuum compatible, we used a 5 V direct connection from a low noise power supply (Keithley Model 2220). We saw no difference in results using either source.

2. We then hook up the RF ports. We used an SMA-to-JSC adapter (GradConn CABLE 366 RF-200-A) and BNC-to-SMA adapter to get the input signal from the signal generator (Keysight 33250A) to the driving board. For traces shown, we input a 3 v, 100 ns wide pulse with 5 ns rising edges at a repetition rate of 1 kHz. This low rate was chosen to reduce the voltage offset in AC-coupling and reduce thermal effects, though the circuit was tested to 20 MHz, limited by the recharge time of the biasing resistor and breakdown of the biasing. The second input was grounded.

3. We then turned on the high voltage supply, starting at 5 V to ensure the circuit functioned properly. Once this was verified we slowly increased to voltage to the set point. For initial tests we used a LeCroy PP007-WR 500 MHz $10\,\mathrm{M\Omega}$ probe, tested up to 100 V with a blade ground connector, as shown in Fig. 3.13. The probe was compensated using a 1 MHz square wave signal from the oscilloscope.

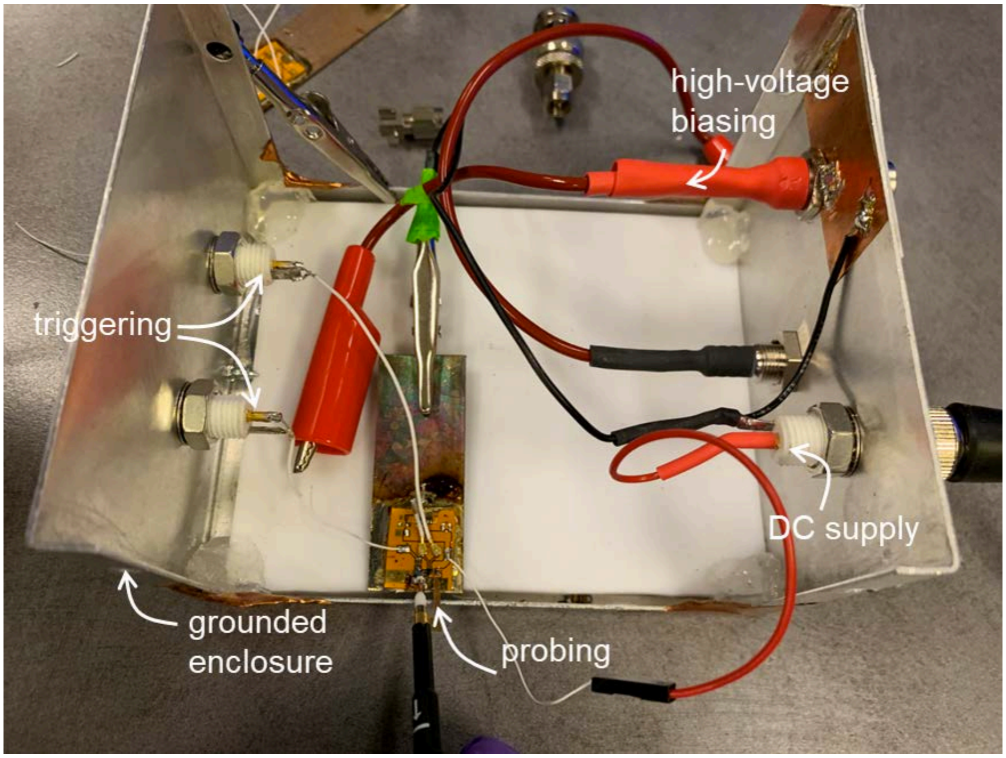

Figure 3.13: Testing setup used, showing shielding, ground insulation, and probing.

4. For the final testing, we directly hooked up our circuit through an SMA connector which we adapted to a BNC connector and inserted into the oscilloscope. This is shown in Fig. 3.5a.

Chapter 4

Simulation of Pulser Switching Performance in Real Loads

In this section, we simulate the performance of several gated electron mirror structures. We then interact these mirrors with a simulation of our GaNFET circuit to validate the GaNFET's switching performance, demonstrating ringing-free critical damping of the mirror. We compare this to results from a low-pass filtering approach. In these simulations, we focus on the single-sided pulser, which is faster and with higher frequency content, although all of this work applies equally well to double-sided pulsers as well. We discuss the theoretical limits to switching speeds for a gated mirror, which is fundamentally set by the length scale of the structures. Finally, we simulate other loads to demonstrate the generality of this GaNFET switching approach.

4.1 Integrated Simulations of a Gated Mirror

In order to validate the performance of the GaNFET pulser for quantum electron microscopy, we simulated its performance when interacting with a gated electron mirror. We chose to do this using frequency-domain simulations. We chose to simulate the mirror in the frequency domain because the gated mirror is a linear time-invariant (LTI) load, and so solving the mirror in the frequency domain gives all information about its performance. Then, by creating a circuit model fit to this, we were able to fully interact it with a non-linear time domain simulation in LTSpice. This approach of combining time and frequency domain simulations dramatically improved simulation speed and performance, as well as gave greater physical intuition to the problem.

The first modeling step of this work was to represent the printed circuit board (PCB) layout and the

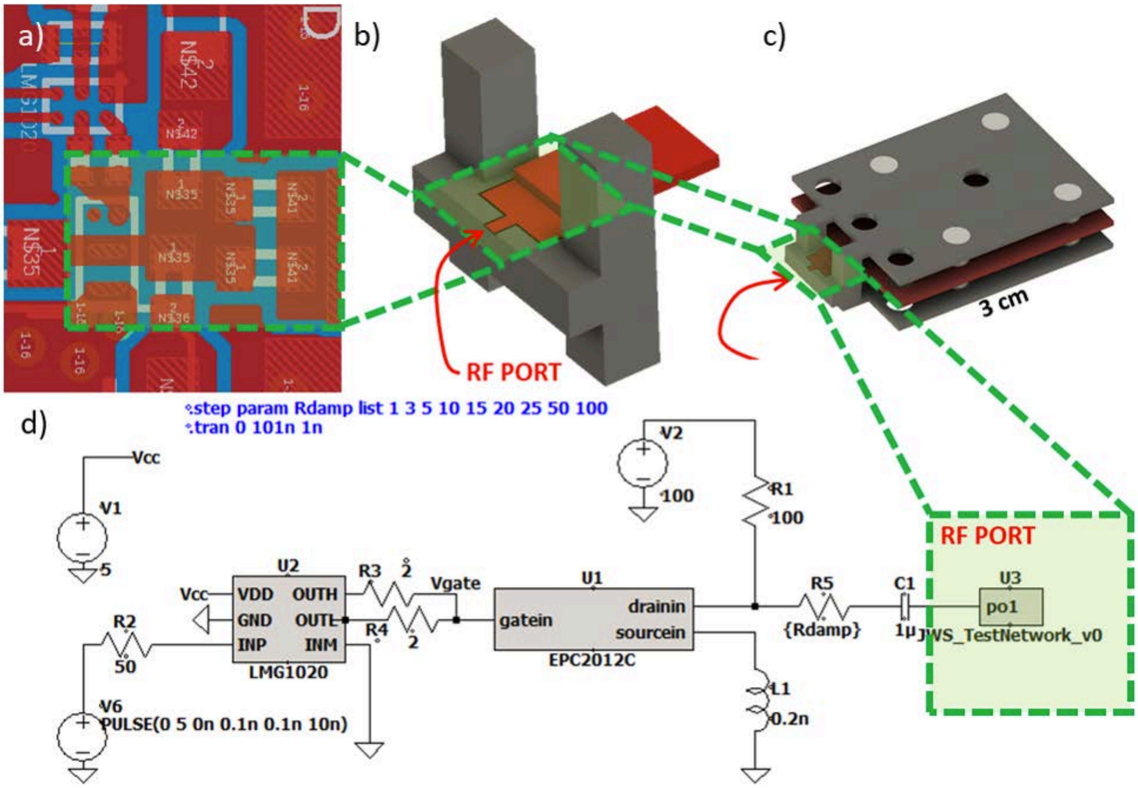

Figure 4.1: Representation of the simulation. (a) A close up of the PCB, with the area treated in the simulation highlighted in green. (b) The simplified PCB model that was used to launch the RF signals in all of the simulations. (c) The RF port attached to the load of interest, in this case the deflector. (d) The SPICE simulation, which interacts the EPC2012C and LMG1020 with the RF port, denoted as JWS_TestNetwork_v0.

load in COMSOL. This was done by extracting the dimensions of the PCB and drain pad of the GaNFET from the layout to a computer aided design (CAD) in Autodesk Fusion 360 and attaching this to various structures we designed. This PCB port model is shown in Figure 4.1a. The process of converting it to a CAD representation is shown in 4.1a-b.

Next, we defined a geometric structure in COMSOL Multiphysics to be excited. We defined three 304 stainless steel plates from Kimball Physics stacked with alumina spacers, with the central electrode (red) receiving the GaNFET excitation as shown in Figure 4.1c where we attach the model to 4.1b. This kind of structure is widely used in electron optics for the fast gating (if the beam enters vertically) and deflection (if the beam enters horizontally) of charged particles. The models of these structures were then imported into COMSOL, and we defined the source and drain of the GaNFET to be our lumped radio frequency (RF) input ports for the simulations.

Next, we developed a circuit model to interact with the mirror. The LTSpice circuit model used is shown in Figure 4.1d. The input to the driver is excited with a $50\,\Omega$ source. This causes a current to go through the gate drive, which is damped by the 2 Ω resistors both on the rising and falling edge. This turns the GaNFET on, which then shunts current from the simulated mirror load (JWS_TestNetwork_v0) through $R5$ and the GaNFET to ground. A 0.2 nH inductor is placed between the GaNFET source and ground to simulate the inductance in that gate drive loop between the LMG1020 and EPC2012C. The inductance value was calculated to be 0.2 nH from analytical approximations [67]. We vary the value of $R5$ with the parameter Rdamp to find roughly the optimal damping for the mirror. Note that the circuit is AC-coupled by a 1 μF capacitor. This capacitor was used because the mirror fitting model model is unable to correctly represent the capacitor's infinite impedance at DC, and so we needed this to ensure correct DC biasing. This mirrors the decoupling used in the oscilloscope measurements of Chapter 3. We explain this further when discussing the mirror-side simulation in Fig. 4.2.

Using the RF Module in COMSOL, we ran a full wave simulation of the structure in the frequency domain, extracting both the field distributions in the load and the port impedance seen by the GaNFET, as shown in Figure 4.2b and 4.2c respectively. As seen in Fig. 4.2b, until 1 GHz, the field distribution is flat and behaves as a single lumped element. At 1.4 GHz, this begins to break down and we see the lowest mode develop. At 3.48 GHz and 7.88 GHz we see higher order modes develop, and the lumped element approximation completely breaks down.

Similar behavior can be seen in the port impedance, shown in Fig. 4.2c. The blue "COMSOL Port" curve shows the raw output from COMSOL from 10 MHz to 10 GHz. The orange "Rational Fit Circuit" curve was generated by exporting of the S-Parameters to MATLAB and using the RF Toolbox rationalfit function. Then using the MATLAB generateSPICE function we exported a SPICE circuit fitting this. Note that the rational fit model smooths some features of the COMSOL simulation, shown by the deviations of the blue and orange curves around 3.5 GHz and the three blips from 7 - 9 GHz shown. These individual points are likely not physical and due to meshing defects in the model, and this fit corrects them as non-physical behavior. Notice also that that the system begins to plateau around 1 MHz due to the simulation stopping at 10 MHz and the nature of the rational fit. The 1 μF decoupling capacitor we incorporate in the model allows the circuit model to treat the infinite impedance at DC properly, and as long as this capacitance is much larger than the system under test, has virtually no effect on the results. This is because the impedance at the flat portion is already significantly higher than that of the rest of the circuit.

At frequencies below 700 MHz the model behaves almost as an ideal capacitor. Up to 2 GHz, an RLC circuit model approximates the curve extremely well, as shown with the overlaid model fit. This similarity opens up the possibility of "critically damping" our system, which we discuss later.

The circuit model of the port was imported into LTSpice, and the time-domain simulation shown in

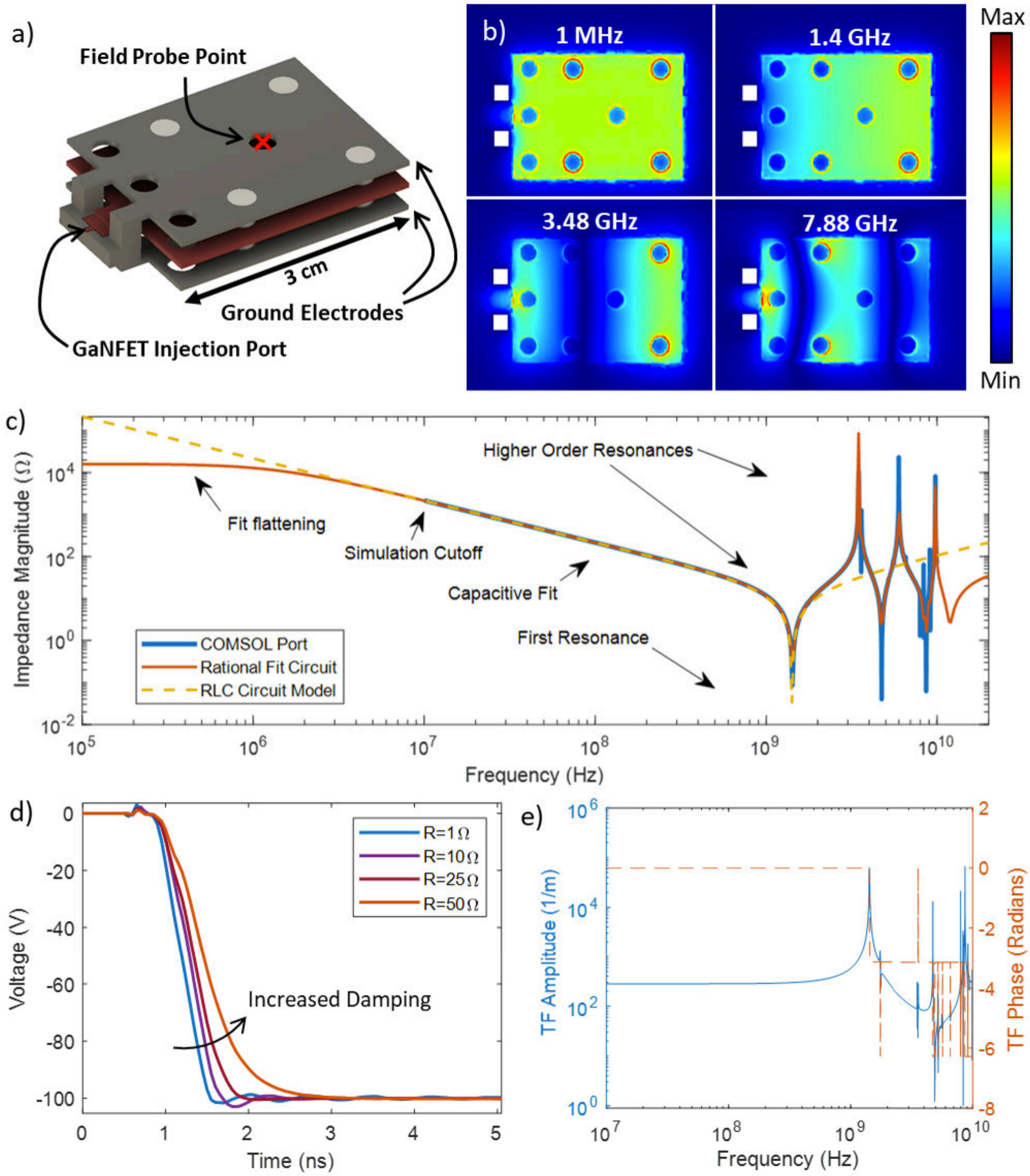

Figure 4.2: Simulated models of a parallel plate load. (a) The geometry of the load where the length of the plate is 3 cm, with the red x denoting the point at which we are probing the electric field. (b) The field structure of the load at various frequencies. At 10 MHz, the load all is driven in unison. (c) A comparison of the full impedance response from COMSOL to the circuit model fit. We also show a simplified RLC model for comparison. (d) The simulated port voltage extracted by interacting the mirror port impedance from 4.2c with the the circuit from Fig. 4.1d. (e) We can also extract the field to port voltage transfer function taken at the point shown in 4.2a. Note its flatness up to around 1 GHz, which is paralleled by the flatness of the field distribution shown in 4.2b up to 1.4 GHz.

Fig. 4.1 was used to simulate the voltage at the mirror input, which is seen in Fig. 4.2d. Then in MATLAB, we took the Fourier transform of this output voltages and multiplied it with the voltage-to-field transfer function (plotted in Fig. 4.2e) at the point indicated by the red x in Figure 4.2a to get the frequency response of the field in the load. The equation of this transfer function is shown in Eqn. 4.1, where E_x is the field at point $\vec{r_o}$ (the red x), V_{port} the port voltage in COMSOL, and ω the angular frequency of excitation. This math is shown in Fig. 4.3a-c. Finally, we took the inverse Fourier transform of the field response, resulting in the time-domain plot shown in Figure 4.3d. This shows significant ringing in the mirror, as would be expected for such an undamped model.

$$TF = \frac{E_x(\vec{r_o}, \omega)}{V_{port,\omega}} \tag{4.1}$$

We next worked to simplify the treatment of this load and remove ringing of the field at the point of interest. Generally, it is assumed that if an element is significantly smaller than the wavelength of the voltage or current exciting it, we can treat that element as a circuit node with parasitic quantities C and L associated with it [68]. Explicitly,

$$\lambda = v_{\text{eff}}/f >> \ell \tag{4.2}$$

where λ is the wavelength, v_{eff} the propagation velocity in the medium (in this case just c for vacuum), and f the frequency of interest. This approximation is generally held valid if the structure length-scale ℓ $\gtrapprox 10\lambda$.

We can see this lumped element behavior emerge explicitly in the impedance plotted in Figure 2c. At frequencies below 500 MHz, the parallel plates exhibit the characteristic of a 7.38 pF capacitor. As the frequency increases beyond 500 MHz and approaches the first resonance at 1.4 GHz, the load is no longer purely capacitive, but is well-modeled using an RLC resonant circuit with an inductance of 1.70 nH as shown in the Figure 2c. However, above 2 GHz, the system can no longer be treated as an 2nd-order LC lumped circuit due to the many resonant modes developed by the length scale of the load, some examples of which are shown in Figure 2b. This will be discussed in greater detail later.

Next, we swept through different damping resistances in our LTSpice model, and plotted the results in Fig. 4.4. Here, we can see a steady decrease of the load ringing as we increase the damping resistance from 1 Ω to 50 Ω. At a damping of 25 Ω we see the fastest ringing-free transition, which corresponds to a

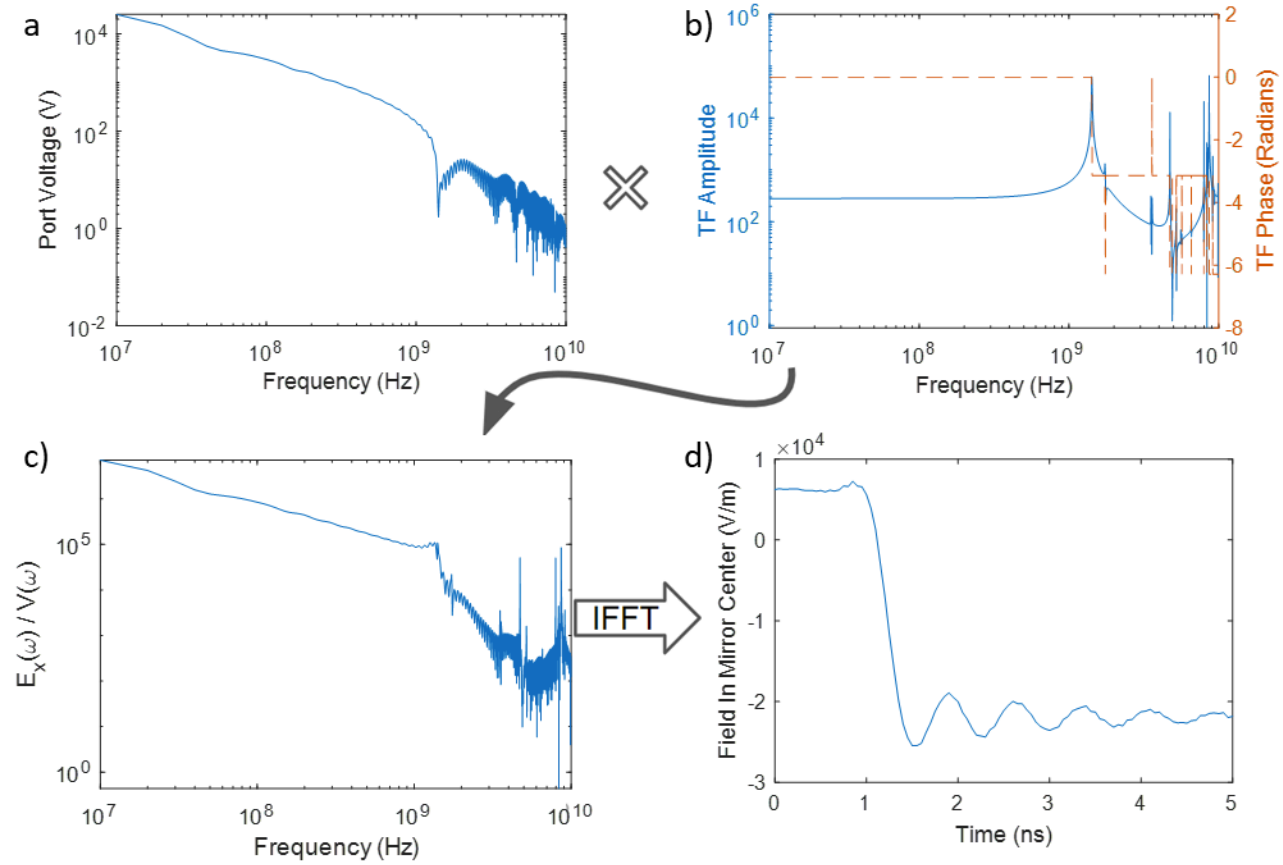

Figure 4.3: Fourier calculations of field ringing in the loads. In this example we show that multiplying (a) the frequency spectrum of the pulse by (b) the port voltage to field in mirror transfer function (the top right, taken at the red x in Figure 2a) results in the spectrum in (c). Note that (b) is basically flat until 500 MHz, then begins to rise until a peak at 1.44 GHz. This occurs because a quarter-wave mode that forms in the mirror with the minimum at the port, and maximum at the edge of the deflector as shown in Figure 2b at 1.44 GHz. This means that if we force a small set field (normalized to 1 V) at the input port near this resonance, a large field will result at the edge, and thus a large field at the sampling point as well. Depending on the position of the sampling point away from the port, the frequency at which this peaks changes. The closer the sampling is to the port, the higher this resonance. Taking the inverse Fourier transform results in the time domain response shown (d).

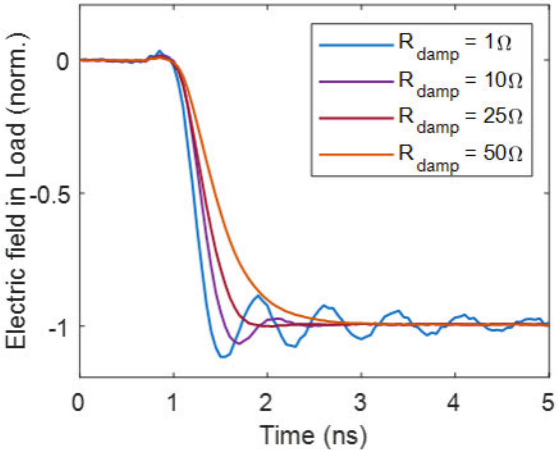

Figure 4.4: The electric field in the center of the gated mirror R_{damp}, which slows the response as it removes ringing. Note that higher-frequency ringing does still exist in the load fields due to the higher-order resonances, but they are less than 1% the transition magnitude.

200 V transition in less than 1 ns. The underlying switching performance and its dependence on R_{damp} is consistent with the measurement on a similarly resonant load load, the decoupled oscilloscope we drove in Chapter 3.

This RLC lumped element treatment offers significant advantage in the ability to estimate and remove ringing in our system. By treating the load as a lumped RLC model, it becomes significantly easier to understand the effects of the parasitic output capacitance and inductance of the driving FET. This treatment also allows "critical dampening" of the circuit with an appropriately selected series resistance, dramatically simplifying the filter design that would normally be needed for such a precise transition. This is demonstrated in Fig. 4.4, where a damping resistance is selected to cause a highly smooth transition that resembles a critical damping in RLC circuits. Ringing-like behavior at 4 GHz and above still does exist in the output, though it is significantly attenuated to below 1% the transition magnitude. This performance shows that these GaNFETs are capable of properly driving the gated electron mirror, as measured at a discrete point. In the following section, we will ensure that this switching properly transitions the full potential surface an electron will reflect off of, as well as discuss the ultimate limits to gated mirror switching.

4.2 Analysis of Mode Structure and Aberrations

In order for a gated mirror to properly reflect an electron, every point the electron wavefunction sees in the gated electron mirror must be approximately at the field distribution of the static gated mirror. If this is not the case, and the gated mirror fields change too much from pass to pass or depending on the electron timing,the electron will not stably recirculate as required for QEM. Thus it is critical to ensure we achieve a stable transition not just at the center point of the gated mirror discussed above, but at all other points.

Rather than represent all field points in the mirror, we choose several critical, high symmetry points on and around the optical axis to represent switching in different regions in space. These points are shown in Fig. 4.6a. Because the frequency of the excitation determines the wavelength of electromagnetic fields, and because this wavelength sets the length scale over which the fields are well-behaved, we can estimate the maximum frequency our point selection is valid to from the sampling spacing we choose. Given we plan to focus the electron beam onto the center of the gated mirror to minimize aberrations [34], the beam spot at the center will contain over 99% of the beam well within $1\,\mu\mathrm{m}$. With a convergence angle of 10 mRad, we would then expect an $50\,\mu\mathrm{m}$ spread of the beam 5 mm along the axis from the center point O, shown for the load in Fig. 4.5. In order to account for lens effects due to deceleration in the gated mirror, we expand this further to say that we expect the vast majority of the beam to be localized within $200\,\mu\mathrm{m}$ of the optical axis at all points. Given $200\,\mu\mathrm{m}$ wavelengths correspond to radiation in the terahertz, far above the frequencies we excite, we do not need any finer sampling of the fields.

We then use this electron length-scale estimate to space out our sampling points. Point L is chosen to be $200\,\mu\mathrm{m}$ along the propagating direction of the mirror, and point T $200\,\mu\mathrm{m}$ transverse to this. This is meant to capture the effects of time delay at point L and the development mode structure in both point directions over the much larger length scale of the gated mirror. We measure 10 mm backwards from the propagation axis to point S (not shown) to ensure we have the expected time delay of 100 ps between the points. We also sample at point G 5 mm along the optical axis from O to measure fields leaking from the gated mirror switching, and point M 2 mm along the optical axis from O to ensure no modes develop along the optical axis. Structure at M should never occur before structure at L or T, since this length scale is far smaller, but regardless we still check. Finally, at point N, $200\,\mu\mathrm{m}$ along the propagation axis from M, we measure to ensure consistent switching along the optical axis even away from the center.

All of these sampling points fields are plotted in Fig. 4.6. Their magnitudes vary significantly to point to point, reflecting the relative strength of the field in the DC case. Point O represents the field at the center of the gated electron mirror and is the same as that of Fig. 4.4 for $25\,\Omega$. It is shown again for reference. Near it are points T and L, which are similar, though of smaller magnitude. This is due to them being further from the optical axis. At points M and N we see a stronger field, since these are further from the center holes and thus fringing field effects are less significant.

The weakest field we see is at point G, which we expect due to the grounded exterior plates. A zoomed

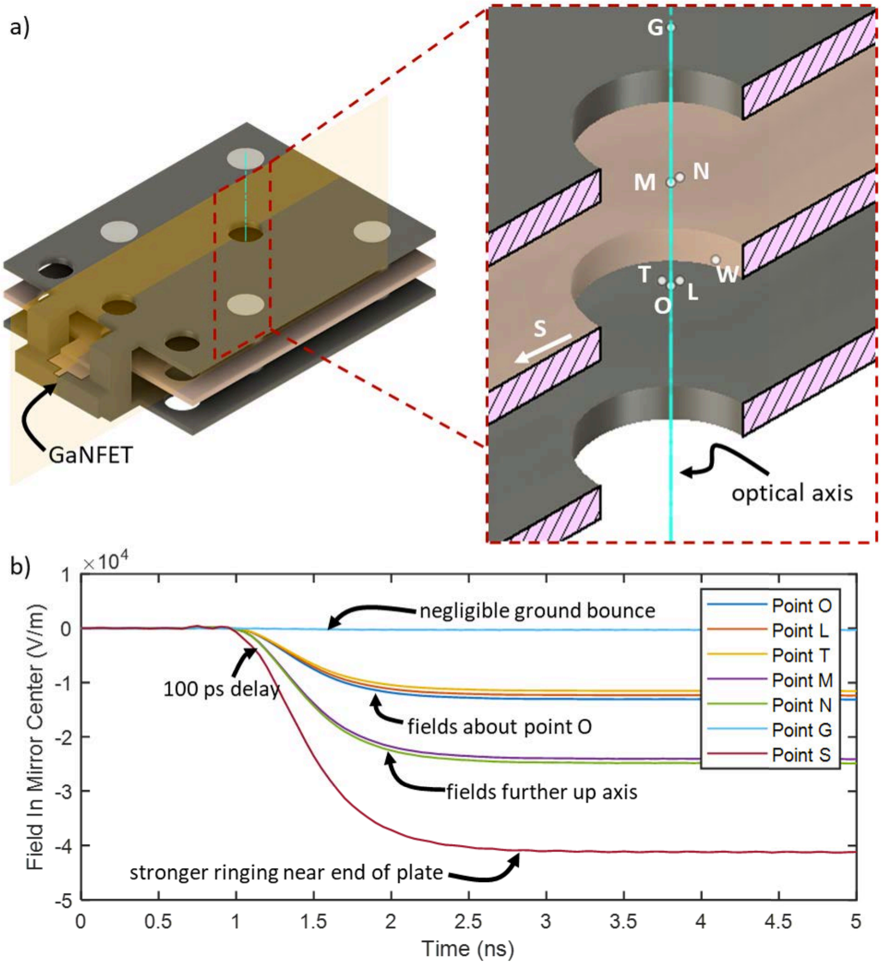

Figure 4.5: Various probe points and their fields, as described in the text. (a) The gated mirror load driven by a GaNFET, with a zoomed in cross section showing the sampling points. (b) The electric field in the optical axis direction as a function of time at various points.

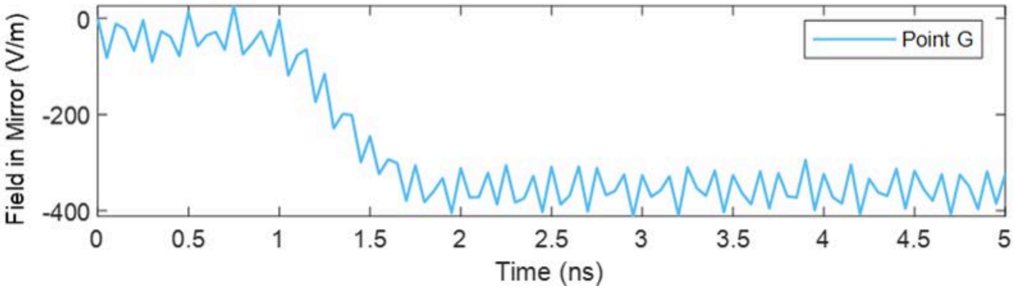

Figure 4.6: Ringing outside the gated mirror at point G. Fig. 4.5. This is zoomed in to see the ringing behavior persisting outside the mirror, though this is 1.5% the value of the gated mirror field transition.

in trace of it is The transition here is roughly 1.5% the value of the the center transition, quite small but not insignificant. This is residual field is equivalent to the concept of ground bounce in high speed circuits [67]. The strongest field exists at point S, far from the optical axis and directly between two plates. This would be expected as the other points are fringe fields near the holes of the electrodes and so substantially weaker. This point is shifted roughly 100 ps sooner than the other points, since the incident propagating fields from the GaNFET hit this region first.

Some other delays exist between these points, though for $200\,\mu\mathrm{m}$ separations this is on the order of 10 ps, so not visible for our purposes. Small variations also exist in the dominant ringing frequencies of each trace, which is set by the length scale of the full load. However, these are all within the bounds of our requirements for a gated electron mirror. Some deviations exist, from what would be expected for the pure DC simulation, such as point L and T not reaching the same final field value, even though they are symmetrically away from the optical axis. This is likely due the need for even finer meshing in our simulation; future work will address this and other discrepancies.

4.2.1 Maximum Switching Speeds and Voltages

We now determine how fast we could possibly switch the gated mirror, given the length scale of the load, and to what voltage. The maximum voltage is set by the pulser technology used. By varying the FET material and topology, this approach can be extended to switching even higher voltages and currents. The simplest way of doing this is to vary the GaNFET technology, using for example the GS61004B from GaN Systems or the TP65H070LSG from Transphorm, both of which are capable of 650 V operation, though their increased gate capacitance, output capacitance, and parasitic inductance lead to slowed output transitions. Another approach would be to use SiC technology, allowing for transitions of several thousand volts though at the cost of even slower transitions. Alternate topologies used to improve silicon performance, such as parallel or stacked FETs [44] or cascode configurations [46] could also be used to improve both voltage ratings and transition performance.

Several routes also could be used to increase the speed of these switches to achieve sub-nanosecond transitions, though at the trade-off of lower voltage. Smaller, lower voltage FETs such as the 100 V EPC2037 from the Efficient Power Corporation would have significantly faster switching due to its smaller gate and output capacitance, as well as its lower form factor. For low voltages and medium currents of 5 A, GaNFET gate drivers such as the LMG1020 itself could also be used directly to drive loads with 400 ps transition times. If state-of-the-art rise times are desired, non-linear pulse sharpening techniques such as step recovery diodes [69] and nanoplasmas [58] could be used together with these FETs, which would allow for transitions on the order 100 ps or less, and would not increase layout size significantly.

A natural question that arises as we increase the speed of the transitions is how fast the loads fundamentally can be driven, especially when trying to ensure no ringing. Even if we drove the load with an ideal 100 ps step, the high-frequency resonances of the load would drown out the signal in ringing and drag out the transition. This is demonstrated in Fig. 4.7 for the real load in Fig. 4.2a. If we then put this transition through an ideal Gaussian filter to reduce the pulse bandwidth and reduce the ringing to 1% the transition, we get the result in Fig. 4.7b which is significantly slower, taking roughly 1.7 ns to get within 1% accuracy. This transition is significantly slower than the RLC response also shown in Fig. 4.4, which takes 1.2 ns to achieve similar accuracy.

As mentioned in Chapter 2, we could also drive the gated mirror with a an arbitrary waveform generator (AWG) and amplifier. If we assume the AWG and amplifier have unlimited bandwidth and gain, and that we can perfectly simulate or measure the response of the gated mirror, we would then theoretically generate any driving signal with any spectrum we would like. Then, we could selectively remove the resonances of the load (seen in Fig. 4.2c) that leads to ringing shown in Fig. 4.7a to produce a transition at a point of any speed we would like. In practice, this is limited by several factors. The first is in the realization of the high power signal - state-of-the-art high voltages amplifiers only have bandwidths of 1 GHz at the best. Second, it is difficult to know what exactly to compensate the signal to. This is because simulating to the required accuracy is extremely difficult due variations from fabrication error, changes in cabling, and effects in real loads such as surface roughness. Measuring these resonances directly is also impossible with traditional probing, which loads the gated mirror and modifies its behavior too substantially. Theoretically one could use an electron as a probe to view these fields directly and then compensate, but this has yet to be achieved in the literature, and is the topic of Chapter 5.

Assuming all of these challenges can be overcome, we still run into bandwidth limits to the mirror

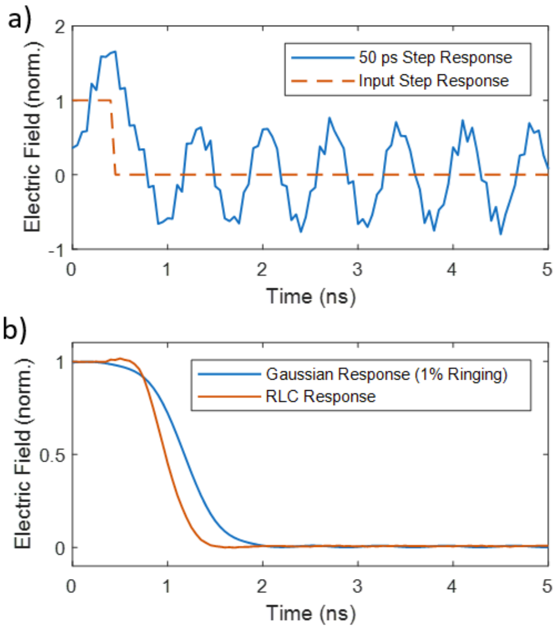

Figure 4.7: Results of injecting arbitrary signals into the load of Fig. 4.2a. (a) The response of the load to a instant 50 ps step (orange dotted line), showing ringing at not just the lowest resonant frequency, but also at the higher order frequencies which appears a roughness on the trace. (b) The same response, but with the edge slowed by Gaussian filtering to reduce the ringing to 1% the transition magnitude. The orange curve is taken from 4.4d for comparison, showing an even faster RLC-based response.

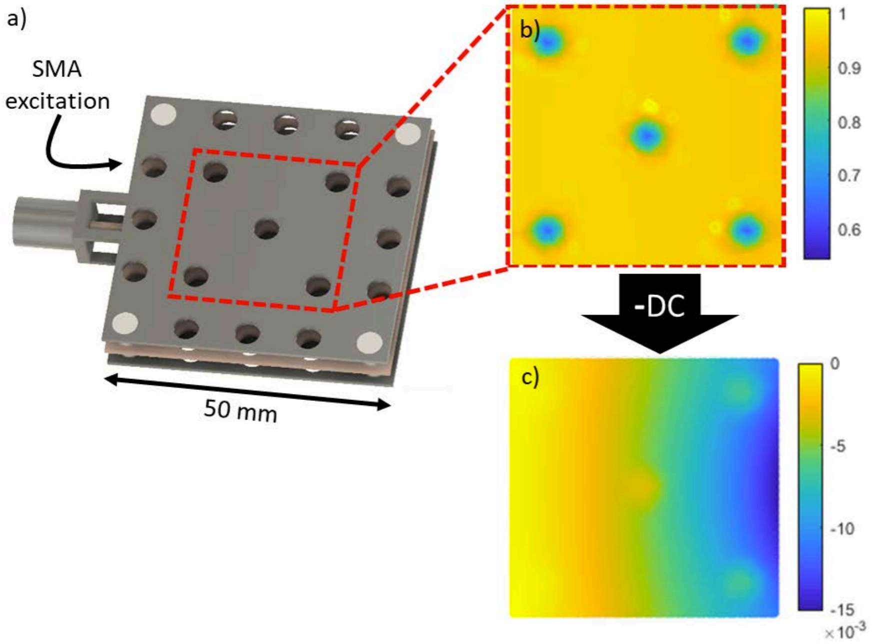

Figure 4.8: New gated mirror simulation based on an SMA driven from perfectly matched 50 Ω source. (a) The CAD model used. (b) The field distribution at 250 MHz. (c) The difference between the field distribution at 250 MHz and DC, highlighting the weak dipole moment already developing.

set by the length-scale of the load and driving circuitry. We demonstrate this in a new simulation by in-coupling an SMA connector to a larger gated mirror structure, shown in Fig. 4.8a. We choose this larger gated mirror to force the resonances to be at lower frequencies, and because this was the structure used in our initial experiments. This is demonstrated in Fig. 4.8b, where we zoom in to the center inset box shown in red to visualize the field distribution better. This plot is normalized to the maximum field strength between two of the plats. At first glance, this distribution looks quite homogeneous, as would be expected for low frequency driving, in which the quasi-static approximation holds. However if we then subtract out the DC field contribution terms, as shown in Fig. 4.8c, we can see the beginnings of a mode developing along the propagation axis. while, this is still small, with the peak deviation being only 1% the maximum field strength in the mirror, it is important to consider for our high accuracy application.

At high enough frequencies, these field modes strengthen and begin to substantially develop across the length of the structure. breaking the axisymmetric structure of the mirror surface required for clean electron reflection in the resonator. At 1 GHz, a dipole-like moment begins to develop along the propagation axis, which then becomes stronger and stronger until the null at 3.3 GHz (Fig. 4.9b). As we increase frequency, it continues to shift towards the source, then at 6.55 GHz forms another almost circularly symmetric mode (Fig. 4.9c). At 7.8 GHz it eventually forms a quadruple-like mode as shown in Fig. 4.9d. Note that at all frequencies shown, the distributions are transverse electromagnetic modes (with the primary field in the optical axis direction) since the spacing of the plates is much smaller (2 mm) than their length and width (20 mm).

These modes are impossible to correct for to create a homogeneous mirror field as in the pure static field case. This is due to the different oscillation frequencies of each mode leading to it being impossible to coherently “add” these modes to construct a potential of the static shape. Thus, even with the best possible AWG and perfect knowledge of the mirror response, it is impossible to use a predistortion approach a to correct for a field beyond a highly localized region set by the wavelength. This is analogous (though at significantly higher frequencies) to the more common problem of active electromagnetic interference cancellation systems, in which even with the best probe and Helmholtz coil, it is impossible to correct for fields at more than just the probe point [70]. This problem sets a clear upper bound on the possible switching speed.

Because the propagation axis is the longest length scale in the gated mirror, this direction sets the lowest bound on our frequency. This is because this direction forms the lowest frequency field structure. In order to visualize this dipole more clearly, in Fig. 4.10 we plot the log of the field intensity along the propagation axis (shown by the dotted lines in Fig. 4.9) versus frequency. This is normalized so that the

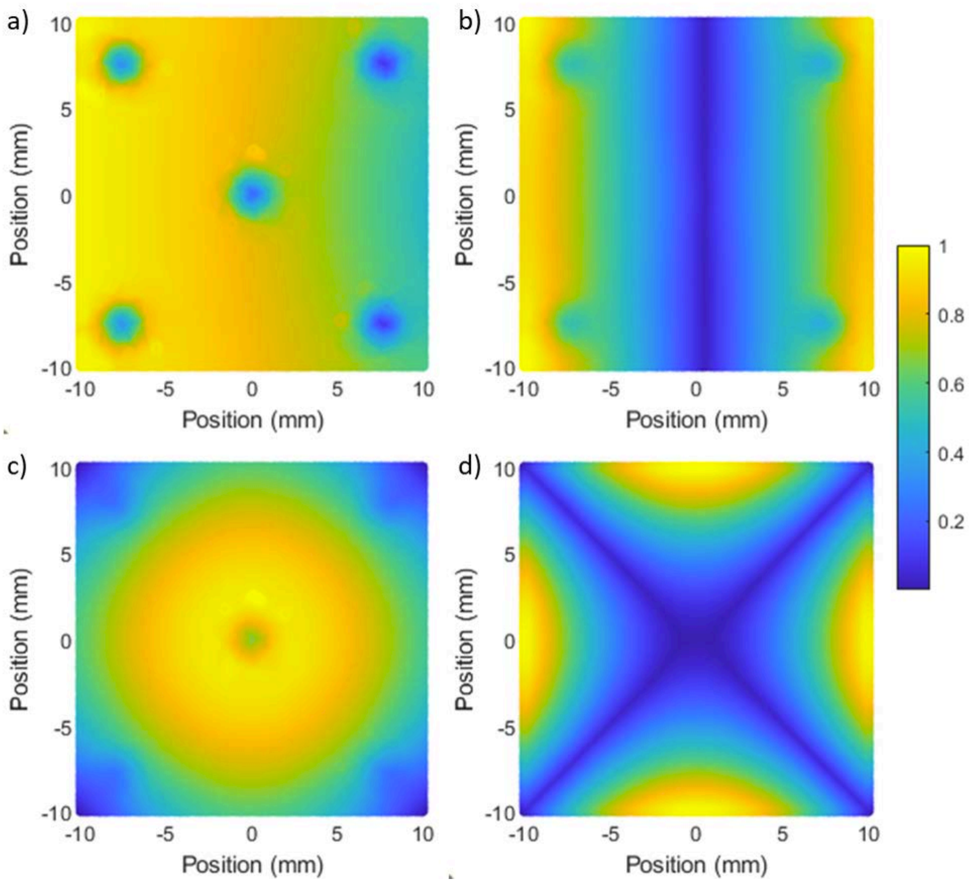

Figure 4.9: Electromagnetic modes developed over the gated electron mirror structure. (a) 1 GHz. (b) 3.3 GHz. (c) 6.55 GHz. (d) 7.8 GHz

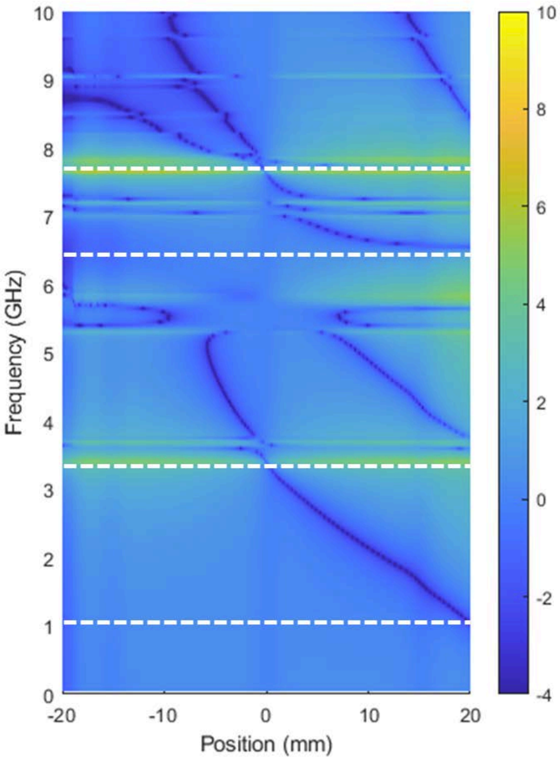

Figure 4.10: Normalized mode development in the gated mirror versus frequency. At low frequencies, the structure is quite homogeneous, as the entire mirror switches far slower than the propagation speed across the structure.

field strength at the input port is constant. We can clearly see the dipole mode structure develop as the frequency is increased, with the null crossover point (blue) slowly shifting to the source from the left. At 3.3 GHz we see that the crossover passes through zero, consistent with Fig. 4.9b. Above this at higher frequencies we see more and more complicated structures develop, since far more than just this dipole moment appears above 3.3 GHz.

From these plots, we can estimate the fastest possible switching we could hope to achieve, even with the best possible AWG. We do this by generating the fastest transition we can at point O that still keeps point L, 200 μm away, switching in unison with point O to the error bounds we select. In order to estimate this, we first normalize all the field distributions to the same weight, and take field samples both at point O and point L. Taking the difference of these gives us the mode-structure-limited deviation from an ideal DC potential as a function of frequency. This leads to an estimate that it is possible to drive the gated mirror to 1% accuracy in less than 100 ps. However, due to the inaccuracies in our simulation seen in the symmetry discrepancies of Fig. 4.5, this needs further examination.

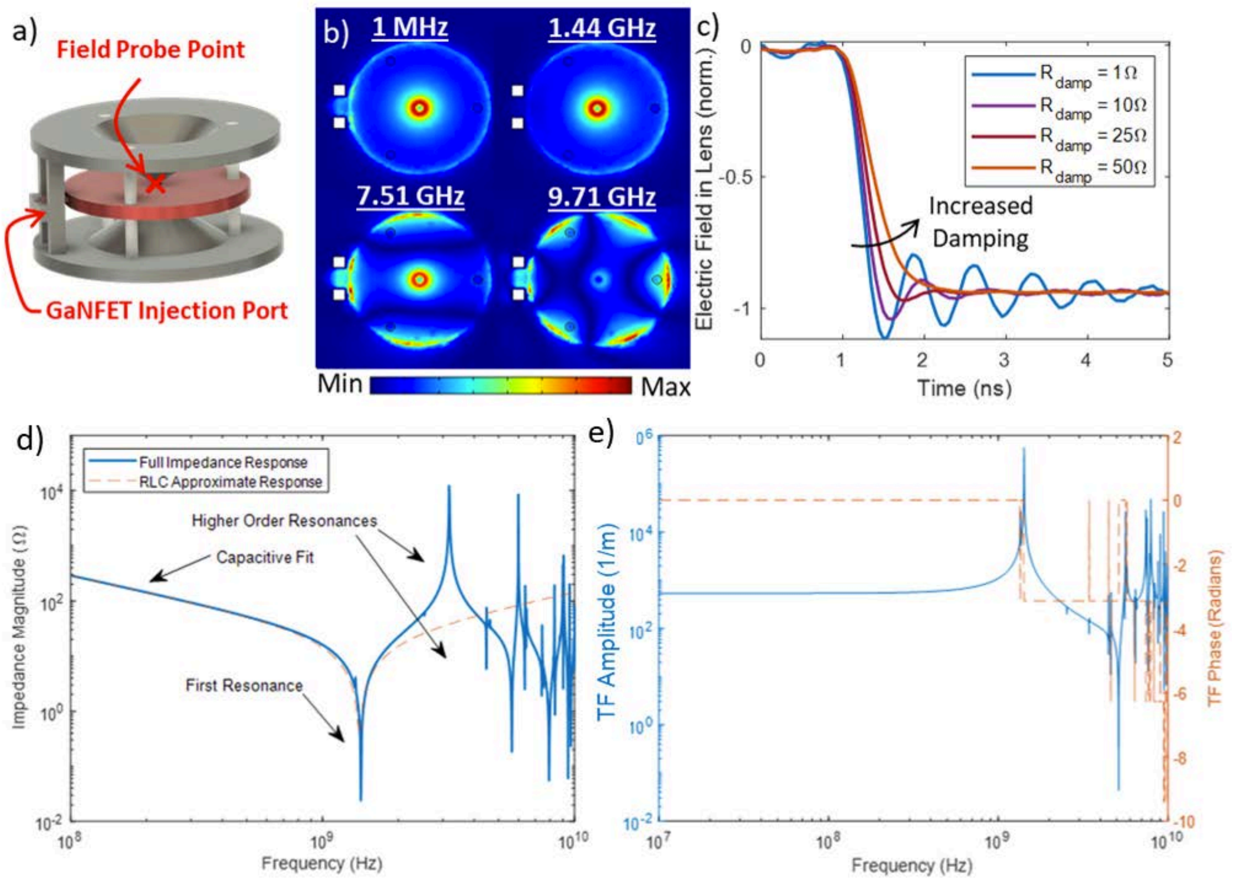

Figure 4.11: Einzel lens simulation. (a) A high voltage electron lens structure, with the red x showing the field sampling point near the center of the mirror. (b) The response of the lens at various frequencies, with resonances fitting the geometry of the structure. (c) The response with increased damping. (d) The port impedance of the Einzel lens, with the fit to a series capacitive-inductive load. (e) The transfer function relating the field in center of the lens to the voltage at the input port.

4.3 Analysis of Other Loads

We also examined other loads to validate the generality of this approach and look into other applications of our pulser. In Fig. 4.11a-c we show driving of a high voltage Einzel lens. This kind of structure is used commonly in electron optics, where the varied spacing of plates is designed to allow for high-strength fields near the center, while the wider spaced portion near the edges prevent electrical breakdown at the insulators during high voltage operation [71].

This load has varied capacitance from the outside of the structure to the inside, as well as a much more significant inductive component due to the large ground return loop. Various resonances of this structure are shown in Figure 3b, and we can clearly see stronger electric fields near the center due to the closer plate spacing. Unlike the first capacitor model, this load cannot be easily simplified into a transmission line segment and thus matched to $50\ \Omega$ systems. However, the load can still be simplified into 5.50 pF capacitive model at low frequencies and a series RLC circuit with 2.35 nH inductance at higher frequencies, extracted from 4.11d. This higher inductance and lower capacitance is consistent with the larger ground return path of this structure compared to the primarily capacitive load. As before, using GaNFET driving and dampening of the first RLC resonance, it was possible to generate 1.2 ns ringing-free field transitions in the load at the field probe point. The generated field strength is equivalent to that that would be generated from a 200 V potential applied to the center electrode. It is interesting to note that nominally the first resonance of this lens and the deflector are the same, but the under-damped deflector response has less ringing. This is due to the output capacitance of the GaNFET circuit element, which results in a response that is much more sensitive to the inductance of the load.

Another load we drove is the inductive coil shown in Fig. 4.12a, which primarily generates a magnetic field rather than an electric field and is used commonly for applying strong magnetic fields to samples and for electron beam deflection systems [71]. The driving topology for this circuit is different from that of the previous cases due to the low DC impedance of the load. The circuit used is shown in Figure 4.13. The damping approach for the simulated inductive load is not very practical due to its large power consumption. Alternative damping techniques such as the use of a series resistor and capacitor in parallel would probably be more feasible, though was not explored.

At low frequencies, this element behaves as a near perfect 313 nH inductor, with an impedance that increases linearly as a function of frequency as shown in Fig. 4.12d. As the frequency increases, the capacitance between the wires begin to shunt current, resulting in a reduced impedance and more concentrated fields near the edges as shown in Fig. 4.12. When the first resonance is reached around 260 MHz, we can model the circuit as a parallel RLC circuit with a capacitance of 1.15 pF. Similar to the previously discussed loads, we were able to tune R_{coil} to achieve a ringing-free magnetic field response driven by a $20\ \mathrm{A}$ current as shown in Fig. 4.12c. However, due to the large inductive component coupled to the GaNFET's output capacitance, this load requires a very large resistance of 110 Ω to damp, slowing the response substantially. Although the current transition time of roughly $20\ \mathrm{ns}$ can be shortened by reducing the loop size or number, inductive loads will almost always be slower that capacitive loads due to the large fixed output capacitance of the GaNFET and circuit board, which the COMSOL simulation does not include, but the LTSpice simulation does. Note that in this case, the transfer function is defined as the ratio of the center magnetic field (A/m) to the port current (A), resulting in the same units of (1/m) for the transfer function.

Order-of magnitude estimates can be made for all of the given loads without the need for full simulations. In our case, this was used to validate the behavior of our models up to the first resonance. For

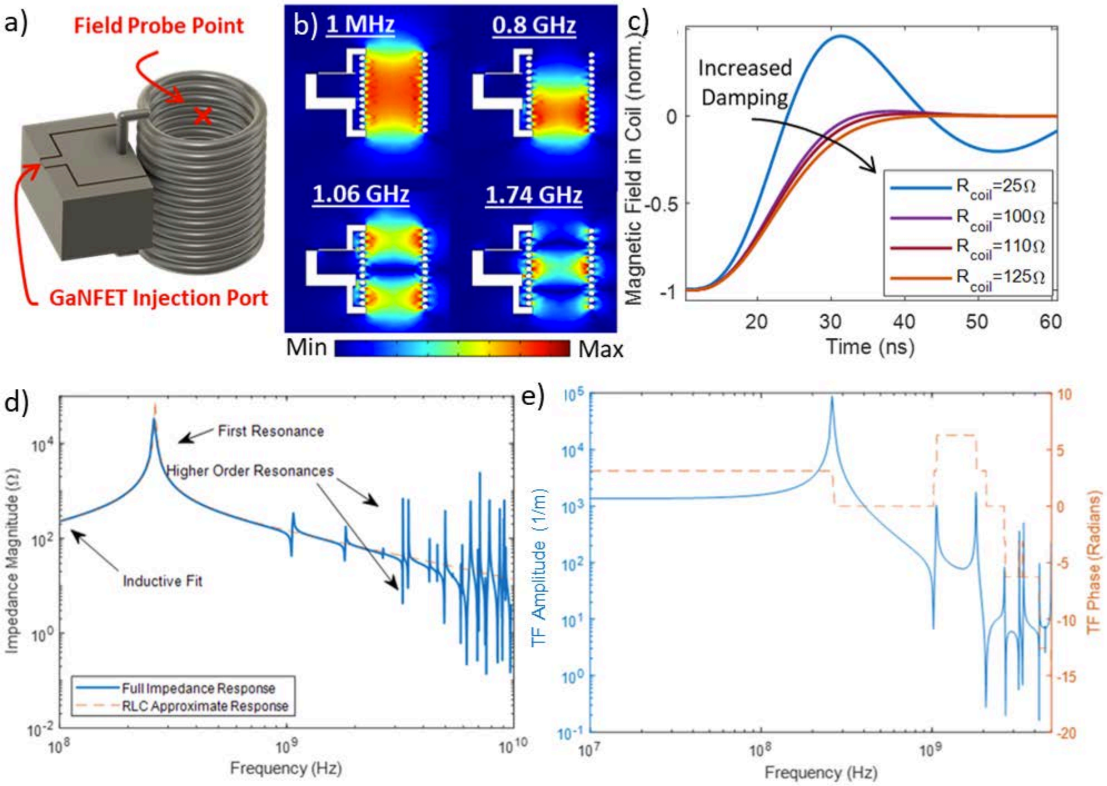

Figure 4.12: Inductive Load. (a) An inductive load with the vertical magnetic field sampled in the center of the structure. (b) The magnetic field distribution, which is complicated even at low frequencies, and concentrates the field via capacitive coupling near the edge of the coils at higher frequencies. (c) The result of damping the inductance, with a huge ringing period due to the large DC inductance of the structure. (d) The port impedance of the inductive coil load. The resonance is much lower than in the other cases due to the large inductance of the coil. (r) The transfer function of the magnetic field in the center of the coil to the current input into the load.

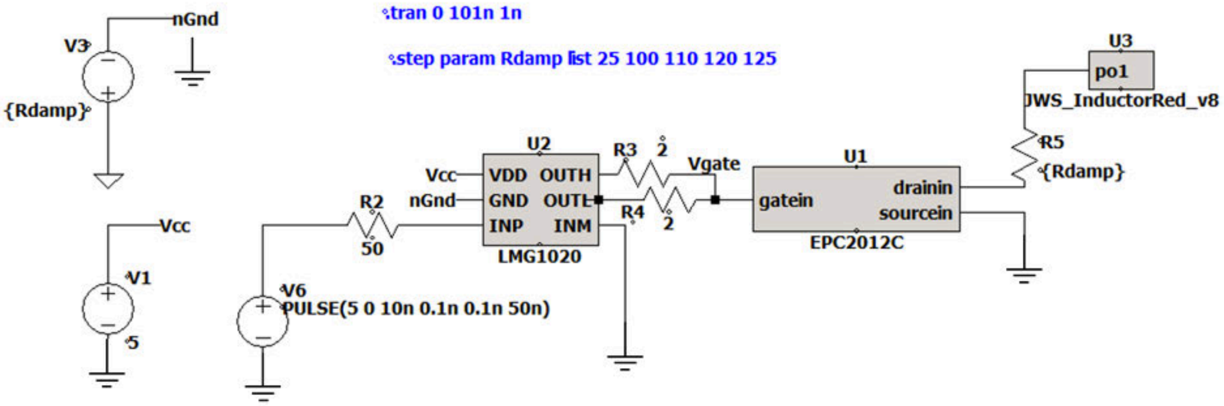

Figure 4.13: Simulated inductor topology. Notice the replaced ground symbol attached to nGnd. This was used because the circuit model of the inductor was internally referenced to ground, so in order to drive the inductor as if it was attached to a voltage source to the drain, we had to drop the potential of the rest of the circuit to this so-called ”new” ground.

inductive loads, we can estimate the load inductance using equation 4.3, where A is the loop area, μ the core permeability, N the number of loops, and ℓ the length of the coil. The output capacitance of the GaNFET will almost always dominate the capacitive portion of the response, and so the resonator can be treated as a combination of the GaNFET output directly to an ideal inductor.

$$L_{\text{coil}} = \frac{\mu N^2 A}{\ell}. \tag{4.3}$$

For capacitors, we can roughly estimate the capacitance of the structure with a parallel plate approximation using equation 4.4, where ϵ is the permittivity of the medium, ℓ the length of the plates, w the width, and d the separation. If the spacing varies over the structure, a very rough estimate of the capacitance can be made by using the ”average” spacing of the plates over the full structure. The inductance can be over-estimated by forming a loop from the GaNFET to the end of the structure at the ”average” spacing, and using equation 4.5 below, where μ is the permeability of the medium and the other quantities the same as for 4.4.

$$C_{\text{plates}} = \frac{\epsilon w \ell}{d}, \tag{4.4}$$

$$L_{\text{plates}} = \frac{\mu d \ell}{w}. \tag{4.5}$$

Using these lumped element quantities, we can estimate the “critical” damping (R_{damp}) needed of any structure using equation 4.6. This takes into account the total capacitance (C_{total}), inductance (L_{total}), and resistance (R_{internal})) of the system which are the combination of the load capacitances and inductances and the GaNFET capacitance and channel resistance. Better estimates of the inductive and capacitive quantities can be found from [67] to improve this estimation. Doubling the damping used with rough estimations of these quantities ensured over-damped results.

$$R_{\text{damp}} = R_{\text{internal}} + \sqrt{\frac{4L_{\text{total}}}{C_{\text{total}}}}. \tag{4.6}$$

If we would like to go further than damping the port quantities and ensure there is very little ringing on the final port, we would have to estimate the frequency spectrum of the pulse, as well as the locations of these resonances in the load in the frequency domain. A common rule of thumb for the -3 dB bandwidth is shown in equation 4.7, where f_{-3dB} is the -3dB bandwidth and r_t the 10% to 90% rise time.

$$f_{-3dB} \approx \frac{0.35}{r_t}. \tag{4.7}$$

A more exact solution would be to take the pulse edge generated by critical damping and take the fast Fourier transform of it. We then can find the frequency corresponding to whatever accuracy we would like to achieve in our system, in our case, this was assumed to be 1%. The closest analog to this problem can be thought of as the classic problem of a potential across a parallel plate transmission line, in which both ends of the line remain open until one side is suddenly shorted by the damping resistance we set.

We now will estimate the transfer function resonances for the capacitive case. We do this by taking the distance from the GaNFET to the point of interest in our system, weighted by the average velocity of propagation in the system. In the simplified case of dielectrics ($\mu_r = 1$), we first calculate an effective dielectric constant of the system. This is shown in equation 4.8, where ℓ_i is the length of each segment, ℓ_{tot} the total length to the point of interest, and ϵ_i the permittivity of each segment. Next, we use this effective impedance to derive the position of the first resonance, assuming that this is a quarter-wave resonance (caused by the low impedance at the input port set by the damping resistance and high impedance at the sampling point). This is shown in equation 4.8.

$$\epsilon_{\text{eff}} \approx \frac{\ell_1}{\ell_{\text{tot}}}\epsilon_1 + \frac{\ell_2}{\ell_{\text{tot}}}\epsilon_2 + \ldots \tag{4.8}$$

$$f_{\text{res}} \approx \frac{4c}{\ell_{\text{tot}}\sqrt{\epsilon_{\text{eff}}}}. \tag{4.9}$$

If the location of this resonance is above the pulse edge band-width derived above, ringing due to the geometric resonances will most likely be negligible unless the quality factor of the resonances is extremely high. Due to the strong cutoff of our pulse edge, higher resonances (which are generally over lower strength than the first resonance) will almost always be even less excited.

From these simulations, we demonstrated that the GaNFET circuitry constructed is capable of switching the gated mirror as fast as we require. They also gave insight into the ultimate switching speeds of the mirror, and the potential of these circuits for driving other load geometries, taking advantage of the lumped element approximation. Minor errors in our simulations became apparent when testing the ultimate switching speeds of the mirror, especially close to the optical axis at distances the electron would see. Future work will seek to correct these errors by using finer meshing on the optical axis, reflecting the length scale of the electron wave packet. Eventually, we aim to simulate a gated mirror including dielectric loss and surface roughness effects, and to fully quantum-mechanically predict the interaction of the electron with a switching gated mirror.

Chapter 5

Testing of the Gated Electron Mirror

In this brief section, we take the first steps in validating the performance of the gated electron mirror. First, we extract observable parameters from our model, which will be used to ensure proper switching of the mirror and discuss best strategies for observing them. We then construct an optimized gated mirror. Next, we discuss our designs for an electron streak camera capable of observing the fast electrical fields in a non-optimized mirror. Finally, we demonstrate early results for this gated mirror, directly observing resonances up to 3.3 GHz and extracting the transfer function of the system over multiple points in space.

5.1 Calculation of Observable Outputs

In order to verify that we have stably switched the gated mirror with no ringing, we need some kind of measurement. As mentioned previously, electrons do not simply interact with gated mirror fields at a single point. Instead, they follow paths in which the electron wavefunction interacts with the mirror field at every point in space. To solve this time-dependent interaction fully quantum mechanically is a computationally intensive problem beyond the capabilities of our current simulations.

Fortunately, there are approaches we can take to simplify this problem substantially and generate observable outputs from our simulations. Knowing that an electron has an extremely small wavelength, and thus can be well localized to sub-micron scales far below the mode structure of our switching, we can simplify this full quantum calculation into a classical path integral. The two simplest kinds of paths we are interested in are shown in Fig. 5.1.

The first type of path is the gated electron mirror mode, shown in Fig. 5.1a. In this operating mode, the electron, shown traveling on the x-axis, is slowed down substantially by the mirror before either just transmitting or stopping and being reflected. If the electron is at all off the optical axis, it will also pick up

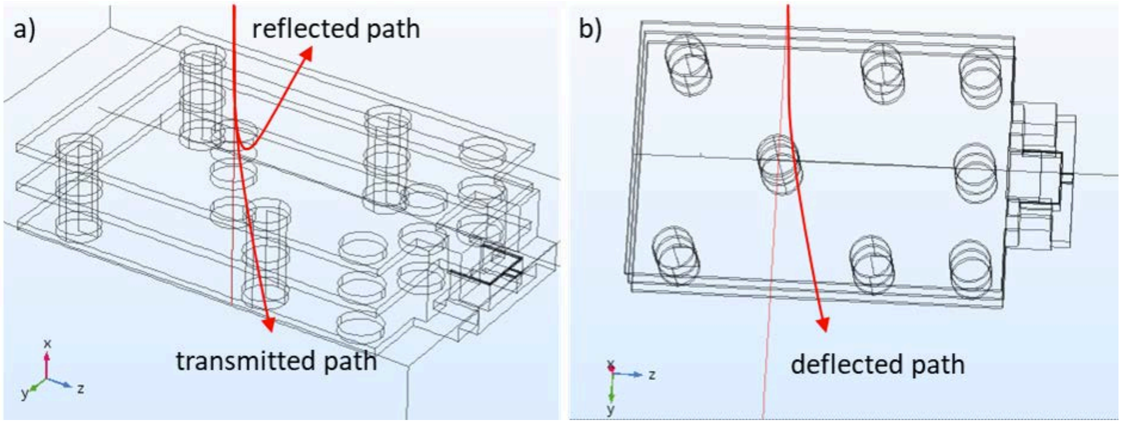

Figure 5.1: Electron paths in the gated mirror. (a) The path when the gated mirror is used as a mirror. (b) The path when we instead use the gated mirror as a deflector

a transverse velocity as shown. Solving for this path integral is difficult, as the velocity of the electron and the electrical field change in the integration direction.

If we instead insert the electrons from the side, as shown in Fig. 5.1b, the integral is much easier to solve. If we assume the electron momentum from the gun is much greater than the momentum kick p_x it receives from the mirror, we can approximate the electron path as a line in the y-direction. In the limit of the electron passing though the structure much faster than the the field is oscillating, we can approximate this deflection ϵ as Eqn. 5.1 below, where e is the electron charge, $E_x(y)$ the x-directed electric field distribution along y we simulated, and v_y the velocity of the electron. However, given that at 3 keV (10% the speed of light) we know that the electron interacts with the 3 cm long mirror path for 1 ns, meaning that to test GHz signals, we need to include the full time-domain part of the calculation.

$$\epsilon \approx \frac{e}{m_e} \int_{-\infty}^{\infty} \frac{E_x(y)}{v_y^2} dy. \tag{5.1}$$

The deflected magnitude of Fig. 5.1b is much greater than that of Fig. 5.1a, since the majority of the electric field is in the x direction. Thus, in later sections, we will use this direction to verify the field distributions in our gated mirror.

5.2 Construction of a Gated Mirror

As we learned from Chapter 4, improving the performance of the gated mirror primarily comes down to reducing its length scale. This improvement stems from two factors - reduced parasitics in the load

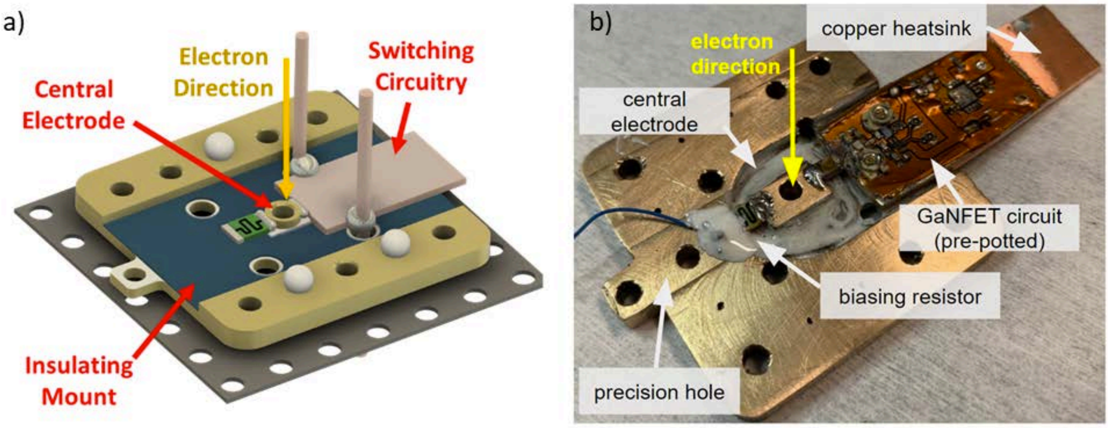

Figure 5.2: Optimized gated electron mirror. (a) A CAD rendering showing the design clearly. (b) The fabricated mirror, made for electrical testing, but not of electron-optical machining quality.

which reduces the circuit resonance we need to damp, and fewer asymmetric spatial modes over the length scale of the load which distort the beam. The challenge to constructing an optimized gated mirror then comes figuring out how to balance reduced length scales and dielectric use with precision fabrication, high-voltage rating, and insulator charging requirements.

An early prototype is shown in Fig. 5.2a. In this design, the first resonance was shifted from 1.4 GHz from the design of earlier simulations to 2.3 GHz in this structure. Beyond just shrinking the central electrode, several design elements come into play in it. First, the central electrode is well isolated by a biasing resistor placed directly next to it. This high impedance element acts to allow the circuit to be held to high voltages, but stops the length scale of the mirror from increasing and the biasing supply from causing the mirror to recharge while holding at the reflective state. Second, we have the center electrode peaking out from above and below the insulators holding it in place. This prevents the electron from seeing any insulator, which distorts the beam on line of sight due to stray charge accumulating and being unable to dissipate on them. Third, the lens element is made of silicon bronze, a hard metal that does not form an oxide or deform, and is also non-magnetic, so does not require annealing after machining, which would destroy our structure. Last, we ensure there is a good ground return path by directly linking the copper circuit board to the outer ground plates as close as possible, to minimize path inductance.

The fabrication approach is shown in Fig. 5.3. The key step is shown in Fig. 5.3e, where the center electrode is held in place by ball bearings while the epoxy hardens. This fabricated mirror is shown in Fig. 5.2b with minor modifications. It has yet to be tested using electrons, since the streak camera design would have to be pushed to even higher frequencies.

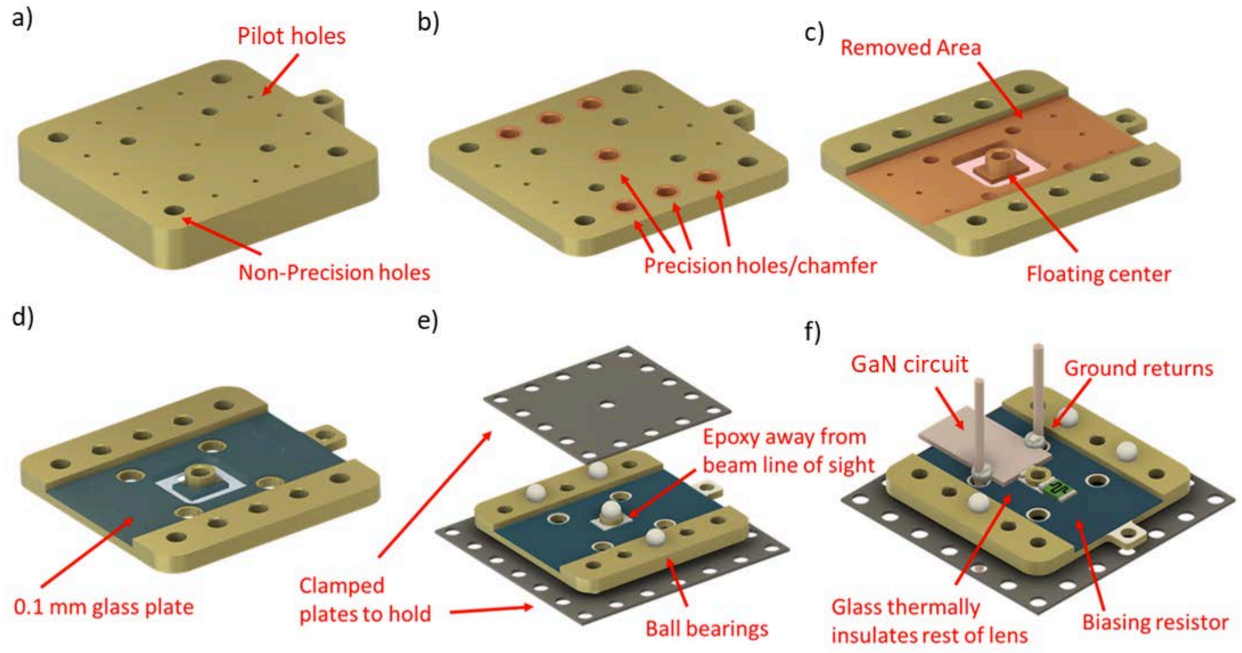

Figure 5.3: Optimized gated electron mirror fabrication. (a) First, we use a water jet cutter to cut out the stock and drill pilot and fixture holes. (b) Next, we use precision bits to drill out and chamfer critical holes for the ball bearings and center electrode. (c) Using a mill, we then separate out the center electrode from the stock, and mill a recess, not machining the center hole or ball bearing holes. (d) After this we place a thin Pyrex glass sheet onto the mirror recess, which was also water jet cut. (e) We next place the center electrode into the middle, held onto the glass plate gently by the wet epoxy. We then place the ball bearings onto their holes, and clamp the mirror between two plates. This holds the center electrode in place while it dries. (f) Finally, we attach the GaNFET circuit and solder on the grounf returns and biasing resistor. The whole part is sonicated in acetone and IPA for 15 minutes each.

5.3 Designs for a Streak Camera

In order to verify that our circuit functions as intended, and we indeed achieve nanosecond, ringing-free transitions of the gated mirror electrode, we need testing. Unfortunately, no commercial electrical probe exists for measuring fields so high frequency, high voltage, and sensitive to perturbation. Due to the enormous complexity of a QEM, it is also not advisable just to plug this system in and hope that it works based on simulation.

Due to these challenges, we decided the best route would be to develop a streak camera to measure these fields both spatially and temporally using the smallest probe possible: an electron. This apparatus, whose overall design and operation principle is shown in Fig. 5.4, has been used historically for oscilloscopes and for picosecond-resolution measurements in optics [72, 73].

The streak camera implementation inside of a Zeiss LEO 1550 scanning electron microscope (SEM) is shown in Fig. 5.5. At the top is the electron column, capable of operating from 500 V to 20 keV. Directly

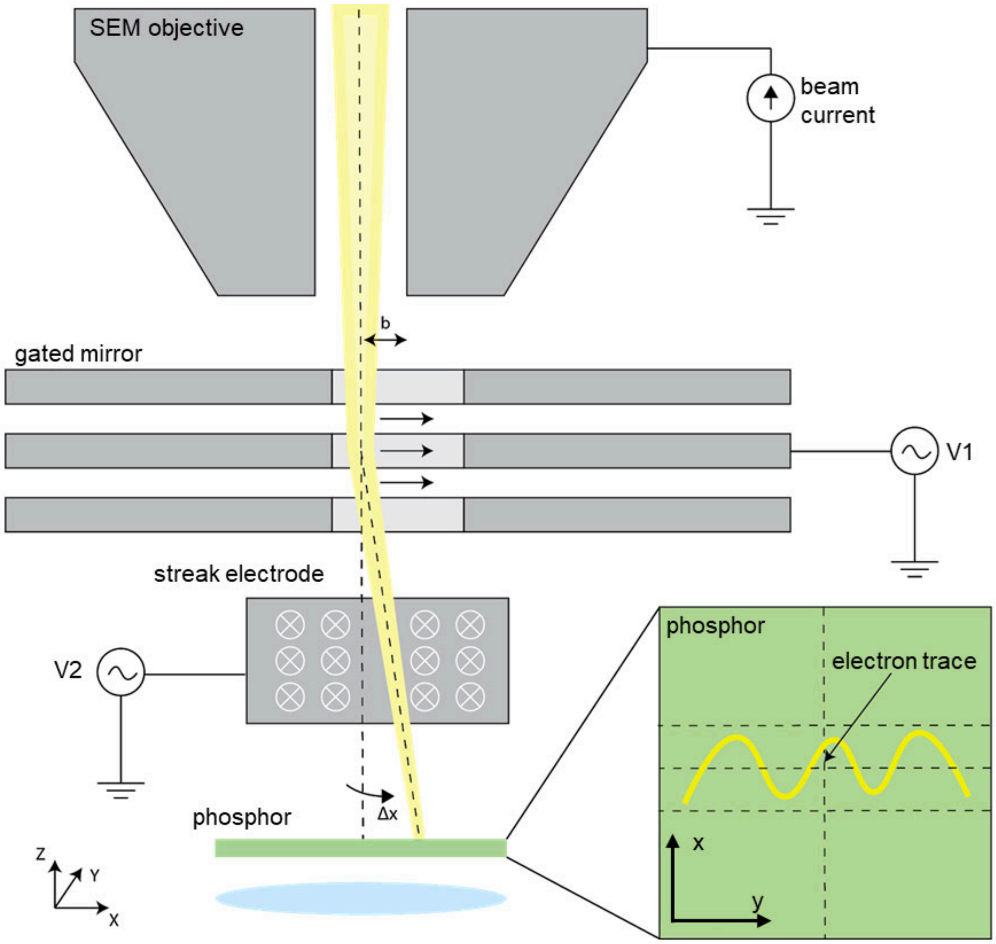

Figure 5.4: Overview of the operation of the a streak camera we designed and constructed. First, an electron probe is focused inside a region of interest in the gated mirror. When signal V1 is applied, this causes a slight deflection in the beam in the x direction. Next, the probe passes a larger plate. This plate is excited with a second slower, higher amplitude signal V2, which is either phase-locked with V1 if measuring in the frequency domain or synchronized if in the time domain. The beam is then incident on an imager, consisting of a acceleration grid, micro-channel plate, and phosphor. As shown, this results in the trace seen in the bottom left inset. The signal generated on the phosphor is then imaged out of the vacuum system and onto a camera.

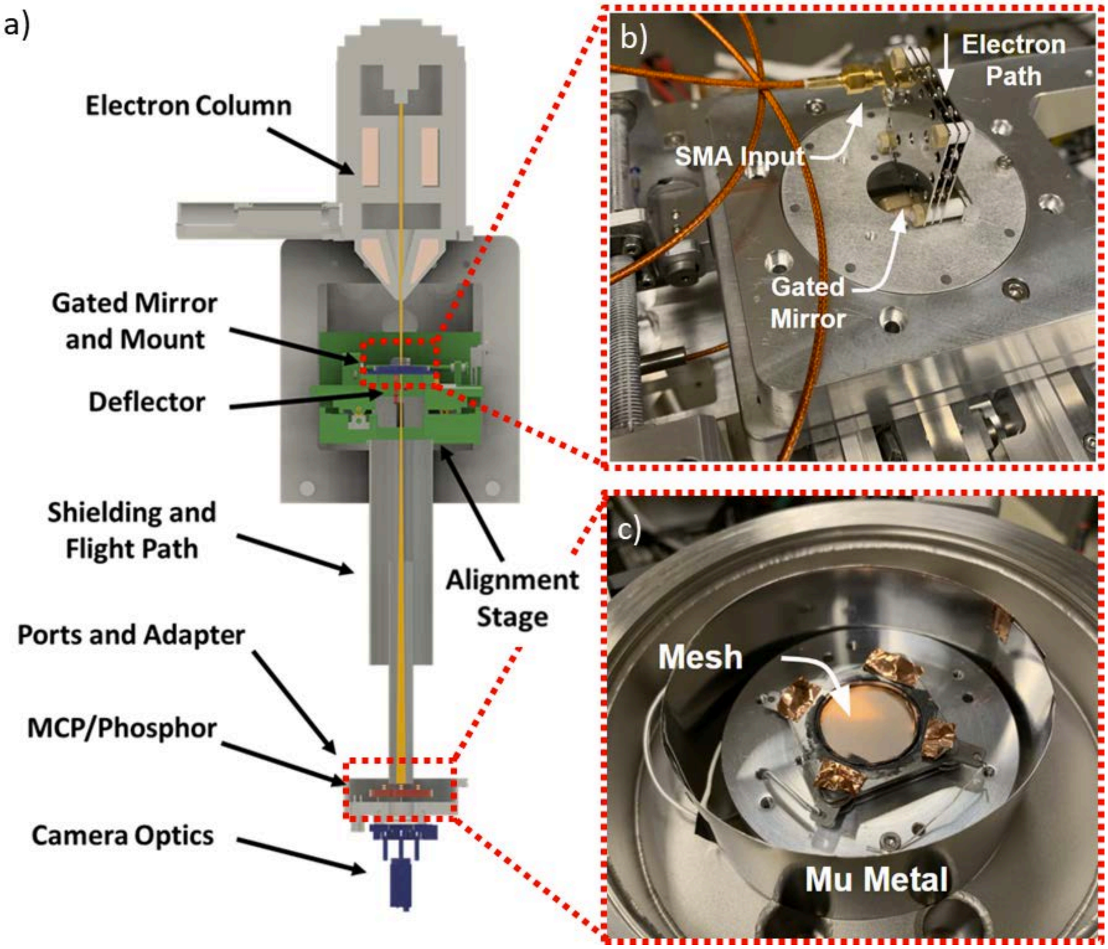

Figure 5.5: Implementation of a streak camera in an SEM. (a) A CAD rendering of the streak camera, with colorized modules. (b) The gated electron mirror simulated in Chapter 4, coupled by an SMA connector. We chose the larger version so its resonances would be more visible for testing the streak camera. (c) Custom electron imager. Surrounding it is an example of the mu metal shielding to prevent stray EMI from the turbo.

beneath that is the gated electron mirror and deflector, mounted on a 3-axis door. Beneath that is mu-metal shielded flight tube, and below that the imager. The imager consists of a 64 µm mesh with an 70% open area ratio (MC38 from Precision eForming), a 25 µm micro-channel plate (Beam Imaging Solutions), and water jet 100 µm titanium shim stock (McMaster-Carr). With a 1 keV beam driven by a 1 VPP signal, we would expect to have a 0.8 mm streak signal on the bottom of the chamber.

Finally, in Fig. 5.6 we show the RF circuitry used to drive the streak camera in its frequency domain mode. This consists of a 3.3 GHz vector signal generatior (Rhode & Schwartz SMV03) input to a power splitter (Mini-Circuits ZVSC-Z-2500). The bottom path consists first of a 1/8 pre-scaler (Mini-Circuits FPS-8-20), filtered with a low pass filter (Mini-Circuits BLP-450) to remove higher harmonics in the pre-scaler,

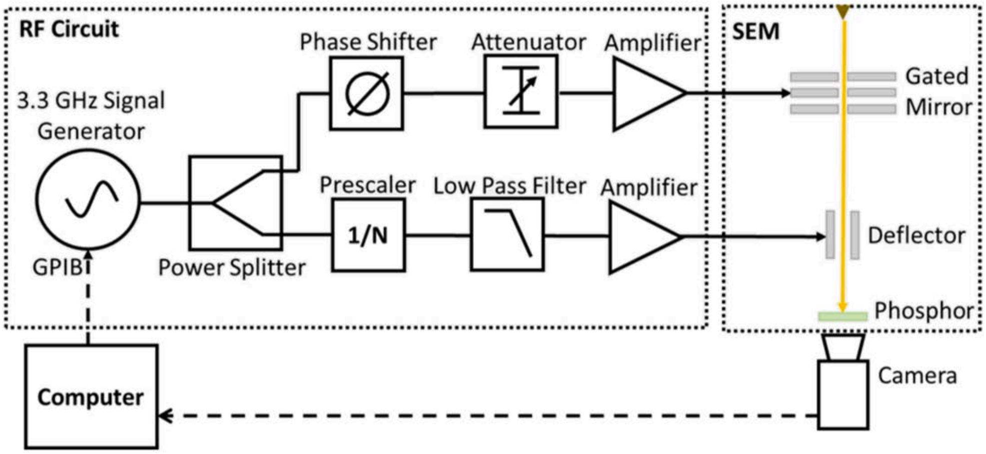

Figure 5.6: Electronics for driving the streak camera. First, we use a General Purpose Interface Bus (GPIB) to control a 3.3 GHz signal generator. This outputs a signal that is then divided in two paths by a wide-bandwidth power splitter. The first path is shown on the bottom, and drives the deflecting electrodes of the streak camera. First, this signal is inserted into a 1/8 pre-scaler. To remove higher harmonics, we use a low-pass filter to result in a clean sinusoidal output at a frequency 8x lower than the driving waveform. An attenuator (not shown) is placed on the amplifier input to control the total output power. The second, top path excites the gated electron mirror. This path consists of a phase shifter, to set the reference zero phase at low frequencies, a variable attenuator to control the amplifier power, and an power amplifier. By having the gain and phase controllable, we can accuracy in measuring the system response, especially around resonances where these quantities vary drastically.

and then plugged into 10-500 MHz gain block (Mini-Circuits ZHL-1-2W-S+). Attenuators are placed in front of the amplifier to ensure it does not get damaged in open circuit. The top, higher frequency path is first plugged into a phase shifter (Arra INC. Model 3448B), then various attenuator to protect the amplifier, and finally a 700-4200 MHz amplifier (MiniCircuits ZHL-42). In order to acquire the frequency response of this system, we strongly attenuate the power before the amplifiers, and plug the outputs into our LeCroy 2 GHz oscilloscope, which we use in sampling mode to acquire the signals up to 3.3 GHz. Note that for different frequency ranges, different band pass filters and amplifiers were used, but all work shown here used this configuration.

5.3.1 Early Results

We then tested this streak camera. Fig. 5.7a shows a top-down image of the gated mirror load. Fig. 5.7b shows this same image as an SEM micrograph, which we use to image the mirror so select a portion of the mirror to prove. In order to measure the fields in the gated mirror, we turn the SEM to spot mode and center the beam, with slight adjustments due to changes in alignment. We can vary the sampling location spatially by aligning the beam to the streak camera, and then moving the load in to that point with the

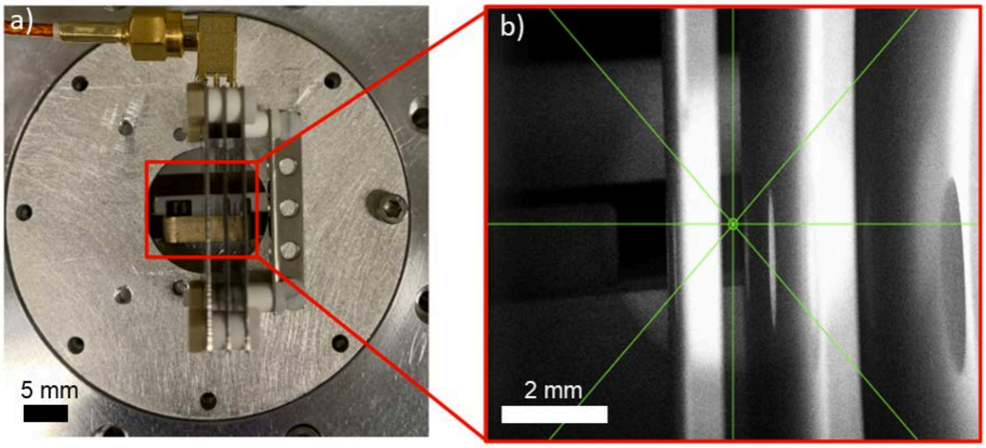

Figure 5.7: Gated mirror in the streak camera. (a) Photograph of the streak camera from the top. (b) SEM micrograph of the streak camera.

SEM stage.

Fig. 5.8a-c shows the electron traces at various frequencies. This pattern can be described as a parametric curve in x and y, with the x direction being governed by the slower, high amplitude oscillations in the lower deflector, while the y direction is due to higher frequency perturbations on the gated mirror. Both of these deflection directions are described by the parametric Eqn. 5.3.1 below, where t is the time parameter, a the relative amplitude between the streaking, and ϕ the phase shift between the curves. This is plotted in 5.8d, showing the similarity between this curve and our observations.

$$\Delta x = \sin\left(t + \phi\right), \ \Delta y = a \sin\left(8t\right) \tag{5.2}$$

Looking closer at the curves, we can see that we can extract the relative amplitude and phase from each one, critical parameters for determining the mode structure of the gated mirror. Fig.5.8a at 200 MHz shows a large amplitude mirror (vertical) deflection and an either 0 or π phase shift. Fig.5.8b at 1 GHz shows a small decrease in amplitude, and a positive or negative $\pi/2$ phase shift. Finally, at 1.5 GHz we see a significant amplitude decrease in the mirror direction, and again a 0 or π phase shift. Notice that the phase is ambiguous to π, and must be determined by tracking the beam with small changes to the driving frequency. In this case, we define the low frequency curve as a 0 phase shift, 1 GHz as a $\pi/2$ shift, and the 1.5 GHz signal as a π shift. Note that since we have not calibrated the driving signals, which are not flat over the spectrum of the RF circuitry, we can not tell which modulations are due to the circuitry and which to the load. Also, because the time-scale of the electron passing the mirror is very similar to the

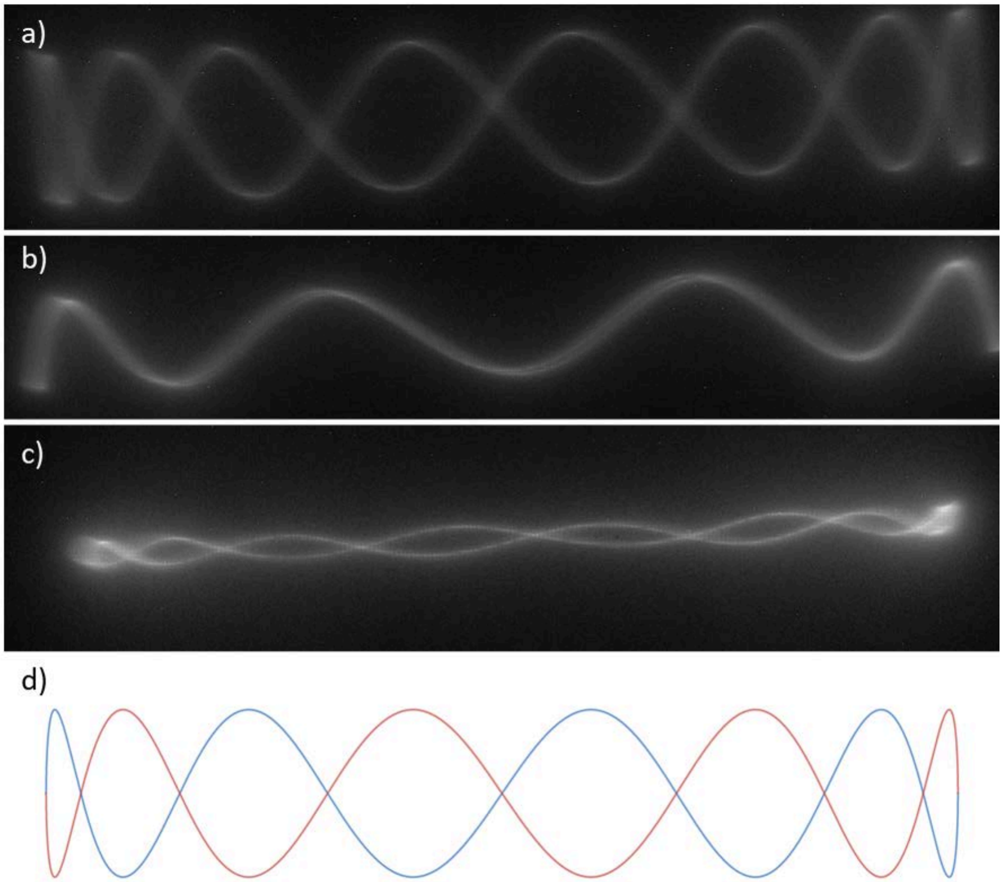

Figure 5.8: The streak camera output at various frequencies. (a) 200 MHz trace, showing an approximately 0 or π phase shift between the signals and maximum amplitude. (b) 1 GHz trace, showing a $\pi/2$ phase shift, and slight amplitude modulation. (c) 1.5 GHz trace (d) Parametric equation describing all of the observed traces.

mirrors oscillation time, we must integrate the path in space and time to predict electron responses at each frequency. Future work will address both of factors, allowing us to eventually fit our data to simulation and validate mirror performance.

Chapter 6

Conclusions and Future Work

In this work, we demonstrated the potential of GaN power electronics to drive a gated electron mirror, a critical element in realizing a quantum electron microscope. We first validated this concept by constructing a test-bed circuit capable of switching 100 V in under 1.5 ns with ringing, and under 3 ns without ringing. We expanded this to double-sided pulsing as well, allowing for faster repetition rates and opening of the gated mirror cavity. We then simulated the mirror in the frequency domain, and demonstrated a model of the mirror's lowest resonance as an RLC resonator, which allowed us to simplify analysis of the load and damp the dominant ringing of the field. We then extracted the temporal response of the electric fields in the load at various points, demonstrating 1 ns switching in the gated mirror throughout the region the electron sees. We estimated the maximum possible switching speeds of the load, and examined switching in other loads. Finally, we showed progress on characterizing the gated mirror in the frequency domain using an electron beam in an SEM, setting up future work on characterizing the mirror in the time domain to demonstrate stable switching.

While significant progress has been made in realizing a gated electron mirror, there are still several areas that need further work. These are centered around understanding fully the classical and quantum interactions of electrons with the gated mirror, which requires further simulation and improving the electron streak camera. In the following sections, we explain in broad terms what still needs to be done, focusing on four topics – improving our simulations, calculating real electron paths in our mirror, improvements to our streak camera, and true time-dependent testing of our mirror structure.

6.1 Improvements to Simulation Resolution Near the Optical Axis

The first area of improvement we need is in the simulations we constructed. As one can see from both Fig. 4.9 and Fig. 4.5 in Chapter 4, there is a certain amount of roughness in our simulation models caused by the coarseness of the meshing used. In Fig. 4.9 we see this as non-physical field graininess, most apparent near the edges of the holes. Furthermore, the fields around these points are not perfectly cylindrically symmetric at low frequencies, resulting in the significant deviations in final switching values we see about the optical axis in Fig. 4.5b, specifically for points T and L symmetrically about the optical axis point O.

The simplest way to improve this would be to decrease the size of the meshing. However, this greatly increases computational requirements, and would make the current simulations, that run in a matter of hours, take days with our current computing resources. A more sophisticated approach would be to improve meshing specifically around the optical axis, as well as more carefully think about the frequency stepping and range needed for simulation. We could also introduce convergence criteria based on the symmetries we would expect to develop in the problem, although this would be difficult to implement. Also, given DC simulations are much easier to run, getting a highly accurate static field model to compare to as a ground truth would be extremely useful. While the course simulations were useful for developing an overall sense of mode structure, finer simulations will be needed to understand electron interactions with it.

6.2 Electron Interactions with the Gated Mirror

Another challenge we must address is fully understanding interactions of an incident electron with the changing fields of the gated mirror, and calculating the observable results. In Chapter 5, we briefly introduced a model for interacting with the mirror in the easier deflector-like configuration. This model was simpler since we could treat the deflecting fields as perturbations to the electron, keeping the path integral a simple straight path. Furthermore, we posited that at low enough frequencies that the gated mirror fields would appear stationary to the electron, meaning we could ignore the relative time-dependence of the gated mirror and electron. This led us to Eqn. 5.1, which is simple to solve in our model.

Both of these assumptions are not valid for the gated mirror however. Even at relatively low frequencies of 1 GHz, the assumption of stationary fields from the point of view of the electron breaks down, as the electron takes about 1 ns to traverse the mirror. This means that we must explicitly take into account the time dependence of the deflecting fields in our integral. For frequency domain measurements, this means we will see the appearance of anti-resonances that do not truly exist in our mirror from the point of view of the wave, caused by the mirror field going through a full cycle while the electron goes through it, perfectly cancelling out the deflection of the electron. In order to avoid this type effect, we will have to probe the mirror at various energies and know where these effects occur.

In the case of true gated mirror operation, both of these assumptions will break down, as the paths are necessarily highly curved in reflecting modes. Furthermore, the electron slows down and speeds up while propagating in this mode, due to fields acting in the direction of electron, making the time dependence even more significant and hard to calculate. This becomes even worse when biasing is introduced, as required for true mirror performance, due to slowing the electrons even further.

The model we presented also completely neglected the effects of magnetic fields. In the use case of the gated mirror, magnetic fields should be insignificant, since the final state of the gated mirror is a near-static electric field, and because the velocity of the electron is very slow upon reflection and thus couples only weakly to magnetic fields. However, for the perturbative frequency-domain testing of the gated mirror used in the streak camera, neither of these factors are true and so we must account for changing magnetic fields induced by the changing electric fields.

Finally, since a QEM is an interferometer, the quantum properties of electrons such as phase and coherence matter greatly to the mirrors performance. Since some high frequency ringing effects will always exist in our mirror beyond the bandwidth we can filter to, we must understand how they effect the electron in order to understand to what degree they must be removed. This is especially critical since the gated mirror will slow the electrons significantly upon reflection, leading to strong interactions with these weakly ringing fields.

6.3 Frequency Domain Streak Camera Improvements

There are also several aspects in which the streak camera design we have can be improved. The first, most significant way is to implement automated compensation. The compensation routine would consist of a driver and oscilloscope with a high-bandwidth attenuator, where we put in a constant known signal of varying frequency into the driving circuitry. We would then simultaneously measure both the amplitude and phase of both the streaking and mirror signals, taken at the point where we would connect the SMA connectors to the gated mirror and deflector. We could then normalize out these effects by dividing them out from our measured results, to match simulation.

A second significant improvement would be to automate acquisition and processing of the output traces shown in Fig. 5.8a-c from Chapter 5. By fitting these curves to the parametric equations of 5.3.1, we could more accurately and consistently extract phase and amplitude quantities. This would also greatly increase the speed and thus frequency resolution at which we could take these measurements.

Third, in order to fully visualize mode structures better we need to push our measurements up to 10 GHz and beyond. This would require use of different amplifiers and drivers than what we currently use, and stitching together of these different ranges, since to our knowledge no commercial amplifier is capable of such a broadband range. Implementation of some kind of RF switching circuitry to automate these range shifts would also be extremely valuable.

6.4 Time Domain Streak Camera Development

While frequency domain switching is a great diagnostic tool and a validation of our models, the mirror performance we care most about is in the time domain, which we have yet to implement at the speeds required for a gated mirror. This is due to several factors that make time-domain measurements significantly more challenging, which we outline below.

The first challenge is that in order to measure such high-voltage high-speed switching, we need similarly high-speed, high voltage driving. As has been explained in this work, such high-voltage driving is not readily available. Because of this, our designs plan to use significantly slowed GaNFET circuits to streak our normal high-speed ones.

A second challenge comes from the dynamic range of the signal of interest. Since we need to view ringing of less than a volt on a transition of 100 V, we need to be able to properly align the streak camera signal, introducing the need for biasing which complicated the design further. Also, since the ringing signals are quite small, we need to use lower electron beam energies and large beam throws to amplify the streaking signal so that it is observable. Resolving this signal is much harder due to issues focusing the beam at the bottom of the chamber at low energies, and because the beams higher sensitivity to stray EMI in the system.

Third, time-domain streaking has significantly reduced signal-to-noise ratios in our output. This is because if we would like to look at a signal of 10 ns at a repetition rate of 10 MHz, we only get to use 10% of the beam intensity relative to the frequency domain measurements. Thus shortcomings with imaging system gain, the numerical aperture of our imaging lens, camera noise, and stray light become far more significant.

All of these issues should be able to be overcome in the coming months, and hopefully will allow us to directly verify that our gated mirror is capable of switching 100 V, sub-nanosecond fields, removing another barrier to the realization of a quantum electron microscope.

Bibliography

[1] R. F. Egerton, "Control of radiation damage in the TEM," *Ultramicroscopy*, vol. 127, pp. 100–108, 2013.

[2] P. Kruit, R. G. Hobbs, C. S. Kim, Y. Yang, V. R. Manfrinato, J. Hammer, S. Thomas, P. Weber, B. Klopfer, C. Kohstall, T. Juffmann, M. A. Kasevich, P. Hommelhoff, and K. K. Berggren, "Designs for a quantum electron microscope," *Ultramicroscopy*, vol. 164, pp. 31–45, 2016.

[3] T. Juffmann, B. B. Klopfer, T. L. Frankort, P. Haslinger, and M. A. Kasevich, "Multi-pass microscopy," *Nature Communications*, vol. 7, 2016.

[4] R. F. Egerton, P. Li, and M. Malac, "Radiation damage in the TEM and SEM," *Micron*, vol. 35, no. 6, pp. 399–409, 2004.

[5] R. Egerton, *Electron Energy-Loss Spectroscopy in the Electron Microscope.* 2011.

[6] P. E. Batson, N. Dellby, and O. L. Krivanek, "Sub-ångstrom resolution using aberration corrected electron optics," *Nature*, vol. 418, pp. 617–620, 8 2002.

[7] M. Adrian, J. Dubochet, J. Lepault, and A. W. McDowall, "Cryo-electron microscopy of viruses," *Nature*, vol. 308, no. 5954, pp. 32–36, 1984.

[8] R. Henderson and P. N. Unwin, "Three-dimensional model of purple membrane obtained by electron microscopy," *Nature*, vol. 257, no. 5521, pp. 28–32, 1975.

[9] E. Nogales, "The development of cryo-EM into a mainstream structural biology technique," *Nature Methods*, vol. 13, no. 1, pp. 24–27, 2015.

[10] T. Nakane, A. Kotecha, A. Sente, G. McMullan, S. Masiulis, P. M. G. E. Brown, I. T. Grigoras, L. Malinauskaite, T. Malinauskas, J. Miehling, T. Uchański, L. Yu, D. Karia, E. V. Pechnikova, E. de Jong, J. Keizer, M. Bischoff, J. McCormack, P. Tiemeijer, S. W. Hardwick, D. Y. Chirgadze, G. Murshudov,

A. R. Aricescu, and S. H. W. Scheres, “Single-particle cryo-EM at atomic resolution,” *Nature*, vol. 587, no. May, 2020.

[11] M. Khoshouei, M. Radjainia, A. J. Phillips, J. A. Gerrard, A. K. Mitra, J. M. Plitzko, W. Baumeister, and R. Danev, “Volta phase plate cryo-EM of the small protein complex Prx3,” *Nature Communications*, vol. 7, 2016.

[12] R. M. Glaeser, “How good can cryo-EM become?,” *Nature Methods*, vol. 13, no. 1, pp. 28–32, 2016.

[13] R. F. Egerton, “Choice of operating voltage for a transmission electron microscope,” *Ultramicroscopy*, vol. 145, pp. 85–93, 2014.

[14] M. J. Peet, R. Henderson, and C. J. Russo, “The energy dependence of contrast and damage in electron cryomicroscopy of biological molecules,” *Ultramicroscopy*, vol. 203, no. December 2018, pp. 125–131, 2019.

[15] R. F. Egerton, *Electron energy-loss spectroscopy in the electron microscope.* Springer Science & Business Media, 3rd ed., 2011.

[16] G. McMullan, A. R. Faruqi, and R. Henderson, *Direct Electron Detectors*, vol. 579. Elsevier Inc., 1 ed., 2016.

[17] A. Punjani, J. L. Rubinstein, D. J. Fleet, and M. A. Brubaker, “CryoSPARC: Algorithms for rapid unsupervised cryo-EM structure determination,” *Nature Methods*, vol. 14, no. 3, pp. 290–296, 2017.

[18] O. Scherzer, “The theoretical resolution limit of the electron microscope,” *Journal of Applied Physics*, vol. 20, no. 1, pp. 20–29, 1949.

[19] R. Danev and K. Nagayama, “Transmission electron microscopy with Zernike phase plate,” tech. rep., 2001.

[20] R. Danev and W. Baumeister, “Expanding the boundaries of cryo-EM with phase plates,” 2017.

[21] K. Schultheib, F. Párez-Willard, B. Barton, D. Gerthsen, and R. R. Schröder, “Fabrication of a Boersch phase plate for phase contrast imaging in a transmission electron microscope,” *Review of Scientific Instruments*, vol. 77, no. 3, p. 33701, 2006.

[22] J. Verbeeck, A. Béché, K. Müller-Caspary, G. Guzzinati, M. A. Luong, and M. Den Hertog, “Demonstration of a 2×2 programmable phase plate for electrons,” *Ultramicroscopy*, vol. 190, pp. 58–65, 7 2018.

[23] Y. Yang, C. S. Kim, R. G. Hobbs, P. D. Keathley, and K. K. Berggren, "Nanostructured-membrane electron phase plates," *Ultramicroscopy*, 2020.

[24] J. Verbeeck, H. Tian, and P. Schattschneider, "Production and application of electron vortex beams," *Nature*, vol. 467, no. 7313, pp. 301–304, 2010.

[25] B. J. McMorran, A. Agrawal, I. M. Anderson, A. A. Herzing, H. J. Lezec, J. J. McClelland, and J. Unguris, "Electron vortex beams with high quanta of orbital angular momentum," *Science*, vol. 331, no. 6014, pp. 192–195, 2011.

[26] G. Ruffato, E. Rotunno, and V. Grillo, "A general framework for conformal transformations in electron optics," *arXiv*, 2020.

[27] H. Okamoto, "Full-vortex flux qubit for charged-particle optics," *Physical Review A*, vol. 97, no. 4, p. 42342, 2018.

[28] H. Okamoto and Y. Nagatani, "Entanglement-assisted electron microscopy based on a flux qubit," *Applied Physics Letters*, vol. 104, p. 062604, 2 2014.

[29] H. Okamoto, T. Latychevskaia, and H. W. Fink, "A quantum mechanical scheme to reduce radiation damage in electron microscopy," *Applied Physics Letters*, vol. 88, no. 16, pp. 1–4, 2006.

[30] J. P. Dowling, "Quantum optical metrology - The lowdown on high-N00N states," *Contemporary Physics*, vol. 49, no. 2, pp. 125–143, 2008.

[31] A. C. Elitzur and L. Vaidman, "Quantum mechanical interaction-free measurements," *Foundations of Physics*, vol. 23, no. 7, pp. 987–997, 1993.

[32] P. Kwiat, H. Weinfurter, T. Herzog, A. Zeilinger, and M. A. Kasevich, "Interaction-free measurement," *Physical Review Letters*, vol. 74, no. 24, pp. 4763–4766, 1995.

[33] W. P. Putnam and M. F. Yanik, "Noninvasive electron microscopy with interaction-free quantum measurements," *Physical Review A - Atomic, Molecular, and Optical Physics*, vol. 80, no. 4, pp. 1–4, 2009.

[34] M. Turchetti, C. S. Kim, R. Hobbs, Y. Yang, P. Kruit, and K. K. Berggren, "Design and simulation of a linear electron cavity for quantum electron microscopy," *Ultramicroscopy*, vol. 199, pp. 50–61, 4 2019.

[35] M. A. Krielaart and P. Kruit, "Grating mirror for diffraction of electrons," *Physical Review A*, vol. 98, no. 6, pp. 1–9, 2018.

[36] H. Lichte, “Coherent electron optical experiments using an electron mirror,” in *Proceedings of the international symposium foundations of quantum mechanics in the light of new technolog*, pp. 29–31, 1984.

[37] T. Juffmann, S. A. Koppell, B. B. Klopfer, C. Ophus, R. M. Glaeser, and M. A. Kasevich, “Multi-pass transmission electron microscopy,” *Scientific Reports*, vol. 7, no. 1, 2017.

[38] B. L. Higgins, D. W. Berry, S. D. Bartlett, H. M. Wiseman, and G. J. Pryde, “Entanglement-free Heisenberg-limited phase estimation,” *Nature*, vol. 450, no. 7168, pp. 393–396, 2007.

[39] S. A. Koppell, M. Mankos, A. J. Bowman, Y. Israel, T. Juffmann, B. B. Klopfer, and M. A. Kasevich, “Design for a 10 keV multi-pass transmission electron microscope,” *Ultramicroscopy*, vol. 207, no. April, 2019.

[40] A. I. Bishop and P. F. Barker, “Subnanosecond Pockels cell switching using avalanche transistors,” *Review of Scientific Instruments*, vol. 77, no. 4, pp. 1–6, 2006.

[41] M. M. Wolff and W. E. Stephens, “A pulsed mass spectrometer with time dispersion,” *Review of Scientific Instruments*, vol. 24, no. 8, pp. 616–617, 1953.

[42] E. F. Ritz, *Recent Advances in Electron Beam Deflection*, vol. 49. 1979.

[43] R. Fishman, M. Rappaport, L. Vejby-Christensen, O. Heber, I. Ben-Itzhak, M. Dahan, and D. Zajfman, “Electrostatic bottle for long-time storage of fast ion beams,” Tech. Rep. 3, 2002.

[44] W. Jiang, “Fast high voltage switching using stacked MOSFETs,” *IEEE Transactions on Dielectrics and Electrical Insulation*, vol. 14, no. 4, pp. 947–950, 2007.

[45] A. Chaney and R. Sundararajan, “Simple MOSFET-based high-voltage nanosecond pulse circuit,” *IEEE Transactions on Plasma Science*, vol. 32, no. 5 I, pp. 1919–1924, 2004.

[46] R. J. Baker and B. P. Johnson, “A 500 V nanosecond pulse generator using cascode-connected power MOSFETs,” *Measurement Science and Technology*, vol. 3, no. 8, pp. 775–777, 1992.

[47] L. Jinyuan, S. Bing, and C. Zenghu, “High voltage fast ramp pulse generation using avalanche transistor,” *Review of Scientific Instruments*, vol. 69, no. 8, pp. 3066–3067, 1998.

[48] W. M. Henebry, “Avalanche transistor circuits,” *Review of Scientific Instruments*, vol. 32, no. 11, pp. 1198–1203, 1961.

[49] D. M. Benzel and M. D. Pocha, "1000-V, 300-ps pulse-generation circuit using silicon avalanche devices," *Review of Scientific Instruments*, vol. 56, no. 7, pp. 1456–1458, 1985.

[50] L. Zou, S. Gupta, and C. Caloz, "A simple picosecond pulse generator based on a pair of step recovery diodes," *IEEE Microwave and Wireless Components Letters*, vol. 27, no. 5, pp. 467–469, 2017.

[51] E. Afshari and A. Hajimiri, "Nonlinear transmission lines for pulse shaping in silicon," *IEEE Journal of Solid-State Circuits*, vol. 40, no. 3, pp. 744–752, 2005.

[52] Carl E. Baum, L. Carin, and A. P. Stone, *Ultra-Wideband, Short-Pulse Electromagnetics*.

[53] G. Mourou and W. Knox, "High-power switching with picosecond precision," *Applied Physics Letters*, vol. 35, no. 7, pp. 492–494, 1979.

[54] S. Kohler, V. Couderc, R. O'Connor, D. Arnaud-Cormos, and P. Leveque, "A versatile high voltage nano-and sub-nanosecond pulse generator," *IEEE Transactions on Dielectrics and Electrical Insulation*, vol. 20, no. 4, pp. 1201–1207, 2013.

[55] A. De Angelis, M. Dionigi, R. Giglietti, and P. Carbone, "Experimental comparison of low-cost sub-nanosecond pulse generators," *IEEE Transactions on Instrumentation and Measurement*, vol. 60, no. 1, pp. 310–318, 2011.

[56] J. C. Martin, "Nanosecond Pulse Techniques," *Proceedings of the IEEE*, vol. 80, no. 6, pp. 934–945, 1992.

[57] J. Mankowski and M. Kristiansen, "A review of short pulse generator technology," *IEEE Transactions on Plasma Science*, vol. 28, no. 1, pp. 102–108, 2000.

[58] M. Samizadeh Nikoo, A. Jafari, N. Perera, M. Zhu, G. Santoruvo, and E. Matioli, "Nanoplasma-enabled picosecond switches for ultrafast electronics," *Nature*, vol. 579, no. 7800, pp. 534–539, 2020.

[59] D. M. Pozar, *Microwave Engineering, 4th Edition.* 2012.

[60] B. B. Klopfer, S. A. Koppell, A. J. Bowman, Y. Israel, and M. A. Kasevich, "RF pulse shaping for gated electron mirrors," pp. 1–5, 12 2020.

[61] Y. Wu, M. Jacob-Mitos, M. L. Moore, and S. Heikman, "A 97.8% efficient GaN HEMT boost converter with 300-W output power at 1 MHz," *IEEE Electron Device Letters*, vol. 29, no. 8, pp. 824–826, 2008.

[62] A. Brown, K. Brown, J. Chen, K. C. Hwang, N. Kolias, and R. Scott, "W-band GaN power amplifier MMICs," *IEEE MTT-S International Microwave Symposium Digest*, pp. 11–14, 2011.

[63] J. S. Glaser, "High power nanosecond pulse laser driver using a gan fet," *PCIM Europe Conference Proceedings*, no. 225809, pp. 662–669, 2018.

[64] H. Amano, Y. Baines, E. Beam, M. Borga, T. Bouchet, P. R. Chalker, M. Charles, K. J. Chen, N. Chowdhury, R. Chu, C. D. Santi, M. M. D. Souza, S. Decoutere, L. D. Cioccio, B. Eckardt, T. Egawa, P. Fay, J. J. Freedsman, L. Guido, O. Häberlen, G. Haynes, T. Heckel, D. Hemakumara, P. Houston, J. Hu, M. Hua, Q. Huang, A. Huang, S. Jiang, H. Kawai, D. Kinzer, M. Kuball, A. Kumar, K. B. Lee, X. Li, D. Marcon, M. März, R. McCarthy, G. Meneghesso, M. Meneghini, E. Morvan, A. Nakajima, E. M. S. Narayanan, S. Oliver, T. Palacios, D. Piedra, M. Plissonnier, R. Reddy, M. Sun, I. Thayne, A. Torres, N. Trivellin, V. Unni, M. J. Uren, M. V. Hove, D. J. Wallis, J. Wang, J. Xie, S. Yagi, S. Yang, C. Youtsey, R. Yu, E. Zanoni, S. Zeltner, and Y. Zhang, "The 2018 {GaN} power electronics roadmap," *Journal of Physics D: Applied Physics*, vol. 51, p. 163001, 3 2018.

[65] A. Lidow, M. de Rooij, J. Strydom, D. Reusch, and J. Glaser, *GaN Transistors for Efficient Power Conversion.* 2019.

[66] T. Instruments, "LMG1020 data sheet," tech. rep., 2018.

[67] C. R. Paul, *Inductance: Loop and Partial.* 2009.

[68] D. M. Pozar, *Microwave Engineering.* New York: Wiley, 2009.

[69] G. Wong Choi, J. Joo Choi, and S. Hoon Han, "Note: Picosecond impulse generator driven by cascaded step recovery diode pulse shaping circuit," *Review of Scientific Instruments*, vol. 82, no. 1, 2011.

[70] R. K. Cacak and J. R. Craig, "Magnetic field uniformity around near-Helmholtz coil configurations," *Review of Scientific Instruments*, vol. 40, no. 11, pp. 1468–1470, 1969.

[71] *Handbook of Charged Particle Optics.* 2017.

[72] Y. TSUCHIYA, "Picosecond Streak Camera and Its Applications," *The Review of Laser Engineering*, vol. 10, no. 2, pp. 148–164, 1982.

[73] G. Mourou and W. Knox, "A picosecond jitter streak camera," *Applied Physics Letters*, vol. 36, no. 8, pp. 623–626, 1980.